



## **Terms and Conditions of Use of Digitised Theses from Trinity College Library Dublin**

### **Copyright statement**

All material supplied by Trinity College Library is protected by copyright (under the Copyright and Related Rights Act, 2000 as amended) and other relevant Intellectual Property Rights. By accessing and using a Digitised Thesis from Trinity College Library you acknowledge that all Intellectual Property Rights in any Works supplied are the sole and exclusive property of the copyright and/or other IPR holder. Specific copyright holders may not be explicitly identified. Use of materials from other sources within a thesis should not be construed as a claim over them.

A non-exclusive, non-transferable licence is hereby granted to those using or reproducing, in whole or in part, the material for valid purposes, providing the copyright owners are acknowledged using the normal conventions. Where specific permission to use material is required, this is identified and such permission must be sought from the copyright holder or agency cited.

### **Liability statement**

By using a Digitised Thesis, I accept that Trinity College Dublin bears no legal responsibility for the accuracy, legality or comprehensiveness of materials contained within the thesis, and that Trinity College Dublin accepts no liability for indirect, consequential, or incidental, damages or losses arising from use of the thesis for whatever reason. Information located in a thesis may be subject to specific use constraints, details of which may not be explicitly described. It is the responsibility of potential and actual users to be aware of such constraints and to abide by them. By making use of material from a digitised thesis, you accept these copyright and disclaimer provisions. Where it is brought to the attention of Trinity College Library that there may be a breach of copyright or other restraint, it is the policy to withdraw or take down access to a thesis while the issue is being resolved.

### **Access Agreement**

By using a Digitised Thesis from Trinity College Library you are bound by the following Terms & Conditions. Please read them carefully.

I have read and I understand the following statement: All material supplied via a Digitised Thesis from Trinity College Library is protected by copyright and other intellectual property rights, and duplication or sale of all or part of any of a thesis is not permitted, except that material may be duplicated by you for your research use or for educational purposes in electronic or print form providing the copyright owners are acknowledged using the normal conventions. You must obtain permission for any other use. Electronic or print copies may not be offered, whether for sale or otherwise to anyone. This copy has been supplied on the understanding that it is copyright material and that no quotation from the thesis may be published without proper acknowledgement.

# **Numerical Investigations of Magnetic Field Effects on Electrodeposition**

A thesis presented

by

**Treasa Ní Mhíocháin**

to

**The University of Dublin**

in application

for the degree of

**Doctor of Philosophy**

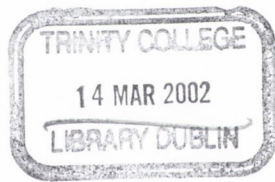
Department of Physics

University of Dublin

Trinity College

Ireland

2001



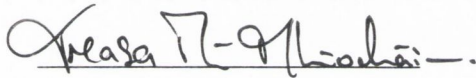
THESIS 6624

# Declaration

This thesis is submitted by the undersigned for examination for the degree of Doctor in Philosophy at the University of Dublin. It has not been submitted as an exercise for a degree at any other university.

This thesis, apart from the advice, assistance and joint effort mentioned in the acknowledgments and in the text, is entirely my own work.

I agree that the library may lend or copy this thesis freely on request.

A handwritten signature in black ink, reading "Treasa Ní Mhíocháin" with a horizontal line underneath.

Treasa Ní Mhíocháin

# **Dedication**

To my darling Mammy  
from her singing, dancing doctor.

# Acknowledgements

Thanks first and foremost to Mike Coey, for his supervision, never-ending support whatever my venture, and for the coconut in Recife. It's been a pleasure.

To Geoff Bradley for being the FLUENT king and for the many hours spent sitting waiting for convergence, and also to Jim Sexton for his enthusiasm and for so kindly putting the resources of the Centre for High Performance Computing at my disposal. Also to Turlough Downes and Alison Musgrave for their time, work and interest in the early stages of the MHD problem. I am greatly indebted to Denis Weaire and Sara McMurry for their many contributions to work on the torque problem. Thanks to David Hurley and all at Magnetic Solutions Ltd. for letting me play with magnets. Of the gang at MS, special thanks to Farid Bengrid and Laurent Clochard for knowing more than me and sharing, and to Tommy, Peter and Andrew for letting me get my hands dirty. Thanks also to Jerome Delamare and Orphée Cugat whose helpful torque suggestions made the whole thing fall into place. Thanks to Gareth Hinds, who has done his best to teach me electrochemistry, for being the original fractal guru, and to Aengus Martin who generated the beautiful electrodeposits at linear electrodes and who briefly provided me with a computational companion. To Mike Lyons who has been a great source of advice and reading material. Thanks also to Emmanuel and to Michael and Aymeric who have been great at the last minute.

As for the finances, this work was jointly supported by Forbairt, the U.S. Navy contract number ONR N00014-96-1-0767, and by the Women Graduates' Association of TCD who have been so supportive in following my progress right down to good luck cards at the stage door. They are great characters and I am thrilled to have met them.

Thanks of course for Group D therapy courtesy of Janko (print-meister and partner in crime), Ciara, Cora, Mazhar, Venki, Oscar, Guenole, Fernando, Alex, Rui, Paul, Jiang, Raju, Katie, Peng, Han, Rhian, Amanda, James, Nora, Fred, Jim, Miyuki and Vassil who have all done or are doing their time and who have made the stay great fun, and to Michelle and Guenilla for holding us together with string. Not forgetting the many Summer and project students who have livened the place up over the years. Thanks to the Physics Department for being fun, from undergrad right the way through, and in particular to Jackie, Joe, Ken, Jemmer, Chris, Michelle, Elaine, Jeannette, John and of course Tom. And especially to the back office boys, John, Steven, Eoin and Danny, for the craic, even at the most peculiar hours. Not bad for mathematicians!

To the lovely friends who have kept me coffeed and chatted for the duration, especially Adrian, Al, Aylwyn, Caitriona, Cathal, the Ciaras, Ciarán, Conor $\times$ 2, David, Derek, Elaine, Eleanor, Emma, Frank, Geoff, Imran, JC, Judith, Katherine, Keelin, Liz, Louise, Luce, Malx, Mary-Beth, Naoise, Niall, Nick, Orla, Philip, Roger, Shaz and Sarah. And to the combined efforts of Summer Festival Produc-

tions, the R&R, Arthurs' Team and HM Productions for very successfully managing to distract me — a lot.

To Michael for putting up with me.

And to Shane.

Thanks to my big brothers Cathal and Cormac who keep me in my place, to my grandparents Larry and Joan for making education matter, to my aunts and uncles for always being there, and to Frank, the real electrochemist in the family.

But thanks, most importantly, to my Dad for being my friend, and to my Mum for who I am.



# Summary

Electrodeposits are fractal in nature when grown in a flat electrochemical cell, in which an aqueous solution of salt of a metal such as Cu, Zn or Ag is held between an anode and cathode by two flat sheets of perspex. These fractals undergo dramatic changes in their morphologies when grown in the presence of a perpendicular applied magnetic field. In the case of a central cathode encircled by a ring anode, deposits become spiral rather than radial in appearance, while the stringy deposits grown between two linear electrodes tilt markedly.

An adapted diffusion limited aggregation (DLA) model was used to represent this system. The basic DLA model considers an ion as a random walker moving about a square lattice until it sticks to an occupied neighbour. As detailed in Chapter 2 this model is adapted to include physical features of the system — applied voltage, magnetic field  $B$ , gravity — by varying the probabilities of a particle moving in a given direction. Multiple ions moving simultaneously reflects concentration  $c$ , and reaction kinetics are introduced through a variable sticking probability.

Chapter 3 considers the effects of these adaptations and the resultant similarity to real electrodeposits. Two magnetic field models are considered, the second of which accurately reproduces the morphologies and chirality seen experimentally for both circular and linear electrode geometries. The magnetic field effect is most likely due to a system-wide Lorentz force induced convection, but can also be con-

sidered in terms of a local electrokinetic effect. Scaling considerations indicate that the modelled aggregates represent structures which may be as much as four orders of magnitude smaller in diameter than their experimental counterparts. Each point on a simulated aggregate may represent the nucleation and growth of a single micron-sized crystallite as found in SEM examination of these electrodeposits.

An applied magnetic field is also known to enhance the current density  $j$  plating at a flat electrode surface. In particular, a  $j \propto c^{4/3} B^{1/3}$  relationship has been reported. This phenomenon was modelled numerically (Chapter 4) using the commercial hydrodynamics finite element package FLUENT, and focussing on the Aogaki cell geometry which consists of an open channel, with a cathode on the upper plate and anode on the lower plate, all immersed in a large bath of electrolyte. The  $j \times B$  force induces hydrodynamic flow in the channel which stirs the diffusion layer, and thus varies  $j$ .

Numerical results in Chapter 5 confirm the  $j \propto c^{4/3} B^{1/3}$  relationship, and indicate regions of reverse flow inside the channel walls. At higher fields and concentrations, this stretches over the electrode surface. In this case two separate flow regimes are identified and the resultant current density profile is examined.

Useful application of these magnetohydrodynamic principles requires the ability to tailor a magnetic field in a specific region in space. One such system of nested permanent magnet cylinders, which achieves a confined, variable field, is considered in detail in the appendices.

# Contents

<b>Abstract</b> .....	<b>1</b>
<b>1 Introduction</b> .....	<b>2</b>
1.1 What is a fractal? .....	2
1.2 Box-Counting .....	8
1.3 Fractals in the Wild .....	11
1.4 Fractals in Electrochemistry .....	15
1.4.1 Circular Electrode Geometry .....	15
1.4.2 Linear Electrodes .....	20
1.4.3 Magnetic Field Effects .....	21
1.5 Principles of Electrochemistry .....	27
1.5.1 Electrolytes .....	28
1.5.2 Electrode Potential .....	28
1.5.3 Reaction Kinetics .....	31
1.5.4 Mass Transfer : Diffusion, Convection and Migration .....	33
1.5.5 Diffusion Layers and Natural Convection .....	37
1.6 Magnetohydrodynamics .....	40
1.6.1 Principles of Hydrodynamics .....	41
1.6.2 Magnetohydrodynamics .....	43
1.6.3 Electrokinetic Effect .....	44

1.7	Numerical Approaches .....	48
1.7.1	The Diffusion Limited Aggregation (DLA) Model .....	48
<b>2</b>	<b>Adapted DLA Model .....</b>	<b>53</b>
2.1	Horizontal Circular Electrode Geometry .....	53
2.1.1	Speeding Up the Basic Model .....	53
2.1.2	Applied Voltage .....	56
2.1.3	Reaction Kinetics .....	61
2.1.4	Concentration .....	62
2.1.5	Applied Magnetic Field .....	63
2.1.6	The Lattice .....	67
2.2	Vertical Circular Electrode Geometry .....	67
2.2.1	Gravity .....	68
2.3	Linear Electrode Geometry .....	71
<b>3</b>	<b>Effects of the DLA Adaptations .....</b>	<b>73</b>
3.1	Circular Electrodes .....	73
3.1.1	Applied Voltage .....	73
3.1.2	Concentration .....	77
3.1.3	Magnetic Field .....	79
3.1.4	Reaction Kinetics .....	85
3.1.5	Vertical Cell .....	89
3.2	Linear Electrodes .....	91
3.2.1	Applied Voltage .....	91
3.2.2	Applied Magnetic Field .....	93

3.2.3 Gravity .....	98
3.2.4 Gravity and Magnetic Field .....	99
<b>4 Magnetohydrodynamic Flow through an Open Channel .....</b>	<b>100</b>
4.1 The Aogaki Cell.....	100
4.2 Interplay between Convective Flow and Diffusion.....	102
4.3 Aogaki's Theoretical Prediction and Experimental Result.....	106
4.4 Numerical Model.....	108
4.4.1 The Full Geometry .....	108
<b>5 Magnetohydrodynamic Simulation .....</b>	<b>112</b>
5.1 Velocity Profiles.....	112
5.2 The Mesh .....	117
5.3 Current Density Profiles .....	117
5.4 Current Enhancement.....	125
<b>6 Discussion .....</b>	<b>134</b>
<b>7 Conclusions .....</b>	<b>146</b>
<b>Bibliography .....</b>	<b>148</b>
<b>Publications .....</b>	<b>157</b>
<b>A Analysis of Torque in Nested Halbach Cylinders .....</b>	<b>159</b>
A.1 Introduction.....	159
A.2 Experimental Results .....	164

A.3	The Model .....	170
A.3.1	Reciprocity .....	171
A.3.2	Magnetic Charge Model .....	171
A.3.3	Consequences of particular symmetries in Halbach cylinders .....	172
A.4	Numerical Simulation .....	175
A.4.1	Field Calculation .....	175
A.4.2	Torque Calculation .....	177
A.4.3	Numerical Results .....	177
A.4.4	Analysis of the Field Profile .....	182
A.5	Theoretical Model .....	186
A.5.1	Symmetry arguments in the ideal, finite length case .....	186
A.5.2	The Segmented Magnet Torque Theorem .....	190
A.5.3	Analytical Results for the Finite Length Effect .....	192
A.5.4	Torque in the case of long ideal Halbach cylinders .....	195
A.6	Conclusion .....	197
<b>B</b>	<b>Calculation of the field due to a finite length ideal Halbach cylinder .....</b>	<b>200</b>

# Abstract

Numerical simulations of magnetic field effects on electrodeposition are presented. An adapted diffusion limited aggregation (DLA) model is used to model electrodeposition in a flat electrochemical cell with either concentric or parallel electrodes. Physical properties of the system such as applied voltage, magnetic field  $B$  and gravity are introduced into the basic random walker DLA model by varying the probabilities that a particle will move in a given direction. Multiple particles move simultaneously. Resultant structures reproduce the morphology and chirality of spiral structures in a circular geometry and tilted deposits in a linear geometry for both horizontal and vertical cells. Fractal dimensions range from  $1.67 < D_f < 1.91$ . Scaling analysis indicates these electrodeposits may be self similar over at least four orders of magnitude. SEM data shows fractal behaviour of these electrodeposits down to the scale of individual micron-sized crystals, indicating that each point on a simulated aggregate represents the nucleation and growth of a single crystallite.

Enhancement of the current density  $j$  at a flat electrode in the presence of  $B$  is modelled for an Aogaki cell geometry using the FLUENT finite element package. The experimentally and theoretically demonstrated  $j \propto c^{4/3} B^{1/3}$  relationship was confirmed where  $c$  is concentration. Regions of reverse flow, which stretch over the edge of the electrode at high fields, are analysed in relation to the current density profile along the electrode surface, indicating two separate flow regimes at the plate.

Magnetic field control of electrodeposition requires devices which concentrate  $B$  on specific regions of space. An analysis of fields and torques in one such system is presented.

# Chapter 1

## Introduction

What do you get when you mix electrochemistry and magnetism?

Well, it goes a little like .....

### 1.1 What is a fractal?

The term ‘fractal’ was coined by Mandelbrot from the Latin adjective *fractus* derivative of the verb *frangere* meaning “to break”, or to create irregular pieces. He applied this term to patterns in Nature, such as coastlines, lightning strikes, clouds, snowflakes and all manner of other natural phenomena, from the growth of bacterial colonies to the structure of the Universe, which generated patterns indescribable by the rigid constructs of Euclidean geometry. Assorted examples [1]- [3] are shown in Figs.1-4. Stalwart Euclidean objects, such as the circle or the line, are in fact far more the exception than the rule in Nature. Mandelbrot thus derived a new geometry which extended to describe these systems and many new geometric curiosities besides. His geometry considered the way in which a pattern fills space on many different length scales.

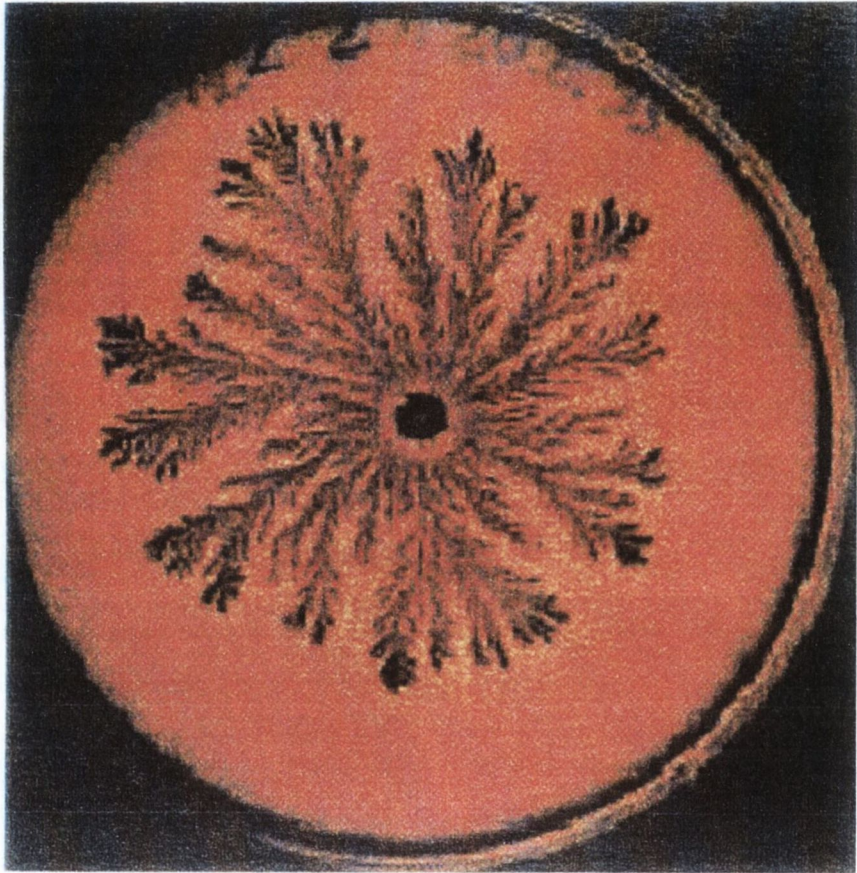
Central to the definition of this new class of objects was a new way of defining their dimension, their *fractal dimension*. Simply considered [6], for a fractal generated from a growth process, its mass  $M$  is related to its linear dimension  $R$  by

$$M \sim R^{D_f} \tag{1.1}$$





1. Patterns formed by the penetration of warm water into a layer of slush, through a layer of 'black ice'. The slush later freezes to form the white ice, and the melted regions form the patterns of black ice within the white layer (Meakin, 1998).



2. Bacterial colonies have fractal structures (Ben-Jacob).



3. A head of cauliflower has fractal form (Guyon and Stanley, 1991).

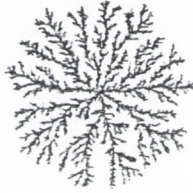


4. Spontaneous cracks in this window pane developed with a fractal structure (Guyon and Stanley, 1991).



$$M \sim R^2$$

(a)



$$M \sim R^{D_f}$$

(b)



$$M \sim R$$

(c)

5.(a) space is thoroughly filled and  $D_f = 2$ ; (b) for a fractal object  $1 < D_f < 2$ ; (c) the mass goes as the number  $N$  of lines of which the stringy pattern is formed and  $D_f = 1$ .

Here “ $\sim$ ” should be interpreted at meaning “scales as”, and  $D_f$  defines the fractal dimension. Fig.5 outlines how a fractal grown in two-dimensional space can have a non-integer fractal dimension which is intermediate between the space-filling case with  $D_f = 2$  and the linear case of  $D_f = 1$ . Thus the fractal dimension of an object indicates to some extent how thoroughly it fills space. This definition extends easily to higher dimensions.

Essential also to the understanding of fractals, is the concept of *scale-invariance* [3], meaning that the degree of their irregularity and fragmentation is identical at all scales. A fractal which is perfectly invariant under all degrees of scaling is said to be *self-similar*. So that if we can make the power law statement

$$M(R) = cR^{D_f} \quad (1.2)$$

where  $c$  is a constant, then we identify the important scaling symmetry

$$M(\lambda R) = c(\lambda R)^{D_f} = c\lambda^{D_f} R^{D_f} = \text{const} \cdot M(R) \quad (1.3)$$

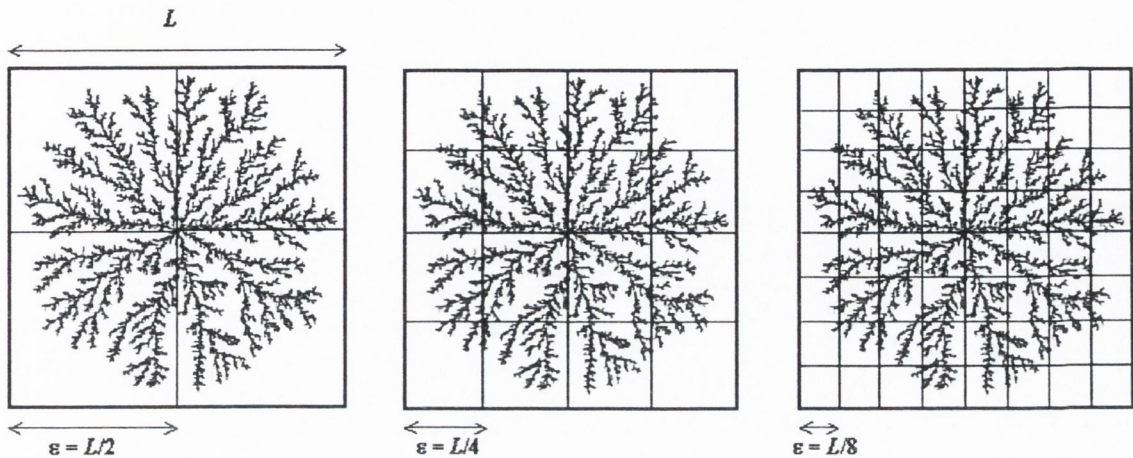
where  $\lambda$  is also a constant.

## 1.2 Box-Counting

In the course of this study, fractal dimension is determined by the ‘box-counting’ method. This method is based on an alternative expression for the power law behaviour of Eq.1.1 in the form of

$$N_\varepsilon \sim \varepsilon^{-D_f} \quad (1.4)$$

where  $N_\varepsilon$  is the minimal number of identical small objects (of linear size  $\varepsilon$ ) required to cover an object. As represented in Fig.6, 4 boxes of side  $L/2$  are required to cover the



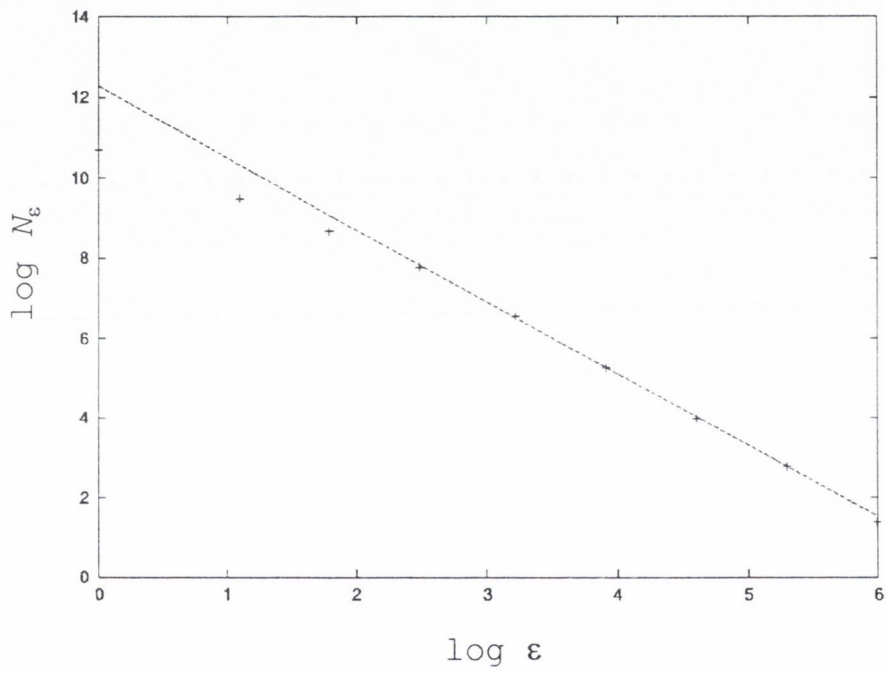
6. Two boxes of side  $L/2$  are required to cover the fractal, eight boxes of side  $L/4$ , fifty-seven boxes of side  $L/8$  and so on .....

object, 16 boxes of side  $L/4$ , 57 boxes of side  $L/8$  and so on, so that in Eq.1.4, ‘ $\sim$ ’ means

“proportional to, when  $\varepsilon \rightarrow 0$ ”.  $D_f$  may thus be determined from the power law relation

$$D_f = - \lim_{\varepsilon \rightarrow 0} \frac{\log N_\varepsilon}{\log \varepsilon}. \quad (1.5)$$

Thus by counting the number of successively smaller boxes required to cover a given fractal, we may determine its fractal dimension from the slope of a log-log plot of  $N_\varepsilon$  against  $\varepsilon$ . Such a graph tends away from linearity at small values of  $\varepsilon$ , so the slope is determined from the high  $\varepsilon$  region of the graph. An example is shown in Fig.7 for the fractal shown in Fig.6 for which  $D_f = 1.79$ . A linear variation of such a log-log plot over a large range of scales is a strong indication of self-similarity, and thus of strongly fractal behaviour.



7. Fractal dimension may be calculated from the slope of the linear region of a log-log plot of  $N_\epsilon$  against  $\epsilon$ .



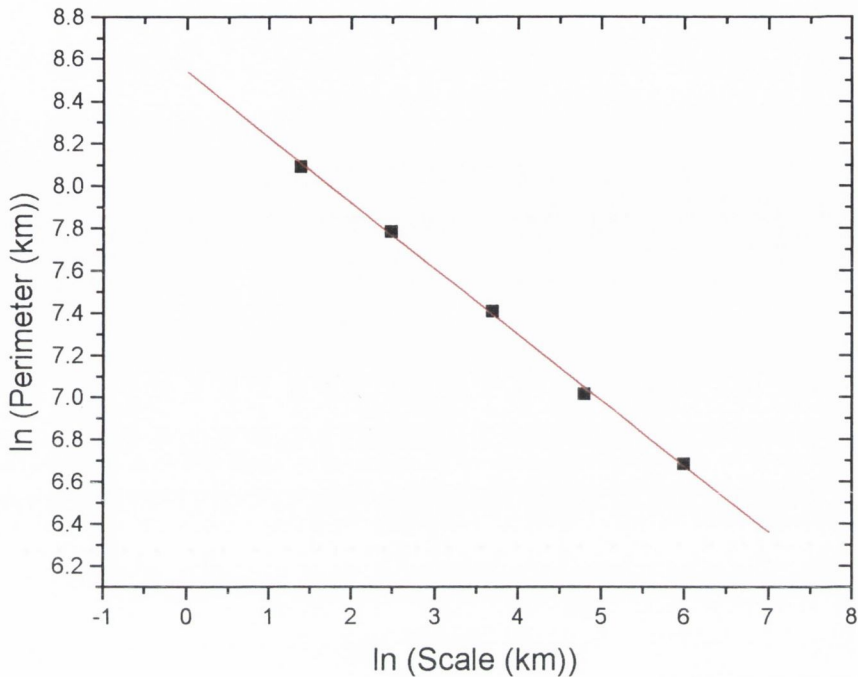
## 1.3 Fractals in the Wild

As this new geometry evolved, the extent of its application was gradually realised. Just as some degree of scale invariance is central to the definition of a fractal, fractal theories have been applied to Nature on all scales, from polymer molecules to continental coastlines to the large scale structure of the Universe. In the following chapters we will explore particular fractal structures as they appear in electrochemistry, but first a number of fractal phenomena and theories are presented as an indicator of the ubiquity of our subject matter.

### “How long is the coast of Ireland?”

The original, classic [7] question which yielded a fractal answer was “How long is the coastline of Ireland (or Britain or Japan, or whatever country one happens to be writing one’s thesis in)?”. Coastlines are fractal in the sense that they are curves with fractal dimension greater than one. The difficulty in measuring the length of a coastline is one of scale. A first estimate will involve effectively neglecting much of the detail of fjords and other features along the perimeter. Increasing the accuracy of the measurement to include some of these features will increase the calculated value for the length. The precision of the measurement can be refined to the level of individual grains of sand and on down to the molecular level. So how long is the coastline?

The solution underpinned by Richardson and later Mandelbrot is that a coastline is not simply a one-dimensional line, but rather has a fractal dimension  $D_f \simeq 1.2$ , and the structure of the detail and corrugation is similar on a variety of scales. Thus its measured length depends on the scale on which the measurement is made. Measurements of the



8. A log-log plot of coast length against scale yields a fractal dimension of 1.31 for the coastline of Ireland.

length of the coast of Ireland vary from 800 km when measured on a 400 km scale, to 1660 km on a 40 km scale and 3272 km when measured to a scale of 4 km. A straight line results from a log-log plot of length against scale as shown in Fig.8, and yields a fractal dimension of  $D_f = 1.31$  for the Irish coast.

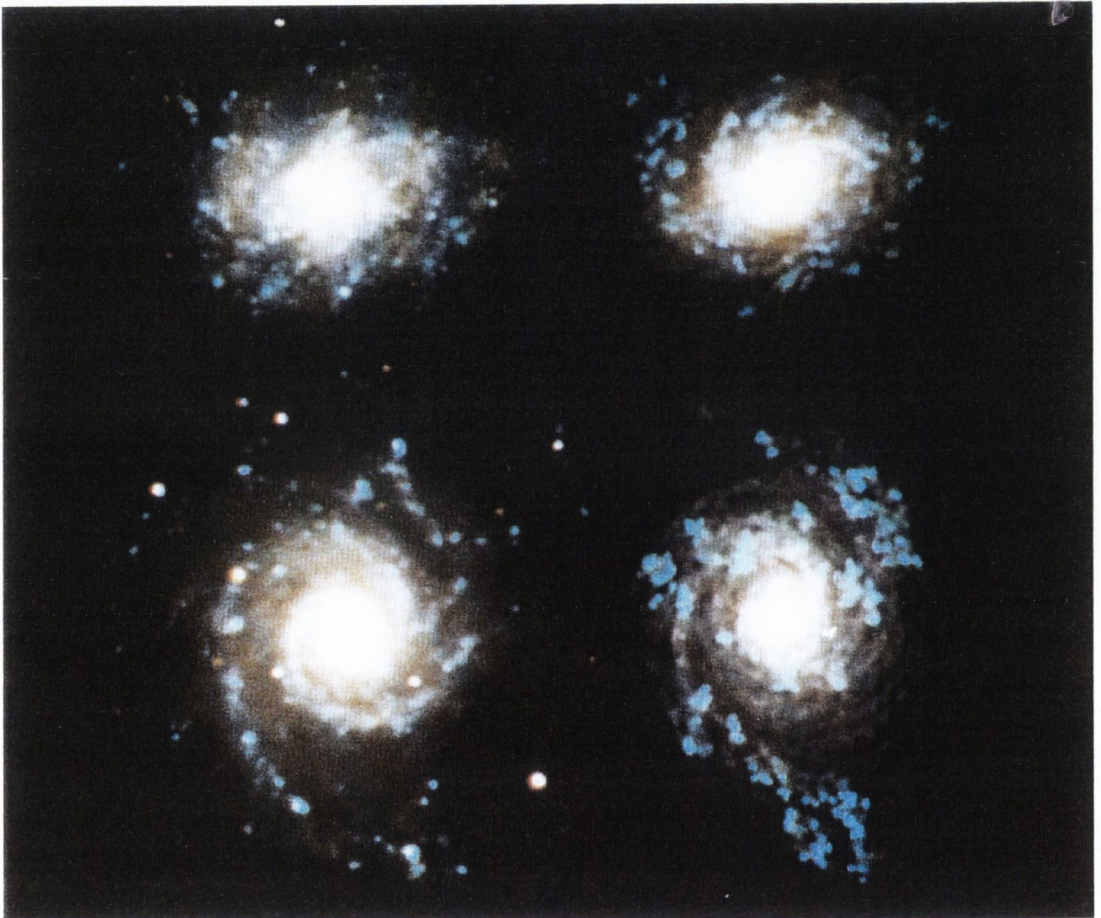
### Fractal neighbourhoods

Quite aside from fractal features in Nature, human social and geographical networks also appear to develop according to fractal principles. Extensive work on the theory of the “*fractal city*” has been completed by Batty and co-workers [14][15], who show the geometry

of urban residential development to be fractal. The degree to which space is filled, and the rate at which it is filled, both follow scaling laws which imply self-similarity at different scales. Furthermore, population density functions based on inverse power laws yield fractal dimensions specific to each city. Although results vary somewhat for different scale and measurement techniques, Batty [15] concludes that the fractal dimensions of Buffalo, Cleveland, Columbus and Pittsburgh lie between 1.7 and 1.9. Such models are proving very useful for modern urban planning and development. The same authors have begun to consider the “geography” of cyberspace [16]. One can only wonder what fractals are growing here too!

### **The fractal Universe**

Fractal theories have been applied to a variety of cosmological phenomena. In fact, fractal theories were applied to the structure of universe by Trinity physicist Fournier d’Albe as far back as 1907 [17]. On the one hand, percolation models have been used to account for the fractal structure of spiral galaxies[11]. The model assumes that intense star formation is triggered by shock waves due to some nearby event such as a supernova explosion. However, shock waves due to star formation in this region can in turn trigger star formation in neighbouring regions, and so on ... In this sense clusters of regions of intense star formation develop in much the same way as any random, fractal growth process. When combined with rotational effects due to the angular velocity of the galaxy being modelled, structures very similar to those of spiral galaxies emerge from simulation as shown in Fig.9.



9. The left-hand side of this figure shows digitised images of galaxies, while the right-hand side shows patterns generated by the galaxy percolation model of Seiden and Schulman (Meakin, 1998).

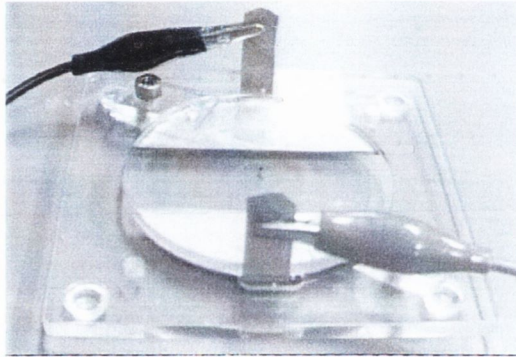
On larger scales, fractal models have been used to describe large-scale structure in the Universe [12], and even provide an alternative theory for the evolution of the Universe as a huge growing fractal consisting of many inflating fireballs that each produce new fireballs, which in turn produce more fireballs and so on ad infinitum, resulting in a “self-reproducing inflationary Universe” [13].

## 1.4 Fractals in Electrochemistry

One important segment of the whole field of fractal research, and the one that concerns us here, is electrochemistry. Electrodeposits produced under a variety of experimental conditions have unusual structures which have intrigued scientists for over five hundred years. A number of classic experiments performed by Matsushita [21], Grier [22][23] and Sawada [24] yielded patterns which have sparked renewed interest in this problem in recent years.

### 1.4.1 Circular Electrode Geometry

The experimental set-up consisted simply of a flat electrochemical cell, with an electrolytic solution of some metallic salt (for example  $\text{ZnSO}_4$  or  $\text{CuSO}_4$  in water) held between two perspex plates with a separation  $\sim 0.5$  mm. At the centre of the plates is a cathodic rod (typically made of graphite) surrounded by a thin, flat, ring of plating metal (e.g. a ring of Cu, Zn) which acts as the anode in the cell. A typical experimental set-up is shown in Fig. 10.



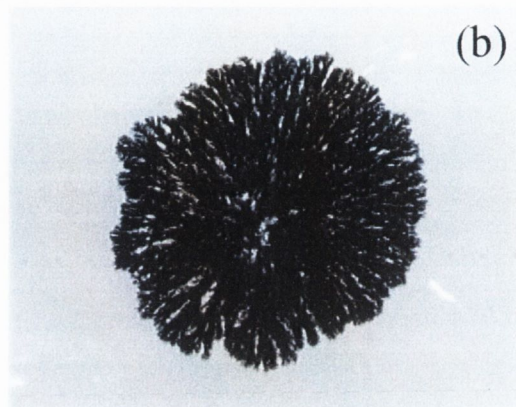
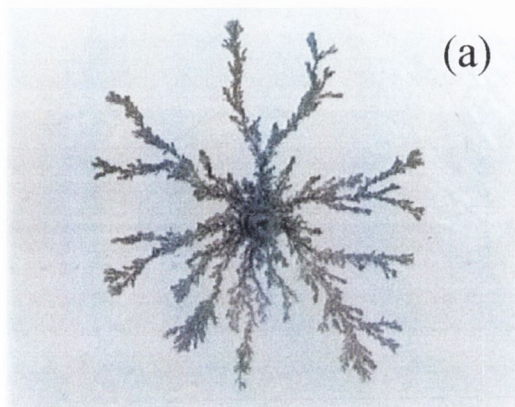
10. Typical flat, horizontal electrochemical cell. The electrolyte is held between the cathode and anode by two sheets of perspex. A voltage is applied between anode and cathode, and metal ions from the solution deposit onto the cathode. A similar set-up can also be arranged for a circular electrode geometry using a (graphite) rod at the centre of the cell as the cathode, encircled by a ring anode.

A voltage is applied between the cathode and anode. Metal ions are reduced at the cathode and the metallic deposit grows according to the chemical reaction



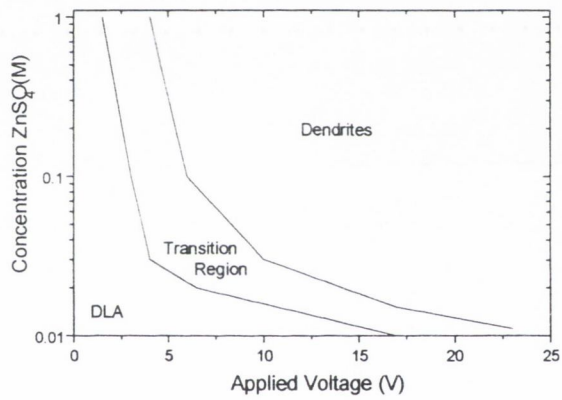
$M$  is a metal, originally in solution in ionic form  $M^{n+}$ , where  $n$  is the number of positive charges on the ion. Some typical patterns formed by the resulting deposits are shown in Fig.11.

The principal factors determining the morphology of the deposit are the magnitude of the applied voltage and the concentration of the metal ions in solution. Approximate phase diagrams have been constructed outlining the relationship between morphology and these two parameters. Broadly speaking, at low voltages and low concentrations the deposits form by *diffusion limited aggregation* (DLA) and are fine, wispy and fern-like with a characteristic fractal dimension  $D_f = 1.67$ . Still at low concentrations, but at higher applied voltages, the deposits become more dense, growing outwards with an expanding circular envelope, and are known as *dense radial*. At high values of both voltage and concentration, the deposits grow rapidly along a small number of branches and lose their radial nature to become *dendritic*. At still higher voltages and concentrations, at the upper extremum of the phase diagram, the deposits become increasingly one-dimensional and are called *stringy*. A typical phase diagram due to Grier et al is shown in Fig.12. Most notably, deposits which fall under the DLA classification are of particular interest as this kind of fractal structure is common throughout Nature (see Section 1.3) and provided the inspiration for an important numerical tool which will be detailed in Section 1.7.

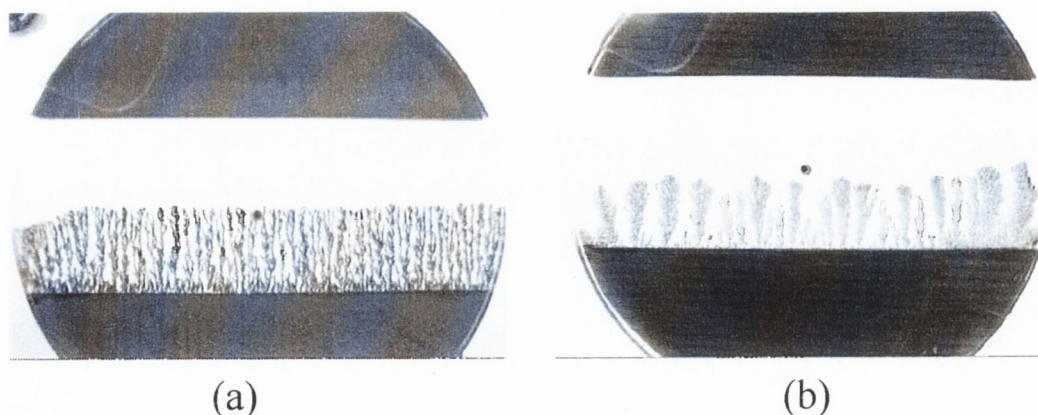


11. Typical fractal electrodeposits with varying morphologies (a) DLA; (b) dense radial; (c) dendritic; (d) stringy.





12. Approximate phase diagram of fractal morphology as a function of applied voltage and ion concentration (after Grier et al).



13. Morphologies of deposits grown between linear electrodes at (a) 15 V, 0.01 M; (b) 5 V, 0.025 M.

### 1.4.2 Linear Electrodes

Electrodeposits have also been grown in similar flat cells, but in linear rather than radial geometries. In this case both anode and cathode are linear electrodes separated by some distance [6][25][26]. Again the electrode/electrolyte system is held between two perspex plates (the purpose of the upper plate is to make the system increasingly two-dimensional, and also to make it portable for image analysis without disturbing the deposit. Deposits may, however, be grown without the use of the upper plate<sup>1</sup>.) Typical resultant morphologies are shown in Fig.13.

Central to the study presented in this thesis, however, is the way in which these flat cell electrodeposits grow in the presence of an externally applied magnetic field.

---

<sup>1</sup> Indeed in some circumstances, notably at applied voltages higher than the reduction potential of hydrogen, it may be necessary to remove the upper plate to allow hydrogen to bubble off so that it does not interfere with the growth of the metal deposit.

### 1.4.3 Magnetic Field Effects

#### Horizontal Circular Electrode Geometry

Magnetic field effects on the morphologies of electrodeposits grown in flat electrochemical cells in the presence of an applied magnetic field were first considered by Mogi et al [27]-[30]. This group concentrated on the effects when the cell was kept horizontal in the presence of a vertical, applied magnetic field. This work was further developed by Hinds et al [31][32] [33] to investigate the effects of magnetic fields applied in and out the plane of electrochemical cells which were held first horizontally and then vertically. The results were, in some cases, quite surprising. Nakabayashi et al have considered similar effects at the liquid/liquid interface [34].

Presented here are some of the patterns observed by Hinds [38]. In each case copper is plated from an electrolytic solution of 0.2 M  $\text{CuSO}_4$  in water. The copper anode has an inner diameter of 22 mm, and a graphite cathode of diameter 0.9 mm is used. A voltage of 6 V is applied between anode and cathode. The magnetic field was applied by placing the electrolytic cell within the bore of a Multimag<sup>2</sup>. In this way magnetic fields in the range 0 – 1 T could be applied to the growing deposit. Where a magnetic field is applied, it is applied for the duration of the growth of the deposit.

---

<sup>2</sup> A Multimag is a permanent magnet variable field source which consists of two nested cylinders. Each cylinder is assembled from segments of permanent magnet material with the magnetization of neighbouring segments oriented such that their combined effect is to produce a uniform field within the bore of the cylinder. Thus by rotating two such nested cylinders relative to each other, magnetic fields continuously variable in both magnitude and direction may be achieved. This system is studied in much greater detail in Appendix A and B.

Firstly we consider cases where the electrolytic cell is kept horizontal. Fig.11(b) is typical of a the dense, radial kind of deposit grown in the absence of an applied magnetic field.

Fig.14(a) demonstrates the effect of a magnetic field of 0.4 T applied out of the plane of the page during the growth. Defined branches emerge in the growth pattern and the fractal is seen to become chiral. That is that the branches tend to arch with some radius of curvature which can be estimated, yielding patterns which look not unlike spiral galaxies.

In Fig.14(b) the direction of the applied magnetic field is reversed to be into the plane of the page. The resulting fractal is similar to that of Fig.14(a), but with an accordingly reversed chirality.

Although the results considered in detail here all involve plating of non-magnetic metals, some interesting work has been carried out by Bodea et al [35] and Imre et al [36][37] on magnetic deposits. In particular, [35] when plating Fe or Co in a flat electrochemical cell in the presence of a magnetic field *in the plane of growth*, the resultant deposit becomes rectangular in shape, with one side of the rectangle parallel to the field direction.

### **Vertical Circular Electrode Geometry**

When a similar cell is held vertically, the deposits produced in the absence of a magnetic field are very different to the comparable horizontal cell result of Fig.14. As shown in Fig.15(a), the basic deposits now tend to grow upwards in a column from the central cathode, with very little growth beneath. The key difference between this and the horizontal set-up, is that gravity is now acting along the length of the cell. This induces natural



(a)



(b)

14. Copper electrodeposits grown (a) with a 0.4 T magnetic field applied *out of* the plane of the page and (b) with a 0.4 T magnetic field applied *into* the plane of the page.

convective flow in the cell which is clearly dominant in this configuration. On applying a magnetic field into the plane of the cell, however, the growth regime changes dramatically and a chiral pattern again results as illustrated in Fig.15(b). This time, however, the chirality of the deposit relative to the direction of the magnetic field is opposite to that of its horizontal counterpart in Fig.14. The chirality of a vertical deposit in a magnetic field is, however, difficult to reproduce. It is neither consistently the same as nor opposite to its horizontal counterpart. Most commonly it is a mixture of both.

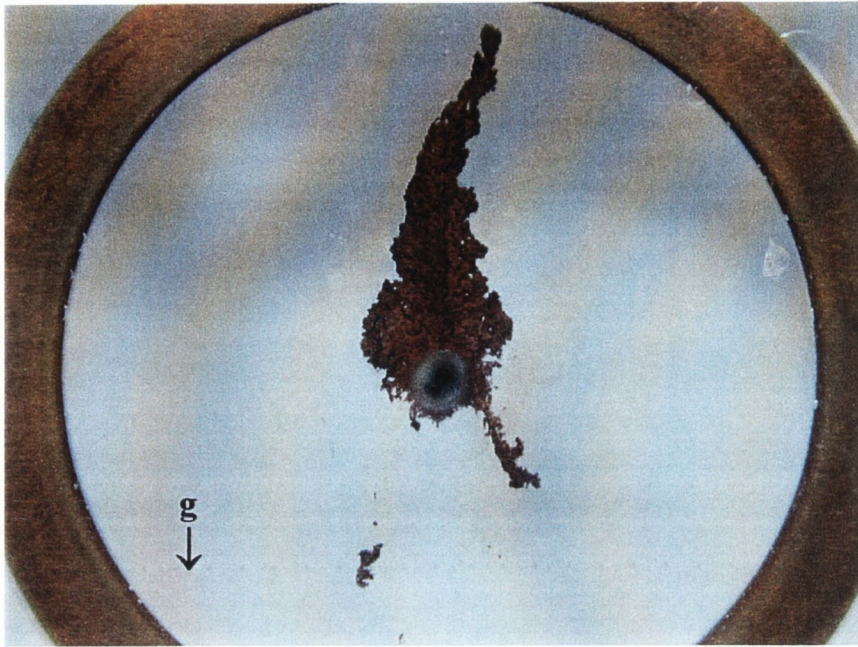
### Linear Electrodes

On growing electrodeposits between linear electrodes, as in Section 1.4.2, patterns of the kind shown in Fig.16 are formed [41]. Similar effects are seen when depositing to a thin wire in the presence of a magnetic field and magnetic field gradient [39][40].

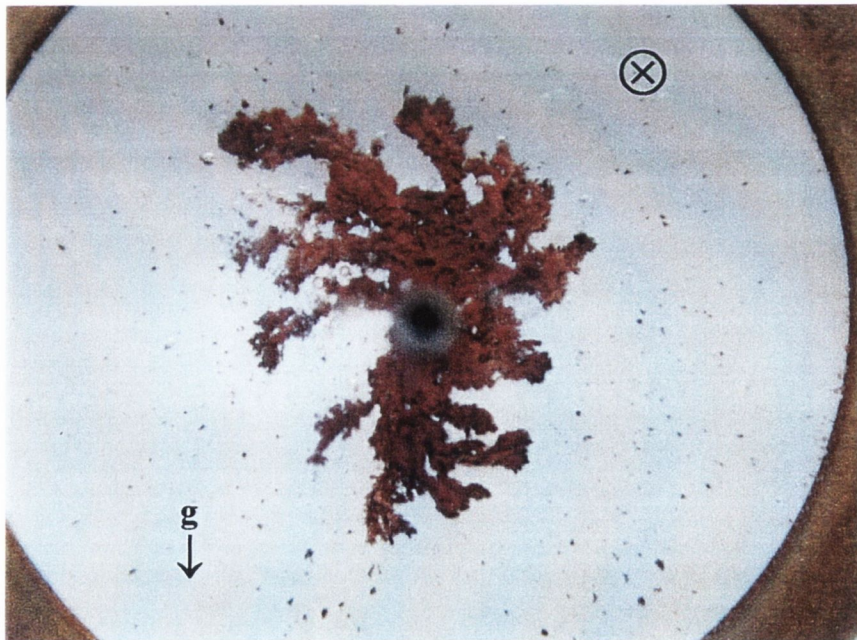
Fig.16(a) indicates the effect of switching on an externally applied magnetic field *out of* the plane of growth as the cell is kept horizontal. The branches begin to tilt to the left-hand side, the direction of the Lorentz force.

The deposit shown in Fig.16(b) was produced under the same conditions, only with the magnetic field applied *into* the plane of growth. The effect of Fig.16(a) is reproduced, but with a reversal of the direction of the magnetic field effect; the branches now tend to lean towards the right hand side.

When deposits are grown in this linear electrode geometry, with the cell held vertically, gravity influences the resultant growth as shown in Fig.17(a). The tentacles of growth tend to tilt slightly upwards, opposite to the direction of  $\vec{g}$ . When a magnetic field is ad-

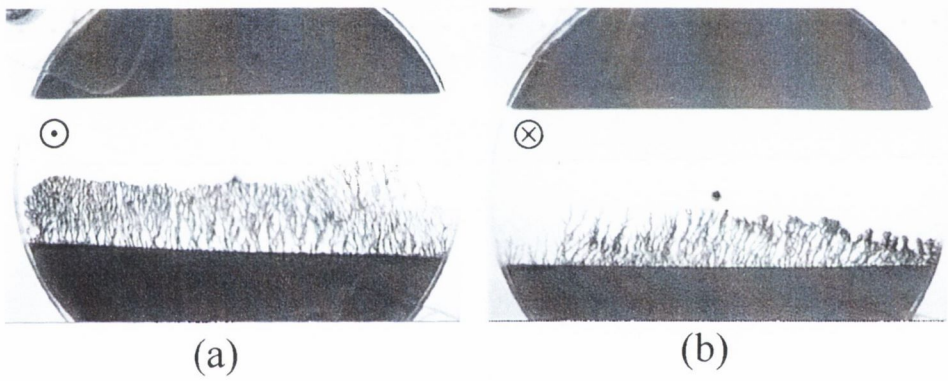


(a)



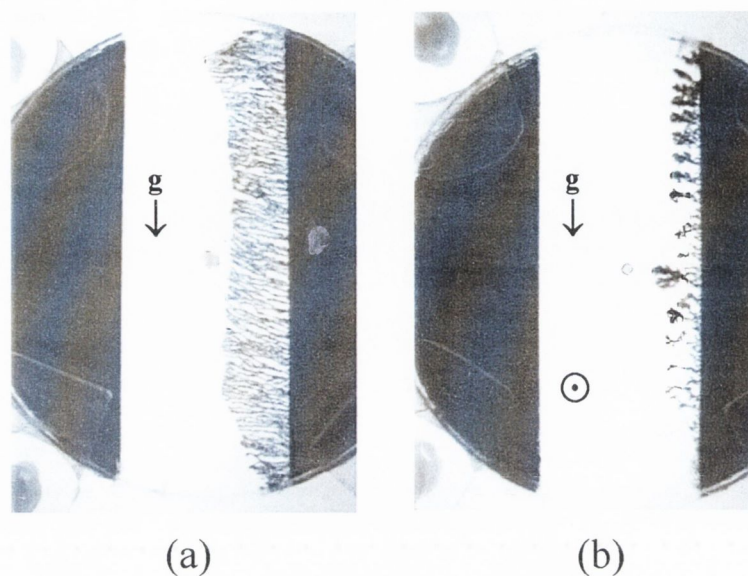
(b)

15. Deposits grown in a flat electrochemical cell held vertically in (a) the absence of an applied magnetic field (b) a magnetic field of 0.4 T applied *into* the plane of the page.



16. Deposits grown in a flat, horizontal electrochemical cell in (a) a 0.35 T magnetic field applied out of the plane of the page and (b) a 0.35 T magnetic field applied into the plane of the page.





17. Deposits grown between linear electrodes in a vertical cell under the influence of (a) gravity alone and (b) gravity combined with an applied magnetic field.

ditionally applied to the vertical cell, the outcome of the competing effects of gravity and magnetic field is somewhat indeterminate as shown in Fig.17(b).

## 1.5 Principles of Electrochemistry

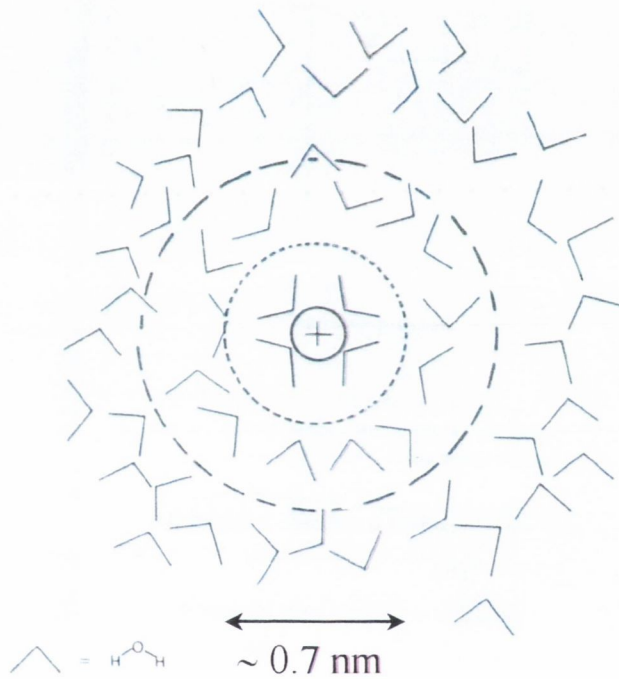
Before we can begin to interpret the mechanisms of the interplay between magnetic field effects and electrochemical processes, we must first outline some general principles of electrochemistry. For much of this section, thanks is due to the assorted, received wisdom of a number of invaluable sources [42]-[47].

### 1.5.1 Electrolytes

In an electrochemical system current is passed between two electrodes via an electrolyte. An *electrolyte* is a substance that dissolves in a solvent to produce a conducting solution of ions. Here the term electrolyte is also taken to refer to the solution as a whole. Unless otherwise stated, water is generally taken to be the solvent. Other solute species such as acids may also be used or added if, for example, the desired effect is to reduce migration effects (Section 1.5.4). When a salt is immersed in a solvent, the extent of its ionisation classifies the electrolyte as either strong or weak. Immersed in water, the salt is first ionised, and then *hydrated* by water molecules which are dipolar due to their strong hydrogen bonds. The dipolar water molecules tend to orient themselves around an ion in solution as in Fig.18. So when considering ions as objects that move through a solution, we actually must consider the larger unit of the ion together with its surrounding *hydration sphere* of water. This structure is more stable than the naked ion, and may consist of two to three layers of water molecules.

### 1.5.2 Electrode Potential

Electrochemical reactions occur at the interface between the electrolyte solution and an electrode surface. An electrode can act as either a source or a sink of electrons for the surrounding electrolyte. In the process of *reduction*, electrons are supplied from the electrode to neutralise positively charged ions in solution; while *oxidation* takes place when electrons are transferred from a negatively charged ion to the electrode. Such reactions are described



18. Due to the dipolar nature of water, water molecules orient themselves around an ion in solution with them. The ion must thus be considered together with its hydration sphere (Hibbert, 1993).

by



where  $O$  and  $R$  are the oxidised and reduced species respectively. In many systems relevant to the present study, the oxidation reaction consists of the dissolution of metal  $M$  from the surface of the electrode



In order for electron transfer to take place, there must be a correspondence between the energy of the orbital of the valence electron to be transferred to or from the ion in solution, and the Fermi energy level<sup>3</sup> of the metal electrode. The Fermi energy level  $E_f$  in the electrode can be adjusted by applying an external potential  $U$ , remembering that the two are related by

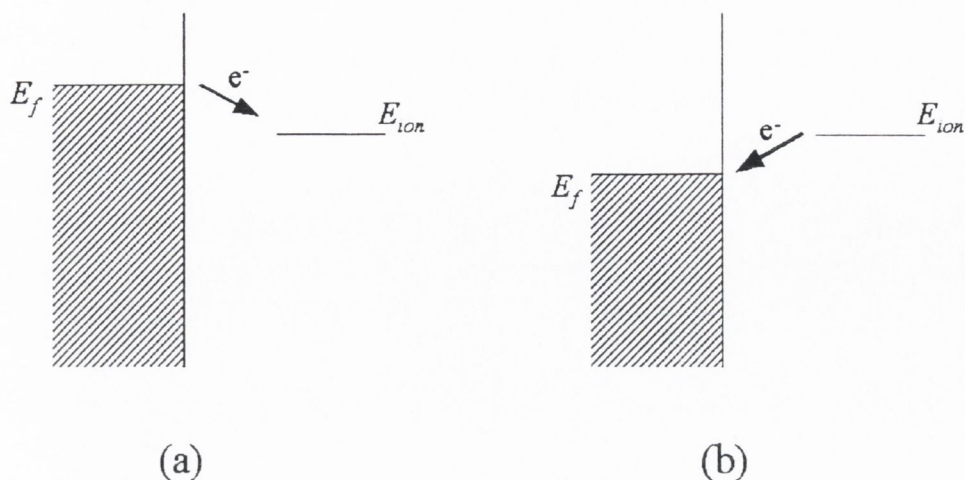
$$E_f = -eU. \quad (1.9)$$

For reduction to take place, electrons must drop from the Fermi level of the electrode to a lower orbital energy level available on an ion in solution. The electrode Fermi energy must therefore have a certain minimum value before electrons can be transferred. This may be achieved applying a sufficiently negative potential to the electrode. This negative electrode is then known as the *cathode*.

For oxidation, on the other hand, electrons must drop from their ionic orbital energy level in solution to the Fermi level in the electrode. Thus there is a maximum energy that the lowest unoccupied energy level on the electrode can have. This is maintained by applying a sufficiently positive potential to the electrode. The positive electrode is known

---

<sup>3</sup> In a metal, the Fermi energy level is the highest electronic energy level occupied by an electron.



19.(a) When a negative potential is applied to a metal electrode the Fermi energy level is raised, facilitating *reduction* of an ion. (b) Applying a positive potential to the electrode lowers its Fermi level and facilitates *oxidation* of an ion.

as the *anode*. Thus applying a suitable potential difference between the anode and cathode, electron transfer can be achieved at both electrodes as shown in Fig.19.

### 1.5.3 Reaction Kinetics

The value of the electrode potential thus determines whether or not a reduction or an oxidation reaction can take place. It is important to note that an electrode has a certain equilibrium potential even in the absence of an externally applied potential. This is known as the formal potential  $U^{\circ}$ , usually measured relative to the normal hydrogen electrode (NHE). In dynamic electrochemistry, the absolute value  $U$  of the electrode potential is not the relevant parameter. Rather we are interested in its value relative to the standard electrode

potential, known as the *overpotential*,  $U - U^\ominus$ . This value determines not only the conditions under which an electrochemical reaction can take place, but also determines the speed with which the reaction proceeds. Thus the *reaction kinetics* are determined by the applied voltage.

The mechanism of electron transfer at an electrode occurs in a number of well defined steps:

1. The ionic species must move through the solution to the solution/electrode interface. The speed of this mass transfer is determined by the mass transfer coefficient  $k_d$ .
2. The ionic atmosphere in the vicinity of the interface is rearranged in response to the new addition. This takes  $\sim 10^{-8}$  s.
3. The solvent dipoles associated with the central ion are reoriented in response to the charged electrode surface. This takes  $\sim 10^{-11}$  s.
4. Distances between the central ion and the ligands are adjusted. This takes  $\sim 10^{-14}$  s.
5. The electron is transferred. This takes  $\sim 10^{-16}$  s.

Steps 2-5 are all considered under the umbrella of reaction kinetics, which are quantified by the charge transfer rate constants  $k_a$  and  $k_c$  at the anode and cathode respectively.  $k_a$  and  $k_c$  are determined by the overpotential according to

$$k_a = k_0 \exp [\alpha_a n F (U - U^\ominus) / RT] \quad (1.10a)$$

$$k_c = k_0 \exp [-\alpha_c n F (U - U^\ominus) / RT] \quad (1.10b)$$

If the reaction kinetics are slow compared to the rate of mass transfer, that is if ions are arriving at the electrode more quickly than they can react, then the reaction is said to be in the **activation regime**.

### 1.5.4 Mass Transfer : Diffusion, Convection and Migration

Step 1 in the sequence leading up to charge transfer is *mass transfer*, the transport of species between the electrode surface and the bulk solution. This transport can take place by a combination of three mechanisms: diffusion, convection and migration. The rate of mass transfer is monitored by the *mass transfer coefficient*  $k_d$ . When the speed of the reaction kinetics is large compared to the rate of mass transfer, the reaction is said to be **mass transport limited**. Parameters relevant to mass transport, together with their units and typical values are summarised in the table.

Quantity	Typical Value	Units
Flux, $J$	$\sim 5 \times 10^{-4}$	$\text{mol m}^{-2} \text{s}^{-1}$
Current density, $j$	$\sim 1000$	$\text{A m}^{-2}$
Concentration, $c$	$\sim 100$	$\text{mol m}^{-3}$
Diffusion constant, $D$	$\sim 1 \times 10^{-9}$	$\text{m}^2 \text{s}^{-1}$
Viscosity, $\nu$	$\sim 1 \times 10^{-6}$	$\text{m}^2 \text{s}^{-1}$
Voltage	$\sim 1$	V
Velocity, $U$	$\sim 1 \times 10^{-2}$	$\text{m s}^{-1}$
Temperature	293	K
Ionic charge number, $n$	1, 2, 3...	
Faraday constant, $F$	= 96485.309	$\text{C mol}^{-1}$
Gas constant	8.314510	$\text{J mol}^{-1} \text{K}^{-1}$

Table 1 : Typical values and units of quantities and physical constants relevant in an electrochemical cell.

### Diffusion

*Diffusion* is the natural movement of a species, whether charged or neutral, due to a gradient in its concentration  $c$ . Material is swept through the concentration gradient from regions of high concentration to regions of low concentration. In the case of the movement of charged species, a net flux  $\mathbf{J}$  of the species in the vicinity of an electrode with normal  $\hat{\mathbf{n}}$  results in a net current  $i$  flowing through the electrode with current density  $j$  ( $= i/A$ ) where  $A$  is the area of the electrode through which the current is flowing), according to

$$j = nF\mathbf{J}\cdot\hat{\mathbf{n}} \quad (1.11)$$

where  $n$  is the number of unpaired electrons on the ion, and  $F$  is the Faraday constant,  $F = 96,500 \text{ Cmol}^{-1}$ . The flux  $\mathbf{J}$  of a species is the number of moles passing normally across a plane of unit area in unit time, and is measured in units of  $\text{mol m}^{-2}\text{s}^{-1}$ .

The net flux  $\mathbf{J}$  of a species through a concentration gradient is given by Fick's first law

$$\mathbf{J} = -D\nabla c \quad (1.12)$$

where  $D$  is a constant for a given material known as the *diffusion coefficient*. The rate of change of the concentration is related to the flux gradient by

$$\frac{\partial c}{\partial t} = -\nabla\cdot\mathbf{J} \quad (1.13)$$

leading to the expression of Fick's second law as

$$\frac{\partial c}{\partial t} = D\nabla^2 c \quad (1.14)$$

where  $\nabla^2$  is the Laplacian operator<sup>4</sup>.

<sup>4</sup> The Laplacian (del-squared) operator is given by  $\nabla^2 f = \frac{\partial^2 f}{\partial x^2} + \frac{\partial^2 f}{\partial y^2} + \frac{\partial^2 f}{\partial z^2}$  in Cartesian coordinates.



Note that at steady state, Eq.1.13 reduces to a conservation equation for current density

$$\nabla \cdot \mathbf{J} = 0 \quad (1.15)$$

### Convection

When, in addition to diffusion, a *convective* flow with velocity  $v$  is present in the fluid, then Fick's law is modified to give a net flux

$$\mathbf{J} = c\mathbf{v} - D\nabla c. \quad (1.16)$$

In this case, the first term on the right-hand side indicates the fact that mass transport is also achieved when species are moved along within a flow of velocity  $\mathbf{v}$ . In the case of charged particles reacting electrochemically with an electrode, the current density is directly enhanced by direct substitution of Eq.1.16 into Eq.1.11 if  $\mathbf{v}$  has some component which directs the ions towards the electrode surface. In the case where  $\mathbf{v}$  is parallel to the electrode surface, there is no direct convective mass transfer to the electrode. The current density can, nonetheless, be indirectly enhanced as will be outlined in Sec.1.6.

Fick's second law is accordingly adapted from Eq.1.16 and Eq.1.13, to give

$$\frac{\partial c}{\partial t} = -\mathbf{v} \cdot \nabla c + D\nabla^2 c. \quad (1.17)$$

### Migration

In the case of *migration*, ions move through a solution under the influence of an external electrical potential applied between two electrodes. In the presence of an electric field of strength  $\mathbf{E} = -\nabla V$  (measured in units  $\text{Vm}^{-1}$ ), the net flux of a species due to the

combined effects of diffusion and migration is

$$\mathbf{J} = -D\nabla c - nc \frac{FD}{RT} \mathbf{E}. \quad (1.18)$$

The second term on the right hand side of Eq.1.18 derives from a number of considerations. The net flux of ions with concentration  $c$  moving with velocity  $\mathbf{v}$  is given by

$$\mathbf{J} = c\mathbf{v}. \quad (1.19)$$

Neglecting retarding effects, the maximum velocity  $\mathbf{v}$  achievable by an ion in an electric field  $\mathbf{E}$  is limited by

$$\mathbf{v} = u\mathbf{E} \quad (1.20)$$

where the ion mobility  $u$  is the proportionality coefficient between  $\mathbf{v}$  and  $\mathbf{E}$ . Finally, the diffusion constant for a given ionic species is closely related to both temperature and the mobility of the ion by the *Einstein equation*

$$D = \frac{uRT}{nF}.$$

where  $R$  is the gas constant and  $T$  is temperature.

In the system considered in the Chapters 4 and 5 the electrolyte solution contains large quantities of acid. The ions from the acid serve to shield the metallic ions from the electrode potential, at all but very small distances from the electrodes. In this system, therefore, migration can be largely neglected. In the case of the flat electrochemical cells of Chapters 2 and 3, however, there is no acidic supporting electrolyte present, and so migration must be considered.

### 1.5.5 Diffusion Layers and Natural Convection

Of the processes outlined in Sec.1.5.4, the most relevant to us here is diffusion. Diffusive mass transfer is achieved when material is swept through a concentration gradient from a region of high concentration to a region of low concentration. So we must consider the concentration gradients arising in an electrochemical cell. The electrodes are immersed in an electrolyte which contains a bulk concentration  $c_\infty$  of a given ionic species. If that species reacts at the electrode, and assuming that the reaction kinetics are sufficiently fast that the reaction takes place immediately on the ion reaching the electrode surface, the concentration  $c_0$  of that ionic species at the electrode surface is zero. Thus a concentration gradient arises in the vicinity of the electrode as the concentration varies from  $c_0$  on the surface to the bulk value of  $c_\infty$  some small distance away.

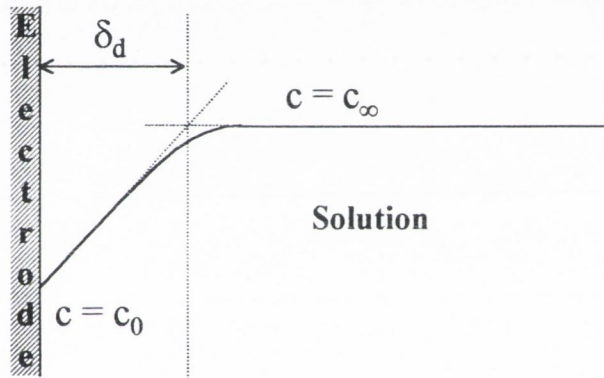
The concentration profile is not strictly linear, and the concentration gradient actually tends asymptotically to zero at large distances from the electrode surface as shown in Fig.20.

Nonetheless, a linear approximation can be used to estimate the thickness  $\delta_d$  of the diffusion layer, so that the one dimensional concentration gradient may be given as

$$\frac{\partial c}{\partial y} = \frac{c_\infty - c_0}{\delta_d}. \quad (1.21)$$

Fick's first law

$$j = nFD \frac{\partial c}{\partial y}$$



20. After an initially steep concentration gradient at the electrode surface, the concentration gradient tends asymptotically to zero at large distances from the electrode surface. A linear approximation for the concentration profile can be used, however, to estimate the diffusion layer thickness  $\delta_d$ .

from Eqs.1.11 and 1.12, may thus be simplified so that the diffusive current density is given by

$$j = nFD \frac{c_{\infty} - c_0}{\delta_d}. \quad (1.22)$$

Thus the thickness of the diffusion layer is the essential parameter in determining the current density in the mass-transport limited regime. The value of  $\delta_d$  is limited by natural convection, and may be controlled by forced convection. The latter mechanism will be examined in Sec.1.6.

At the onset of an electrochemical reaction, a concentration gradient is established at the electrode surface. As the reaction proceeds it 'eats' further and further into the supply of ions from the bulk solution, and the diffusion layer widens accordingly. This also establishes, however, density gradients between the ion-rich and ion-poor regions of the electrolyte which results in gentle churning (convection) of the electrolyte at the edge of the diffusion layer. After some time  $t$ , the thickness of the diffusion layer becomes limited by these natural convective effects. This growth of the diffusion layer thickness is given by

$$\delta_d = \sqrt{\pi Dt} \quad (1.23)$$

where, depending on the solution and the orientation of the electrode surface, a limiting value for  $\delta_d$  is typically reached after a time  $t$  of the order of 30–60 s. Since  $D \sim 1 \times 10^{-9} \text{ m}^2\text{s}^{-1}$  (Table 1) it follows that  $\delta_d$  is typically  $\sim 300 \mu\text{m}$  thick when the limiting current is reached.

This also establishes that in the absence of forced convection, a value may be determined for the *limiting diffusion current density* that is

$$j_d(t) = \frac{nFD^{1/2}(c_\infty - c_0)}{(\pi t)^{1/2}} \quad (1.24)$$

This is known as the *Cottrell equation*.

## 1.6 Magnetohydrodynamics

Hydrodynamics is the study of fluid flow [49], [50]. It considers patterns which evolve in fluid flows, particularly when the fluid is interacting with solid objects in its path. It is guided by a number of essential principles and equations from which analytical solutions may be derived for the most simple geometries, but which also lend themselves to solution by numerical techniques for more complex scenarios. Hydrodynamics essentially considers the result of competition between internal friction within the fluid (viscosity) and friction between the fluid and a solid surface (the ‘no-slip’ condition) on the one hand, and a driving force such as a pressure gradient, gravity or some externally applied force on the other hand. Resultant velocity profiles vary widely from system to system.

Hydrodynamics becomes ‘*magnetohydrodynamics*’ in the presence of an applied magnetic field, when a force influencing the fluid flow is the *Lorentz force* on charged particles within the solution or conducting melt.

### 1.6.1 Principles of Hydrodynamics

#### Continuity and Navier-Stokes Equations

The fluids considered in this study are incompressible liquids, and for such liquids the following equation of continuity of momentum holds

$$\nabla \cdot \mathbf{v} = 0. \quad (1.25)$$

This is simply a restatement of the law of conservation of matter, insisting that flowing fluid which enters a region of space must all re-emerge from that region of space. Fluid cannot be created or destroyed (or compressed) at any point.

The velocity profile for a given flow is monitored by the Navier Stokes equation

$$\frac{D\mathbf{v}}{Dt} = -\frac{1}{\rho}\nabla p + \nu\nabla^2\mathbf{v} + \frac{\mathbf{f}}{\rho} \quad (1.26)$$

where  $p$  is pressure (in units  $\text{kg m}^{-1}\text{s}^{-2}$ ),  $\rho$  is density ( $\text{kg m}^{-3}$ ),  $\nu$  is kinematic viscosity ( $\text{m}^2\text{s}^{-1}$ ) and  $\mathbf{f}$  is the sum of any other externally applied forces (per unit volume, measured in units  $\text{kg m}^{-2}\text{s}^{-2}$ ), which may include gravity and/or the Lorentz force. Eq.1.26 is essentially just a detailed expression of Newton's second law of motion  $\mathbf{a} = \mathbf{F}/m$ . That is to say that the *resultant* force experienced by the fluid (terms on the left hand side) is the vector sum of the applied forces (on the right-hand side). Given that the velocity may vary not only in time, but also with position in the fluid we can write out the acceleration as the full partial derivatives of the velocity field, which casts Eq.1.26 as

$$\frac{\partial\mathbf{v}}{\partial t} + \frac{\partial\mathbf{x}}{\partial t}\frac{\partial\mathbf{v}}{\partial x} + \frac{\partial\mathbf{y}}{\partial t}\frac{\partial\mathbf{v}}{\partial y} + \frac{\partial\mathbf{z}}{\partial t}\frac{\partial\mathbf{v}}{\partial z} = -\frac{1}{\rho}\nabla p + \nu\nabla^2\mathbf{v} + \frac{\mathbf{f}}{\rho}, \quad (1.27)$$

$$\text{i.e. } \frac{\partial\mathbf{v}}{\partial t} + (\mathbf{v} \cdot \nabla)\mathbf{v} = -\frac{1}{\rho}\nabla p + \nu\nabla^2\mathbf{v} + \frac{\mathbf{f}}{\rho} \quad (1.28)$$

### Viscosity

The *kinematic viscosity*  $\nu$  relates to the *viscosity*  $\mu$  and the density  $\rho$  by

$$\nu = \frac{\mu}{\rho} \quad (1.29)$$

where the viscosity  $\mu$  is a measure of the internal friction within a fluid; that is the friction between adjacent ‘layers’ of the fluid as they move relative each other. In a liquid in which this internal friction is high, the fluid does not flow easily. Such a fluid is said to be very viscous; an example would be glycerine. When  $\nu$  is low, on the other hand, the fluid flows with ease. Examples of less viscous fluids are air and water.

One very important consequence of viscosity is the friction that it generates between a solid object and the layer of fluid in contact with its surface. As a fluid flows past the solid surface, the layer of fluid particles immediately adjacent to the surface adhere to it and remain motionless. The stationary layer may be several molecular layers thick. This ‘no-slip’ condition of

$$\mathbf{v} = 0 \quad (1.30)$$

at the boundary with any solid object, sets essential boundary conditions for solving equations 1.25 and 1.27.

### Characteristic Numbers

Hydrodynamic flow is typically classified in terms of its Reynolds Number  $Re$

$$Re = \frac{Ud}{\nu} \quad (1.31)$$



for flow with velocity  $U$  of a fluid with viscosity  $\nu$  past a plate of length  $d$ . The dimensionless Reynolds number gives a strong indicator of the kind of flow expected from a given system. The particular critical value of  $Re$  varies somewhat from system to system, but for flow past a flat plate, if  $Re < 2000$  then the flow regime is laminar. For  $Re > 2000$ , however, the flow becomes turbulent.

The Schmidt number

$$Sc = \frac{\nu}{D} \quad (1.32)$$

is characteristic of the medium with  $\nu$  and  $D$  primarily representing the properties of the solvent and ionic species respectively. Typically  $Sc \sim 10^3$  for an aqueous solution (Table 1). The Peclet number,

$$Pe = \frac{Ud}{D} = Re.Sc \quad (1.33)$$

on the other hand, represents the relative contributions of convection and diffusion to the transport process.

## 1.6.2 Magnetohydrodynamics

A particle carrying electric charge  $q$ , moving with velocity  $\nu$  in a magnetic field  $B$  experiences a force  $\mathbf{F}_{Lor}$

$$\mathbf{F}_{Lor} = q\mathbf{v} \times \mathbf{B} \quad (1.34)$$

known as the Lorentz force.

Current  $i$  is simply a transfer of charge per unit time, and thus current density  $j$  may be defined as

$$j = \frac{i}{A} = \frac{1}{A} \frac{dq}{dt} \quad (1.35)$$

where  $A$  is the area through which the current is passing. In the case of electrodeposition,  $A$  is the area over which ions are plating. We may thus, from Eq.1.34, define a force per unit volume to quantify the effect on a current density  $j$  of an applied magnetic field  $B$ ,

$$\mathfrak{S}_{Lor} = \mathbf{j} \times \mathbf{B} \quad (1.36)$$

In the case that  $\mathbf{B}$  is not applied parallel to  $\mathbf{j}$ , then this Lorentz force will tend to induce motion of the ions perpendicular to both  $\mathbf{j}$  and  $\mathbf{B}$ . As a result of the large hydration spheres about each ion, this induces bulk flow of the surrounding solution. Hydrodynamic flow develops in the system. The induced velocity profile may be determined by considering the Navier-Stokes equation 1.27 with the inclusion of Eq.1.36,

$$\frac{\partial \mathbf{v}}{\partial t} + (\mathbf{v} \cdot \nabla) \mathbf{v} = -\frac{1}{\rho} \nabla p + \nu \nabla^2 \mathbf{v} + \frac{\mathbf{j} \times \mathbf{B}}{\rho}. \quad (1.37)$$

This fluid flow sets up hydrodynamic boundary layers at solid surfaces due to the 'no-slip' condition of Eq.1.30. In particular, fluid flow past the electrode surface replenishes the diffusion layer, increasing the supply of ions to the electrode. The thickness  $\delta_d$  of the diffusion layer is decreased and the value of  $j$  may thus be enhanced.

### 1.6.3 Electrokinetic Effect

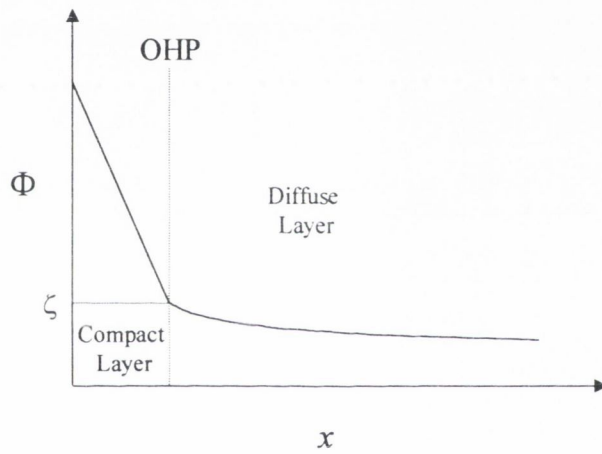
An alternative hypothesis for the mechanism behind the magnetic field effect, is that of the electrokinetic effect [51]. A number of distinct electrokinetic phenomena occur when a solid phase with a surface charge moves relative to a liquid electrolyte phase. In each case either an applied electric field induces movement, or movement induces an electric field. Particles with a surface charge, for example, may be forced to move though an elec-

trolyte under an applied electric field (electrophoresis). Alternatively a potential difference may be induced across the particle when it is forced to move through the electrolyte under a gravitational force (sedimentation potential). In the case where it is the liquid phase which is mobile, if the electrolyte is forced to flow (under pressure for example) parallel to a charged solid interface, a potential difference is established at the interface (the streaming potential) between two points upstream and downstream of the flow. The fourth electrokinetic condition occurs when an electric field  $E_{\parallel}$  parallel to the solid-liquid interface induces movement of the electrolyte parallel to the surface. This is known as electro-osmosis. In this case the electrolyte experiences a force

$$F = \sigma E_{\parallel} \quad (1.38)$$

where  $\sigma$  is the conductivity of the solution.

To appreciate the region in which these effects are relevant, we must consider the nature of the so-called ‘*double-layer*’ at the interface between the conducting phases, in our case the metal-electrolyte interface. When an electrode is immersed in an electrolyte, any excess charge on the surface must, for electroneutrality, be exactly balanced by an equal charge of opposite sign on the solution side of the interface. Thus any ion exchanging an electron at the surface is cushioned from the electrode surface, so that the nearest reacting ion is at a distance from the electrode on a plane known as the Outer Helmholtz plane (OHP) which is  $\sim 1$  nm from the surface. The potential falls off rapidly within the compact layer inside the OHP, to a value known as the *zeta-potential*  $\zeta$ . Beyond this compact layer, the potential decays exponentially to zero in the diffuse layer as indicated in Fig.21.



21. Potential falls off rapidly within the compact layer  $\sim 1$  nm from the electrode surface, and then approximately exponentially into the diffuse layer. At the OHP the potential is known as the zeta-potential.

So when, as in the case of electro-osmosis, flow of electrolyte is induced along a surface, it in fact occurs along a shear plane just beyond the ions immediately attached to the surface. In the case of our system, it has been proposed by Olivier et al [51] that in the presence of an applied magnetic field, an electric field  $E_x$  is established parallel to the electrode surface as a result of the interaction between the current density  $j$  plating in the  $y$ -direction and the applied magnetic field  $B$  in the  $z$ -direction. This, by electro-osmosis, induces a flow of electrolyte parallel to the surface, just beyond the OHP. This represents a significant force in the system [52]. Furthermore, it is their contention that this effect alone is sufficient to account for the magnetic field effects on electrodeposition as the observed effects persist when the magnetic field is concentrated on the immediate vicinity of the electrode alone [53]. This is further justified by the same group by their claim that similar convective effects may be reproduced in the absence of a magnetic field by directly creating an electric field  $E_x$  parallel to the electrode surface .

## 1.7 Numerical Approaches

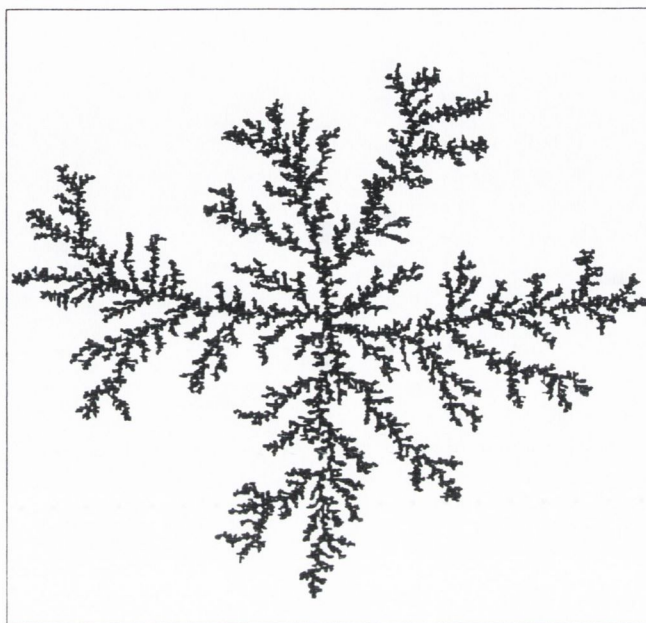
The development of a science of fractal geometry has been inextricably linked with numerical simulation since its inception. The famous Mandelbrot set [1] generated beautiful fractal images which have been simulated and represented with stunning colours which captured the world's imagination. Though some such models amount to little more than mathematical and numerical curiosities, many more practical models have been developed to represent a variety of physical processes. Percolation models, for example [55][56], have been applied to the modelling of systems such as polymer gels, galaxy evolution and formation of colloidal particles, while cluster growth models such as the Eden model [57] was originally applied to the problem of the growth of biological cell colonies, and has been used as a model for the development of skin cancer [58].

The particular model which interests us for the present application, also based on cluster growth, is the diffusion limited aggregation model.

### 1.7.1 The Diffusion Limited Aggregation (DLA) Model

This enigmatic model has, for years, been applied to problems in electrodeposition. It has proved particularly successful in reproducing the structures produced in the growth of metal electrodeposits between two flat horizontal sheets of the kind shown in Fig.11(a).

In its simplest form as introduced by Witten and Sander [59] the DLA model is essentially a random walk model. The simulation is carried out on an  $N \times N$  lattice. Lattices are most typically square, although triangular and hexagonal lattices are also common. At the outset of the simulation, a site at the centre of the lattice is occupied, to represent the cen-



22.A typical computer generated DLA structure.

tral cathode. A particle is then introduced at a random position on the lattice, representing a metal ion. This particle moves through the lattice with equal probability  $\frac{1}{4}$  of walking up, down, left or right (for a square lattice) at each step. When the particle eventually moves to a site which has an occupied nearest-neighbour, it sticks to the aggregate. Another particle is introduced to the lattice and the process repeats while the deposit is growing. Structures of the type shown in Fig.22 are generated by this process.

Despite its simplicity, and its obvious ability to reproduce planar electrochemical structures, the underlying theory behind the success of the DLA model remains elusive

[60]. The DLA model essentially amounts to a numerical attempt to discretize the solution of the Laplace equation that underpins the problem, as outlined in the following section.

### The Mullins-Sekerka Instability

Perhaps the most striking thing about DLA-like patterns is the way in which they do, or more accurately *don't*, fill space. Conceptually it may seem reasonable that a surface which is initially rough may develop in a DLA-like manner. New particles will tend to stick to the protruding regions, thus screening the interior from further growth. Important to understand, however, is that a small instability on a surface which is initially smooth can develop into a protrusion which will ultimately result in a DLA structure.

This result can be outlined by casting the DLA problem in continuum terms as is clearly summarized in [60]. Let us assume that particles with a continuous density  $u(\mathbf{r}, t)$  diffuse towards some smooth surface, and stick to the surface on their arrival. The particles move according to Fick's second law of diffusion (Eq.1.14)

$$\frac{\partial u}{\partial t} = D \nabla^2 u \quad (1.39)$$

and the normal velocity of growth  $v_n$  of the surface is proportional to the flux of material onto it

$$\frac{\partial u}{\partial n} \propto v_n. \quad (1.40)$$

Furthermore, we can estimate  $\partial u / \partial t \propto v \partial u / \partial x$ , so that

$$|\nabla^2 u| \approx \frac{v}{D} \frac{\partial u}{\partial n}. \quad (1.41)$$

As the deposit grows, however, the fact that the basic DLA model releases only one particle per cycle reduces the growth velocity to zero. Under these conditions, Eq.1.41 is



reduced to the Laplace equation

$$\nabla^2 u = 0 \quad (1.42)$$

with the surface boundary condition that the particles stick to the surface immediately on arrival, so that the surface density  $u_s$

$$u_s = 0. \quad (1.43)$$

Far from the surface, the density tends to some finite value  $u \rightarrow u_\infty$ . This is known as the *Laplacian growth regime*, where the diffusion constant is irrelevant to the growth. These equations can equally be considered as identifying a problem in electrostatics where the surface of the deposit grows with a velocity proportional to the electric field (potential gradient, Eq.1.40) at that point.

Eq.1.42 and 1.43 might be expected to describe a system which grows uniformly from a smooth surface. The Mullins-Sekerka instability [62], however, identifies the way in which a small non-uniformity on the surface can result in the growth of a highly non-uniform deposit. If a small bump is present on a flat, equipotential surface, the value of the electric field will be largest in the vicinity of the bump. From Eq.1.40 the velocity of growth from this tip will be greater than from the flat regions of the surface. This further enhances the size of the bump, and also the extent of its effect on its surroundings. Furthermore, if a non-uniformity develops on the bump itself, the branches of enhanced growth may split. The outline of the developing deposit thus rapidly deviates from its initially smooth surface.

This simplification of the problem to a Laplace equation in Eq.1.42 results in a straightforward numerical implementation of the problem. The Laplace equation

$$\left( \frac{\partial^2}{\partial x^2} + \frac{\partial^2}{\partial y^2} \right) u = 0$$

may be represented on a square lattice of sites  $(i, j)$  separated from each other by  $\Delta$ , by the finite equation

$$\frac{u(i+1, j) + u(i-1, j) - 4u(i, j) + u(i, j-1) + u(i, j+1)}{4\Delta^2} = 0$$

where  $\Delta x = \Delta y = \Delta$ . Therefore

$$u(i, j) = \frac{u(i+1, j) + u(i-1, j) + u(i, j-1) + u(i, j+1)}{4}. \quad (1.44)$$

We now note the similarity between Eq.1.44 and Eq.1.45

$$P(i, j) = \frac{P(i+1, j) + P(i-1, j) + P(i, j-1) + P(i, j+1)}{4} \quad (1.45)$$

for the probability that a random walker will be found at site  $(i, j)$  on a square lattice, expressed in terms of the probabilities of finding it at each of the four neighbouring sites.

Thus the Laplace model can be modelled by a random walker model, where  $P(i, j)$  is proportional to the scalar field  $u(i, j)$ .

This argument outlines the essential principle of the DLA model. Its basic structure may be accessibly elaborated, however, by varying  $P(i, j)$  to include more of the physical parameters that may be relevant in a given system, such as applied voltage, finite concentration and for our purposes an applied magnetic field. Chapter 2 presents these modifications in greater detail.

# Chapter 2

## Adapted DLA Model

One of the most intriguing features of the success of original DLA model [59] is not only the remarkable similarity between its results and those of real electrochemical experiments, but the fact that this similarity may be achieved without the input of any of the physical details of the system into the model. Sec.1.7.1 accounts for some similarity between the discrete DLA model and a Laplacian problem in electrostatics. Real systems, however, involve variables such as applied voltage [67], concentration (more than one particle moving simultaneously), concentration gradients, reaction kinetics, gravity and, most importantly for this study, applied magnetic field [69] [70][71]. This section demonstrates ways in which the basic DLA model can be adapted by introducing preferential drifts to incorporate these various effects for both circular and linear electrode flat cell geometries. Firstly though, standard techniques for optimising the basic DLA model are outlined.

### 2.1 Horizontal Circular Electrode Geometry

#### 2.1.1 Speeding Up the Basic Model

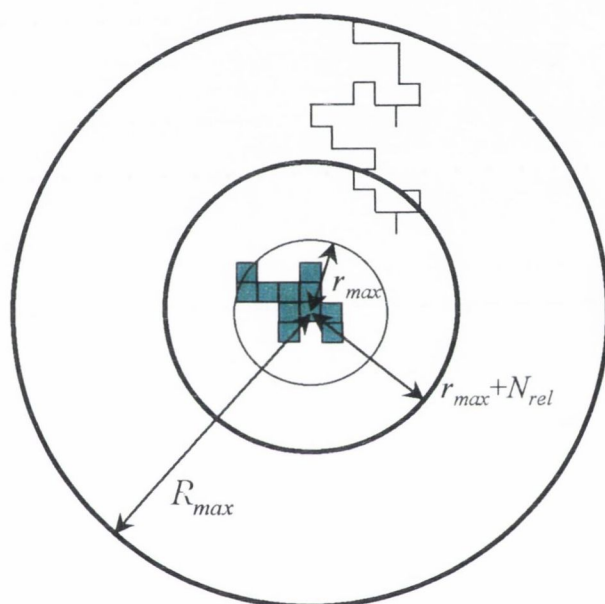
The basic DLA model introduced in Sec.1.7.1 begins by occupying a seed site at the centre of an  $N \times N$  two-dimensional square lattice. A second particle is introduced at a random point on the lattice and moves about with equal probability  $\frac{1}{4}$  of moving up, down, left or right until it neighbours the occupied site at which point it sticks. Another particle is

randomly introduced and the process is repeated. The first problem with this basic model is that it is unnecessarily time consuming. If the new particle begins at some distance from the aggregate, it may walk around for any arbitrary number of steps and never reach the deposit at all. Instead it may eventually walk off the lattice, so that another new particle must be introduced and the process starts over, with no promise of success.

Of the ions in a real solution, those that are deposited at the electrode are those within the diffusion layer at a given time. Ions in the bulk solution cannot deposit until they are gradually queued from the bulk through to the diffusion layer. Thus it is sufficient numerically to consider only particles which begin their random walk close to the deposit. So as the deposit grows, its maximum radius  $r_{\max}$  is at all times recorded. A release radius  $R_{rel}$  for new particles is thus defined at

$$R_{rel} = (r_{\max} + N_{rel}) \quad (2.46)$$

where  $N_{rel}$  is some number of lattice spacings. In the results presented here  $N_{rel} = 10$ . So each new particle begins its trajectory from the lattice site nearest to a point at some randomly chosen angle on a circle of radius  $R_{rel}$  from the initial seed site. Furthermore, if a particle walks too far from the deposit time is unproductively spent waiting for it to return to the area of interest. Thus a maximum radius  $R_{\max}$  about the initial site is defined (dynamically, so that  $R_{\max}$  scales with the growth of deposit). If a particle moves beyond  $R_{\max}$ , it is terminated and a new particle is randomly introduced at  $R_{rel}$ . This is statistically equivalent to the likelihood that a particle which was allowed to continue its trajectory from the last point on the killing circle, would re-enter the release circle at the newly chosen point. This concept is illustrated in Fig.23.



23. Particles begin their trajectories from a randomly chosen point at a distance  $r_{max} + N_{rel}$  from the initial seed site. If a particle moves beyond  $R_{max}$  it is terminated and a new particle introduced.

The time wasted waiting for distant particles to return to the region of interest can be further reduced by allowing particles to take larger steps at greater distances from the aggregate [63]. The distance  $d$  of the particle from the maximum growth point of the aggregate at  $r_{\max}$  is calculated at each step. The size of the next step that it can take must be smaller than  $d$  to ensure that it does not land on a site which is already occupied.

### 2.1.2 Applied Voltage

As we have seen in Sec.1.4, and notably in Fig.11, applied voltage has a marked effect on the morphology of fractal electrodeposits. In terms of the DLA model, this has both long and short range effects.

A voltage  $V$  generates an electric field  $\mathbf{E}$  ( $\text{Vm}^{-1}$ )

$$\mathbf{E} = -\nabla V \quad (2.47)$$

at a distance from the electrode. Mass transport effects due to migration are proportional to  $\mathbf{E}$  from Eq.1.18, and so migration effects due to applied voltage fall off as one over the distance from the electrodeposit. (The perimeter of the deposit is an equipotential surface.) Thus the effect of applied voltage on the bulk of the electrolyte is small compared to that around the surface. Ideally at every step of the particle's motion, we would calculate its distance to the nearest point of growth of the deposit, and move the particle preferentially in that direction. This, however, is computationally very expensive far from the deposit, especially given that the effect is small in the bulk. Far from the deposit, therefore, we simulate the effect of applied voltage simply as a general drift of the particles towards the

centre of the deposit (generally also the centre of the lattice). This central drift is very much smaller than the local drift towards the deposit surface.

This numerical approach is similar to that of Erlebacher et al [72] who consider the cation transport to be diffusion controlled far from the deposit and migration controlled close to the aggregate. Their model is based on the proposal by Chazalviel et al [73][74] that a space charge region exists close to the surface of the deposit, within which there exists a high electric field and large concentration gradient. (Additional consideration of the effects of local interactions between anions and cations within the solution requires solving the Poisson equation at each point. Such a study is currently being conducted by Fleury and co-workers.)

At every step in our simulation, the angle  $\theta_{cen}$  between the  $y$ -direction ('up') and the line from the particle to the centre of the lattice is calculated using the convention shown in Fig.24. The probabilities for the movement in each of the four possible directions at the next step are then adjusted in geometric proportion to increase the likelihood that the particle will move towards centre. The probabilities of moving up, down, left and right respectively become

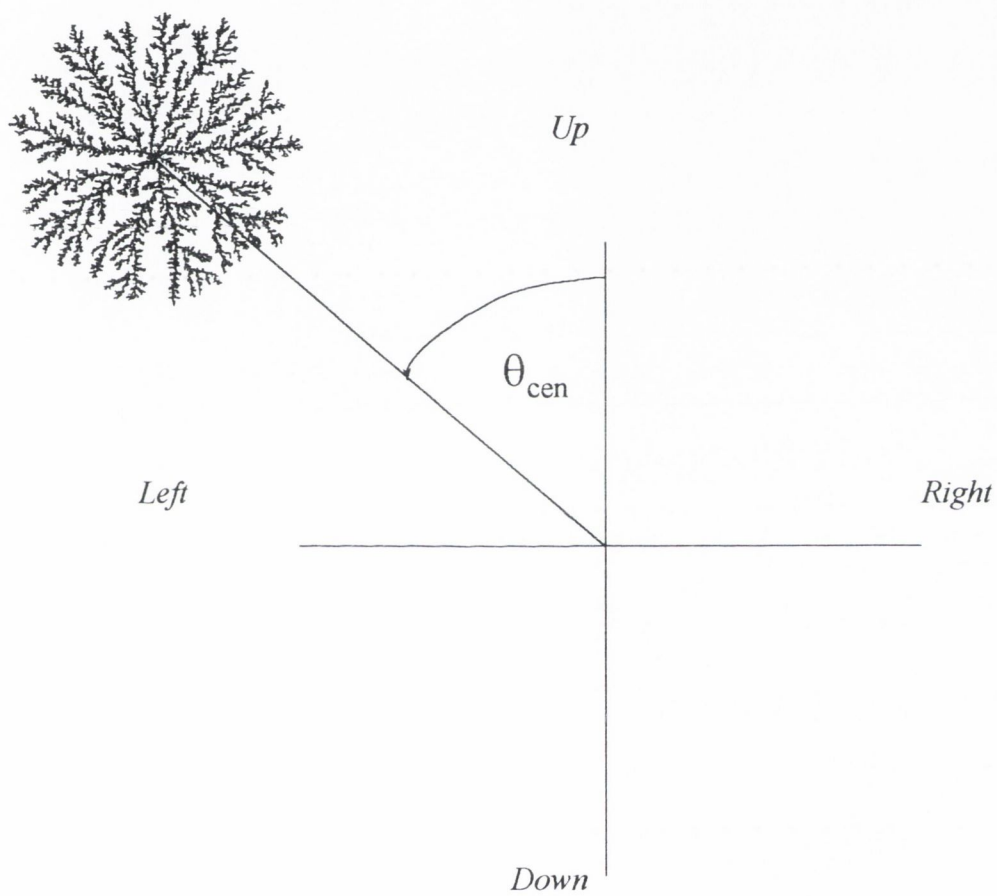
$$Up \quad : \quad \frac{1}{4} + V_{cen} \cos \theta_{cen} \quad (2.48a)$$

$$Down \quad : \quad \frac{1}{4} - V_{cen} \cos \theta_{cen} \quad (2.48b)$$

$$Left \quad : \quad \frac{1}{4} + V_{cen} \sin \theta_{cen} \quad (2.48c)$$

$$Right \quad : \quad \frac{1}{4} - V_{cen} \sin \theta_{cen} \quad (2.48d)$$

where the value of  $V_{cen}$  can be adapted to reflect the extent of this effect.



24. At each step, the angle  $\theta_{cen}$  (counterclockwise from the y-axis) between the particle and the central initial seed site is calculated.



The effect of the applied voltage is most significant in the immediate vicinity of the deposit where its inverse distance character must be taken into consideration. Once the particle is within a distance  $R_{look}$  of the maximum radius of growth of the deposit, we must check whether or not the particle is close to a branch of the deposit. We therefore define a look-up table over sites within a distance  $R_{look}$  of the particle as shown in Fig.25 ( $R_{look} \sim 8$  lattice spacings.) Sites within this area are grouped together into sets of equal distance from the particle. Starting from the inside and working outwards, each set is checked until an occupied site is detected. Once an occupied site is detected, the searching stops. If no site within the range is occupied, the voltage model of Eq.2.48 is used. The drift towards centre is, however, always very much less significant than the local drift to the deposit surface.

The distance  $d_{deposit}$  from the ion to the occupied site is found from the look-up table, as is the angle  $\theta_{dep}$  defined in Fig.25(a).  $\theta_{dep}$  is the angle from the  $y$ -axis to the line joining the particle to the nearest occupied site on the deposit. The probabilities of the particle moving up, down, left and right at the next move respectively become

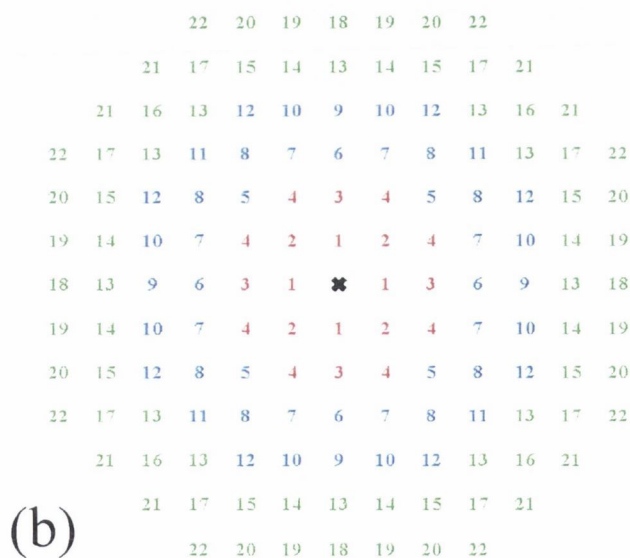
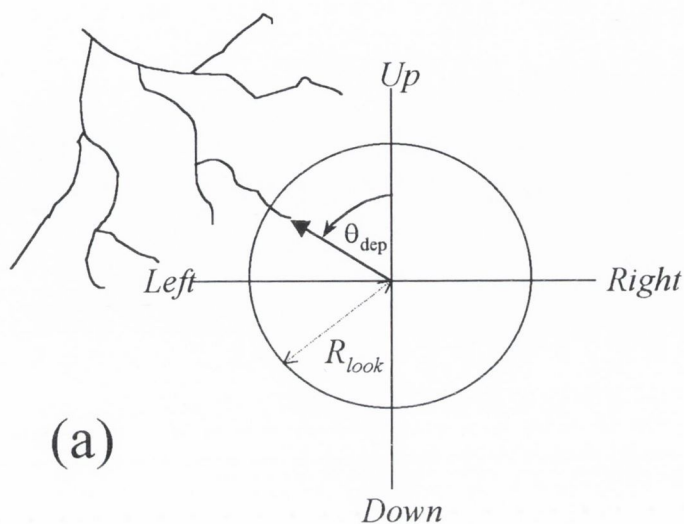
$$Up \quad : \quad \frac{1}{4} + V_{mig}(d_{deposit}) \cos \theta_{dep} \quad (2.49a)$$

$$Down \quad : \quad \frac{1}{4} - V_{mig}(d_{deposit}) \cos \theta_{dep} \quad (2.49b)$$

$$Left \quad : \quad \frac{1}{4} + V_{mig}(d_{deposit}) \sin \theta_{dep} \quad (2.49c)$$

$$Right \quad : \quad \frac{1}{4} - V_{mig}(d_{deposit}) \sin \theta_{dep} \quad (2.49d)$$

where the factor  $V_{mig}$  which determines the extent of the effect is inversely proportional to the distance  $d_{deposit}$  to the nearest point on the deposit.  $V_{mig}(d_{deposit}) \equiv C/d_{deposit}$ , where  $C$  is a constant which can be varied in the program. Eq.2.49 thus increases the probability



25.(a) Sites within an area  $R_{look}$  of the particle are checked for occupied sites. The angle  $\theta_{mig}$  to the nearest occupied site is then calculated. (b) Sites are grouped together into sets of equal distance from the particle. Starting from the inside and working outwards, each set is checked until an occupied site is detected. Like numbers indicate sites within the same set.

that the particle will move in a direction normal to the surface at the nearest occupied site. In the case that more than one “nearest occupied site” is detected (with the same value of  $d_{deposit}$ ), then the adjustments in Eq.2.49 are made for the respective  $\theta_{dep}$  values of each site.

### 2.1.3 Reaction Kinetics

The electrodeposits considered here are generally taken to be grown in a mass transport limited regime (Sec.1.5.4). That is to say that the reaction kinetics are fast compared to the rate of diffusion of ions from the bulk solution to the electrode. It is useful, however, to be able to incorporate the effect of reaction kinetics into the simulation. As we saw in Eq.1.10, the charge transfer rate constants are strongly dependent on the applied voltage. So depending on the value of  $V$  and  $k_0$ , an ion may not react immediately on arriving at the electrode. That is, it may continue to move along, or even away from the electrode before it is reduced.

Numerically, this is equivalent to saying that a particle may not stick immediately on moving to a site with an occupied neighbour. Up to this point it was assumed that the probability  $p$  of sticking to the deposit was  $p = 1$ . Now, however, a *variable sticking probability*  $0 < p \leq 1$  is introduced, so that on arrival at the deposit, a particle may or may not stick. If it does not stick, it continues to move according to the combination of probabilities defined in Eqs.2.48 and 2.49. If at this move, it attempts to move *onto* the occupied neighbour, then it sticks in its original position. A magnetic field effect on

electrode kinetics is not considered here for, although the question of such an effect remains somewhat controversial [64], it is generally determined to be insignificant [65][66][38].

#### 2.1.4 Concentration

The model so far considers the behaviour of only one particle at a time. The trajectory of one particle is followed until it sticks, and then a new particle is introduced. This, of course, is very far from the case in reality; one ion does not wait for another. In real electrolytes there is a finite, and often quite high, concentration of metallic ions surrounding the electrode. Many ions may simultaneously react all over the surface. As the electrode-posit grows, so does its perimeter, and so the number of ions moving close to the electrode and being reduced at a given time is constantly increasing.

In light of this the model has been adapted to allow multiple particles to move and stick simultaneously. The solution concentration is defined by saying that some fraction  $f_c$  of the sites within the release band are occupied. The release band is defined as the area between  $\pi r_{\max}^2$  and  $\pi(r_{\max} + N_{rel})^2$ . It is essentially a two dimensional equivalent of the release circle of Eq.2.46. We thus define some number  $n_{movers}$  of particles

$$n_{movers} = f_c \frac{[\pi(r_{\max} + N_{rel})^2 - \pi r_{\max}^2]}{\text{Area of one lattice square}} \quad (2.50)$$

to be assigned sites within the band at start-up.

At each step thereafter, each particle can move according to the probabilities defined in the preceding sections. If a particle attempts to move onto a site that is already occupied by another moving particle, then it stays put. When one particle sticks (or moves beyond  $R_{\max}$ ), a new particle is randomly introduced within the release band. If the site proposed

for the new particle is already occupied, then these co-ordinates are rejected and another site must be chosen. At high concentrations, this may result in the need for several attempts before a vacant site is found for the new particle. Similarly, if a particle attempts to move to a site that is already occupied by another, unattached, particle, then the former simply moves back to its original position until the next iteration.

A consequence of this algorithm is the fact that the number of particles moving at a given time is constantly increasing as the deposit grows, scaling as

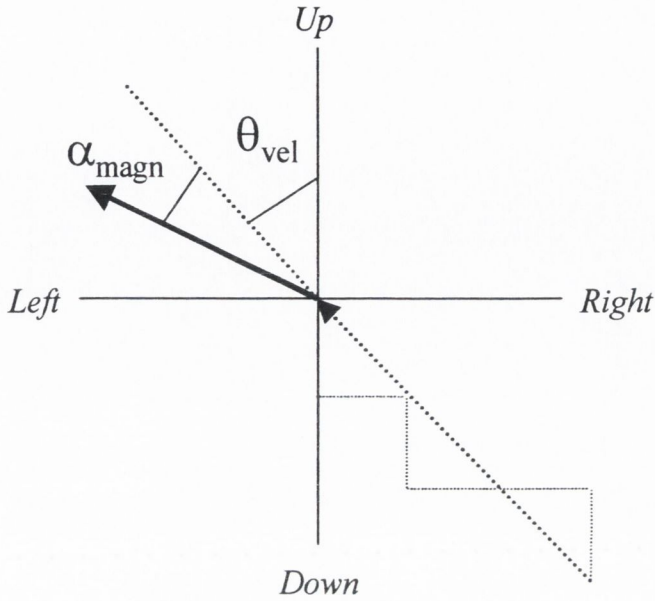
$$n_{movers} \propto 2\pi N_{rel} r_{max}. \quad (2.51)$$

### 2.1.5 Applied Magnetic Field

Two models were used to attempt to introduce the effect of an applied magnetic field. As we are dealing with a two dimensional system, we are restricted to considering the effect of a magnetic field applied perpendicular to the plane of growth of the deposit, so that the Lorentz  $\mathbf{j} \times \mathbf{B}$  force is exerted in the plane in which we are carrying out our calculations.

#### Effect on Individual Particles

The first approach considers the effect of the magnetic field on a particle moving with some velocity  $\mathbf{v}$ , as adopted by Mizuseki et al [76][77]. The ‘velocity’ of the particle is determined by, at each step, examining its motion over the previous  $N$  steps. In these simulations  $N = 4$  or  $6$ . The average angle  $\theta_{vel}$  through which it has moved over  $N$  steps is calculated relative to the ‘up’-direction as shown in Fig.26. In the absence of an applied magnetic field, the particle will tend to continue along this trajectory as a result of the other



26. The angle  $\theta_{vel}$  through which the particle has moved over the previous  $N$  steps is calculated relative to the 'up'-direction. An applied magnetic field will tend to make it deviate from this course by a further angle  $\alpha_{magn}$ . Here  $\alpha_{magn}$  has a positive value, indicating that the magnetic field is applied *downwards*.

forces acting in the system. Under the Lorentz force of an applied magnetic field, however, the particle is deflected through some angle  $\alpha_{magn}$  from  $\theta_{vel}$  as shown in the figure.  $\alpha_{magn}$  may have a positive or a negative value depending on the direction of the applied field.

Thus an additional term is added to the probabilities for the particle to move respectively up, down, left or right at the next step,

$$Up \quad : \quad \frac{1}{4} + B_{vel} \cos(\theta_{vel} + \alpha_{magn}) \quad (2.52a)$$

$$Down \quad : \quad \frac{1}{4} - B_{vel} \cos(\theta_{vel} + \alpha_{magn}) \quad (2.52b)$$

$$Left : \frac{1}{4} + B_{vel} \sin(\theta_{vel} + \alpha_{magn}) \quad (2.52c)$$

$$Right : \frac{1}{4} - B_{vel} \sin(\theta_{vel} + \alpha_{magn}) \quad (2.52d)$$

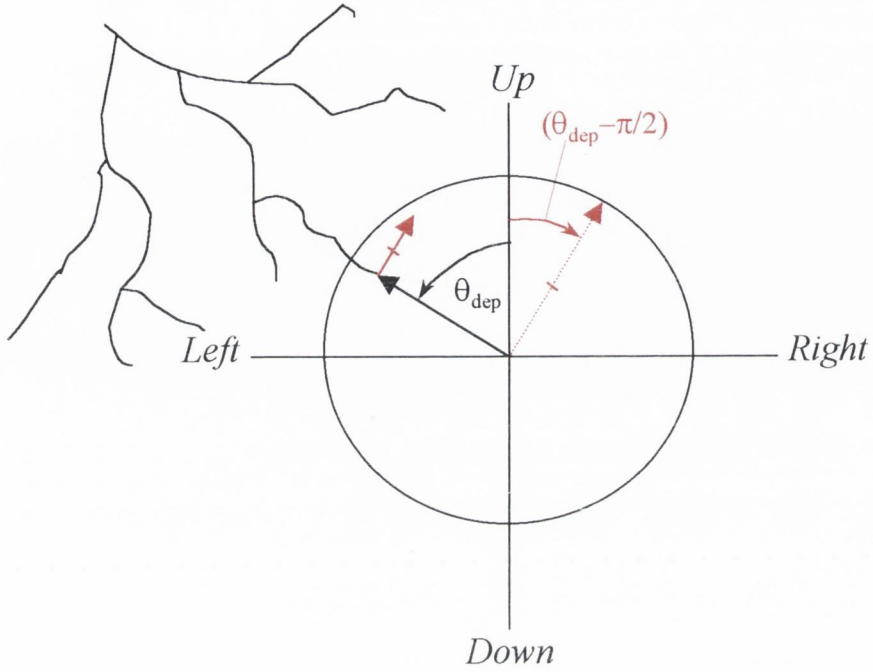
where the constants  $B_{vel}$  and  $\alpha_{magn}$  each reflect the magnetic field strength.

### Bulk Flow

The problem with this approach, however, is that it considers the motion of each particle individually, without acknowledging the fact that the magnetic field acting on the current density  $\mathbf{j}$ , induces a forced convective flow in the bulk solution according to the magnetic field term included in the Navier-Stokes equation (Eq.1.37).

An alternative approach to modelling the magnetic field to some extent incorporates this understanding. If we recognise that the magnetic field induces bulk flow of the fluid, then we must also recognise that this fluid must flow over and around the complex surface of the fractal. That is we must consider a flow parallel to the surface of the deposit. This approach is further justified by considering that, close to the electrode,  $\mathbf{j}$  is perpendicular to the fractal surface (from Eqs.2.49), so the Lorentz force  $\mathbf{j} \times \mathbf{B}$  will be in a direction parallel to the fractal surface.

This model can also be interpreted as incorporating the theory that the application of a magnetic field results in an electrokinetic effect at the electrode, which drags parallel to the surface. In any case, we recognise when the particle is in the vicinity of the electrode by again searching within a radius  $R_{look}$  for an occupied site as in Fig.27. So if  $\theta_{dep}$  is the angle from the particle to the nearest point on the deposit, measured anticlockwise from



27. The nearest occupied site is found by again scanning over an area of radius  $R_{look}$  about the particle. Flow due to the magnetic field is parallel to the plate, i.e. at an angle  $(\theta_{dep} \pm \pi/2)$  depending on the field direction. Here the angle is  $(\theta_{dep} - \pi/2)$ , to model a magnetic field applied vertically upwards.

the ‘up’-direction, the flow parallel to the surface will be through an angle  $(\theta_{dep} \pm \pi/2)$  depending on the direction of the magnetic field.

The probabilities for motion at the next step are thus adapted<sup>5</sup> to include terms

$$Up \quad : \quad \frac{1}{4} + B_{flow} \cos(\theta_{dep} \pm \pi/2) \quad (2.53a)$$

$$Down \quad : \quad \frac{1}{4} - B_{flow} \cos(\theta_{dep} \pm \pi/2) \quad (2.53b)$$

$$Left \quad : \quad \frac{1}{4} + B_{flow} \sin(\theta_{dep} \pm \pi/2) \quad (2.53c)$$

<sup>5</sup> Note that in the process of modifying the probabilities, it is possible that the final probability  $P_i$  of moving in a given direction  $i$  may be less than zero or greater than one. In the case that  $P_i < 0$ , then we set that  $P_i = 0$ , and renormalise the sum of the remaining probabilities to 1.



$$Right \quad : \quad \frac{1}{4} - B_{flow} \sin(\theta_{dep} \pm \pi/2) \quad (2.53d)$$

### 2.1.6 The Lattice

In this study the lattice used is in all cases a square lattice. Alternatively a body-centred, hexagonal, or random lattice could have been used. It has been shown that for very large scale simulations [3], the underlying lattice can begin to affect the self-similarity of the growing fractal, as it begins to assume some semblance of the lattice structure. In this case, however, the scale of our simulations is not sufficiently large for this to be a serious concern. Furthermore, great care has been taken, for example with the formulation of the look-up table in Fig.25, to overcome any tendency towards a square structure. If this is not done carefully, then movement towards the deposit can yield misleading results; for example, the attempt by Mizuseki et al [77] to introduce a drift towards the surface resulted in growth predominantly along the  $x$  and  $y$ -axes.

## 2.2 Vertical Circular Electrode Geometry

The thickness of the cell is  $\sim 0.2$  mm. Although gravitational convection within the diffusion layer can be significant in the horizontal cell even within this small thickness [68], we do not consider this effect in the present two-dimensional study.

When the cell is held vertically, however, gravity acts along the length of the cell and may be modelled in two dimensions. As seen from Fig.15 in the absence of an applied magnetic field, the resultant vertical, columnar growth is radically different from the zero

field radial morphologies of the horizontal case. We must thus introduce natural convective effects due to gravity into the model in order to consider growth in a vertical cell.

### 2.2.1 Gravity

As we know from Sec.1.5.5, the perimeter of the deposit is surrounded by a diffusion layer across which the concentration of metal ions varies roughly linearly. As ion rich material has a somewhat higher density ( $\sim 1050 \text{ kgm}^{-3}$ ) than ion depleted solution ( $\sim 1000 \text{ kgm}^{-3}$ ), this also results in a density gradient in the same region. Thus around the perimeter, three separate regions may be identified [78]:

1. On the lower side of a branch of the deposit, the dense solution lies below the less dense solution, and thus no natural convection takes place.
2. On the upper side of a branch of the deposit, the dense solution lies above the less dense solution. Gravity thus acts to pull the dense material downwards, which sets up convective swirls above the surface. As a result, ions that are above the surface of the deposit, arrive more quickly at the electrode surface [79] [80].
3. The side of a branch of the deposit is equivalent to a density gradient at a vertical wall. In this case as the dense material tumbles downwards under gravity, the less dense material at the wall rises upwards. Convection cells are thus established which push ions upwards along the surface of the deposit [68].

Again we turn to the look-up table defined within an area of radius  $R_{look}$  from the particle. If an occupied site is detected we can, from the angle  $\theta_{dep}$  (Fig.25) determine whether the ion is above, below or to the side of the surface.

In the case of 2, we define a particle as being ‘above’ the surface if  $\theta_{dep}$  lies within the range

$$(\pi - \gamma_{above}) \leq \theta_{dep} \leq (\pi + \gamma_{above}) \quad (2.54)$$

as in Fig.28(a) where  $\gamma_{above}$  is a small angle  $\sim 5^\circ$ . If  $\theta_{dep}$  satisfies the condition of Eq.2.54, then the probability that the particle will move downwards at the next step is increased, and the probability of upwards movement is correspondingly reduced. The likelihood of movement to the left or right is unaltered.

$$Up \quad : \quad \frac{1}{4} - G_{above} \quad (2.55a)$$

$$Down \quad : \quad \frac{1}{4} + G_{above} \quad (2.55b)$$

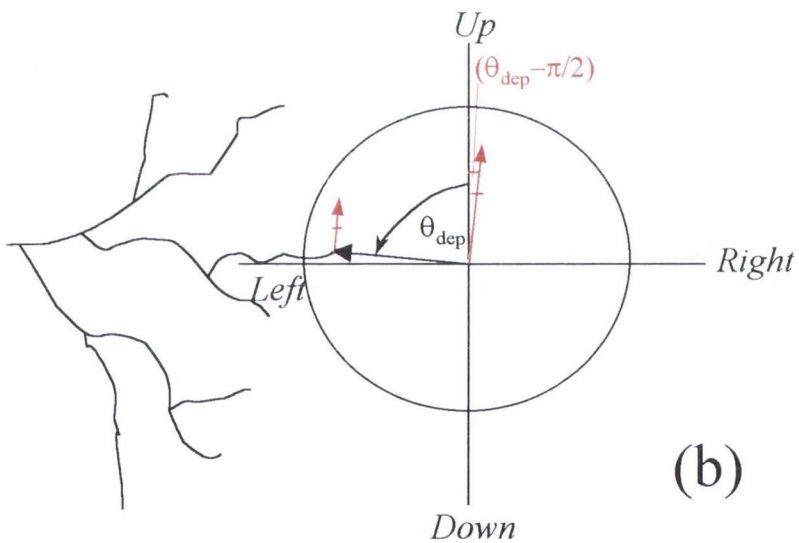
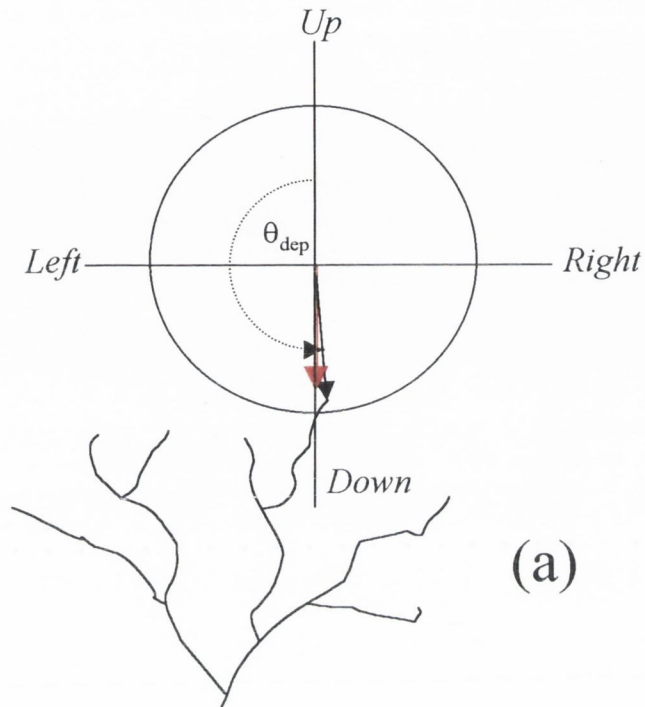
Similarly it is determined that a particle is lying to the side of a branch of the deposit if the angle  $\theta_{dep}$  lies within the range

$$(\pi/2 - \gamma_{side}) \leq \theta_{dep} \leq (\pi/2 + \gamma_{side}) \quad (2.56a)$$

$$(3\pi/2 - \gamma_{side}) \leq \theta_{dep} \leq (3\pi/2 + \gamma_{side}) \quad (2.56b)$$

according to Fig.28(b). In this case the flow will not simply be vertically upwards, but will be constrained by the solid interface to move upwards parallel to the surface of the deposit. That is to say that if Eq.2.56(a) is satisfied, then the probabilities are adjusted according to

$$Up \quad : \quad \frac{1}{4} + G_{side} \cos(\theta_{dep} - \pi/2) \quad (2.57a)$$



28.(a) If the particle is within a defined angular radius above the deposit, then it tends to drift downwards; (b) if the particle lies to the side of the deposit then it tends to move upwards parallel to the surface of the deposit.

$$Down \quad : \quad \frac{1}{4} - G_{side} \cos(\theta_{dep} - \pi/2) \quad (2.57b)$$

$$Left \quad : \quad \frac{1}{4} + G_{side} \sin(\theta_{dep} - \pi/2) \quad (2.57c)$$

$$Right \quad : \quad \frac{1}{4} - G_{side} \sin(\theta_{dep} - \pi/2) \quad (2.57d)$$

while if Eq.2.56(b) is satisfied, the probabilities vary by

$$Up \quad : \quad \frac{1}{4} + G_{side} \cos(\theta_{dep} + \pi/2) \quad (2.58a)$$

$$Down \quad : \quad \frac{1}{4} - G_{side} \cos(\theta_{dep} + \pi/2) \quad (2.58b)$$

$$Left \quad : \quad \frac{1}{4} + G_{side} \sin(\theta_{dep} + \pi/2) \quad (2.58c)$$

$$Right \quad : \quad \frac{1}{4} - G_{side} \sin(\theta_{dep} + \pi/2). \quad (2.58d)$$

$G_{above}$  and  $G_{side}$  are constants representing the strength of natural convection flows.

## 2.3 Linear Electrode Geometry

In the case of deposition between *linear* electrodes, most of the above arguments still apply, but with a few minor changes.

A circular simulation begins with one central occupied seed site. Now, however, we initially occupy one full row of sites to represent the surface of the linear cathode. The cathode is taken to be in the ‘downwards’ direction. The boundary conditions must also be altered somewhat. In the circular case a particle was deemed to have ‘left’ the system if it moved beyond some maximum radius  $R_{max}$ . Now, however, care must be taken to remove particles that walk past the open ends of the cell.

Eqs.2.49 and 2.53 still apply for behaviour in the vicinity of the surface of the deposit, as does Eq.2.52 for the magnetic field effect on an individual ion with velocity  $v$ . In approximating the effect of voltage at some distance from the surface, however, the drift is no longer towards centre, but downwards towards the cathode. Thus for the linear geometry, Eq.2.48 is replaced by

$$Up \quad : \quad \frac{1}{4} - V_{linear} \quad (2.59a)$$

$$Down \quad : \quad \frac{1}{4} + V_{linear} \quad (2.59b)$$

where the constant  $V_{linear}$  represents the strength of the applied voltage.

# Chapter 3

## Effects of the DLA Adaptations

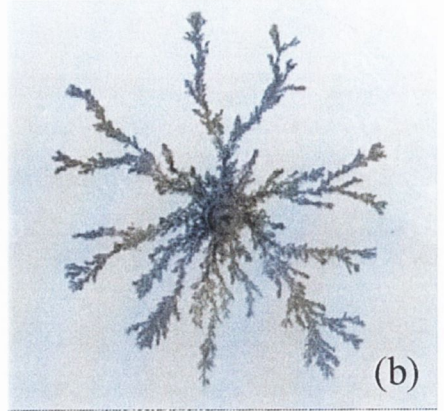
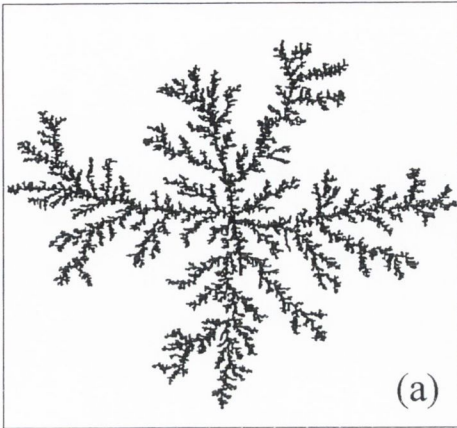
The basic DLA model produces diffuse, fern-like patterns of the kind shown in Fig.29 (a), which bears a strong similarity to the results of electrodeposition experiments under condition of low concentration and low applied voltage of the kind shown in Fig.29 (b).

In this section we will consider the effects of external influences such as applied voltage, ionic concentration, applied magnetic field and gravity which are introduced as detailed in Chapter 2.

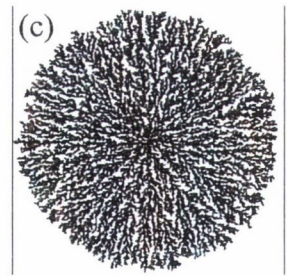
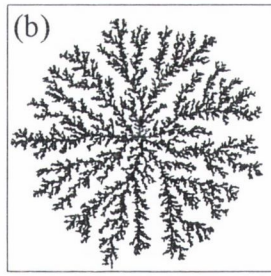
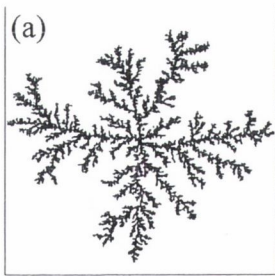
### 3.1 Circular Electrodes

#### 3.1.1 Applied Voltage

In the absence of an applied magnetic field, the key parameters determining the morphology of a deposit are the concentration of ions in the solution, and the applied voltage. Firstly, while maintaining a very low concentration, we examine the effects of varying the parameters relating to applied voltage. In the first approximation that the growth of the deposit is broadly radial, the applied voltage can be modelled according to Eq.2.48, whereby the probability is increased that the ions will drift towards the centre of the deposit. The extent of this effect can be varied by increasing the constant  $V_{cen}$ . Results for varying values of  $V_{cen}$  are shown in Fig.30.



29.(a) A typical structure generated by the basic DLA model, compared with (b) a typical DLA-type electrodeposit.



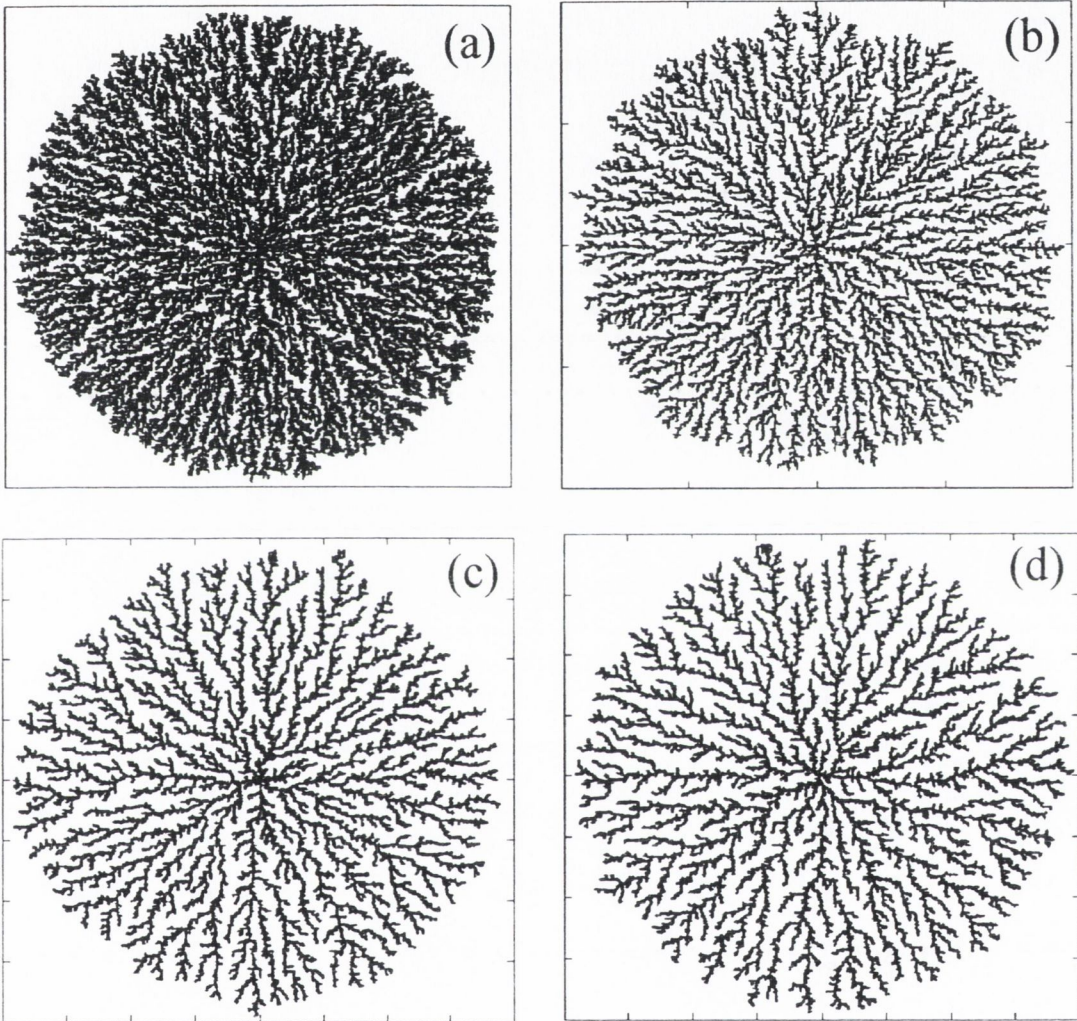
30.Results of increasing the imposed drift towards the centre of the deposit for (a) Plain DLA, (b)  $V_{cen} = 0.005$  and (c)  $V_{cen} = 0.05$ .



Clearly the imposition of this central drift results in deposits which are more dense and more radial. This change in the morphology of the structures can also be monitored through their fractal dimensions which are (a)  $D_f = 1.67$ , (b)  $D_f = 1.79$  and (c)  $D_f = 1.87$ .

We must recognise, however, that this broad drift towards centre is only valid at a distance from the structure. Close to the deposit, the electric field lines emerge perpendicular to the deposit surface. And thus the ions are preferentially drawn in towards the surface according to Eq.2.49. Remembering that in a 2-dimensional system, the electric field will vary as  $1/d_{deposit}$ , we search sites within a distance  $R_{look}$  of the deposit for occupancy as detailed in Sec.2.1.2. Thus at a distance from the structure, voltage is still modelled by a drift towards centre in the style of Eq.2.48, but once an occupied site is detected within a distance  $R_{look}$  of the ion, Eqs.2.48 are abandoned, and Eqs.2.49 are implemented instead. Results vary somewhat with the range of  $R_{look}$  as shown in Fig.31.

As the value of  $R_{look}$  is increased from 4 to 10 lattice spacings, the resultant fractals become less dense, with more clearly defined branches, and a slightly lower fractal dimension. We describe this as a *ramified* structure. Fig.31(a) (also Fig.30(c)) which uses *only* the central drift model, and has  $D_f = 1.87$ , is shown for comparison. Once we begin to consider the effect close to the deposit however,  $R_{look} = 4$  spacings produces a deposit with  $D_f = 1.85$ ,  $R_{look} = 6$  spacings results in  $D_f = 1.84$ , while both  $R_{look} = 8$  and  $R_{look} = 10$  spacings yield deposits with  $D_f = 1.81$ . As there was no apparent difference between the results for 8 and 10 spacings, we conclude that, due to the fact that  $V_{mig} = V_{mig}(1/d_{deposit})$ , the bulk of the effect is contained within a distance smaller than 10 lattice spacings from the deposit. Thus for the remainder of the simulations, we take  $R_{look} = 10$ .



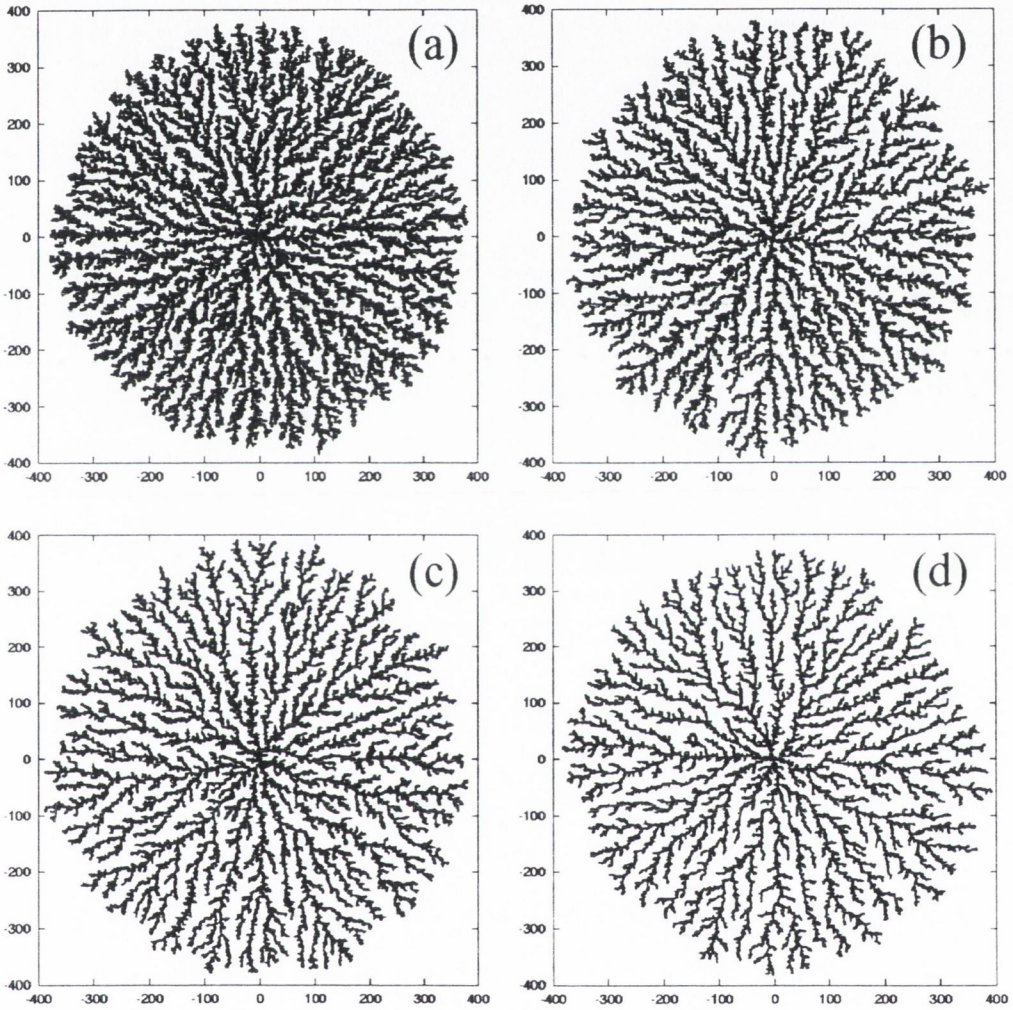
31. The applied voltage is modelled as a drift perpendicular to the deposit surface with a  $1/d_{deposit}$  dependency. The result depends on the distance  $R_{look}$  over which we scan for occupancy. (a)  $D_f = 1.87$  as in Fig.30(c) i.e. without the implementation of Eq.2.48, (b)  $R_{look} = 6$  sites,  $D_f = 1.84$ , (c)  $R_{look} = 8$  sites,  $D_f = 1.81$  and (d)  $R_{look} = 10$  sites,  $D_f = 1.81$ . (In each case  $C = 1.0$ , where  $V_{mig} = C/d_{deposit}$ .)

Having determined an appropriate value for  $R_{look}$ , Fig.32 demonstrates the effect of variations in the value of  $C$ , where  $V_{mig}(1/d_{deposit}) = C/d_{deposit}$ . The deposits become more ramified as the value of  $C$  is increased.

### 3.1.2 Concentration

Experimentally, large variations in the concentration of ions in the solution can have dramatic effects on fractal morphologies. As illustrated in Fig.11, in the very high voltage, high concentration regime morphologies change from radial to dendritic in character. Numerically we introduce a finite concentration by increasing the number of particles walking in the system in proportion to the maximum radius of the growing deposit. The number of particles moving is some fraction of the number of sites available within an annulus of thickness  $R_{rel}$  about the deposit. A constant concentration is thus maintained as the fractal develops. On an  $800 \times 800$  lattice, with ions initially placed randomly at 20% of the sites about the central seed (in practice this is the maximum percentage of sites which can be filled, as the particles are unable to move at greater concentrations), there might typically be as many as  $\sim 4000$  ions moving around the lattice by the end of the simulation.

Consider, by comparison, the fraction of water molecules in the solution which are associated with the ionic hydration spheres. A electrolyte might typically contain a metal ion concentration  $\sim 500 \text{ mol/m}^3$ , i.e. a 0.5 molar solution. A 1 molar solution consists of one mole of the substance per litre of water. One litre of water weighs 1000 g, and so contains  $1000/18 = 55$  moles of water. Taking an average, however, of six water molecules associated with the hydration sphere of a given ion, that means that 3 ( $= 0.5 \times 6$ ) of every



32. Given a value of  $R_{look} = 10$  lattice spacings, variations in the resultant deposits for (a)  $C = 0.1$ ,  $D_f = 1.85$ , (b)  $C = 0.3$ ,  $D_f = 1.83$ , (c)  $C = 0.5$ ,  $D_f = 1.82$  and (d)  $C = 1.0$ ,  $D_f = 1.81$  are shown, where  $V_{mig} = C/d_{deposit}$ .

55 moles are directly tied to the movement of the ions. That is  $\sim 6\%$  of the volume is ‘occupied’ by ions and their surrounding hydration spheres. Thus in our simulations, we can realistically hope to reproduce the kind of ionic concentrations observed experimentally.

The effect of increased concentration is summarised in Fig.33 for increasing values of  $f$ . The resultant deposits become somewhat more dense with raised fractal dimensions ranging from 1.80 to 1.83 as  $f$  increases from 0.005 to 0.2.

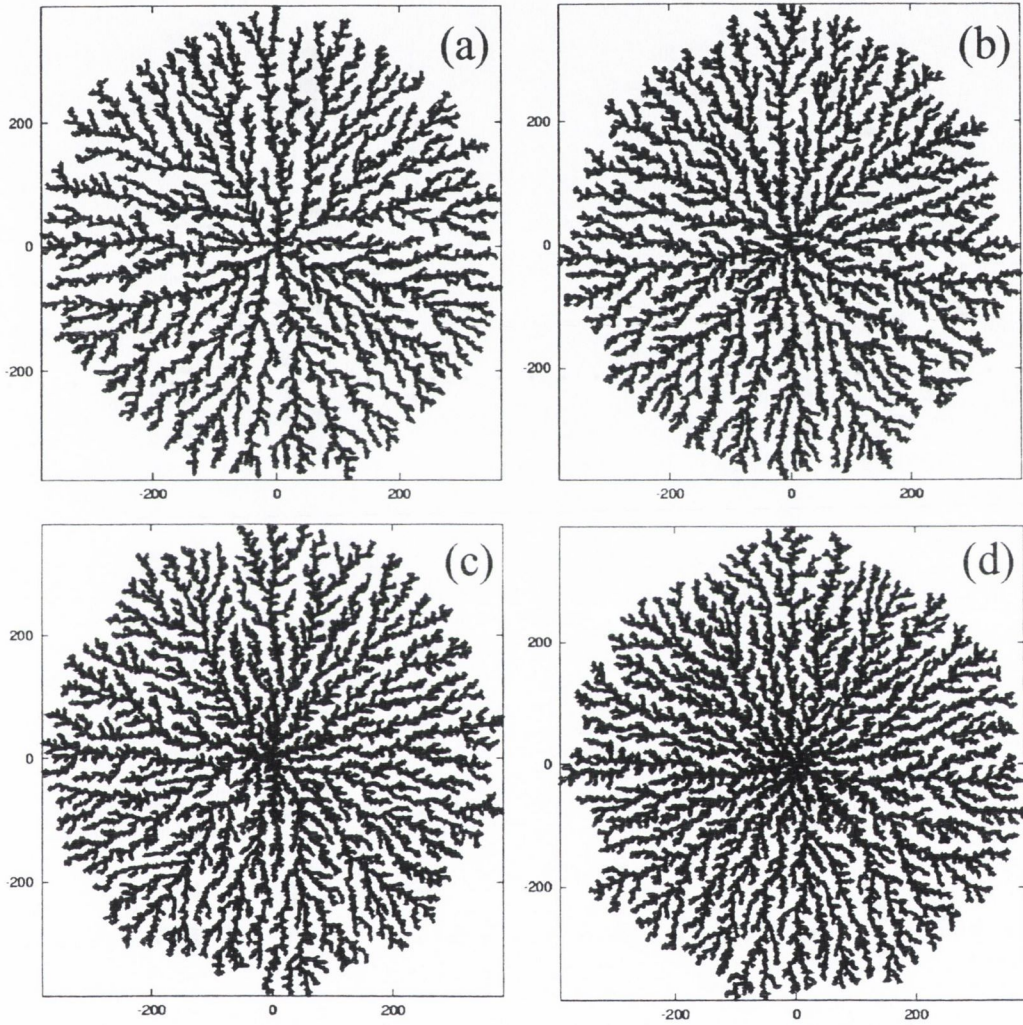
### 3.1.3 Magnetic Field

#### Individual Particle Approach

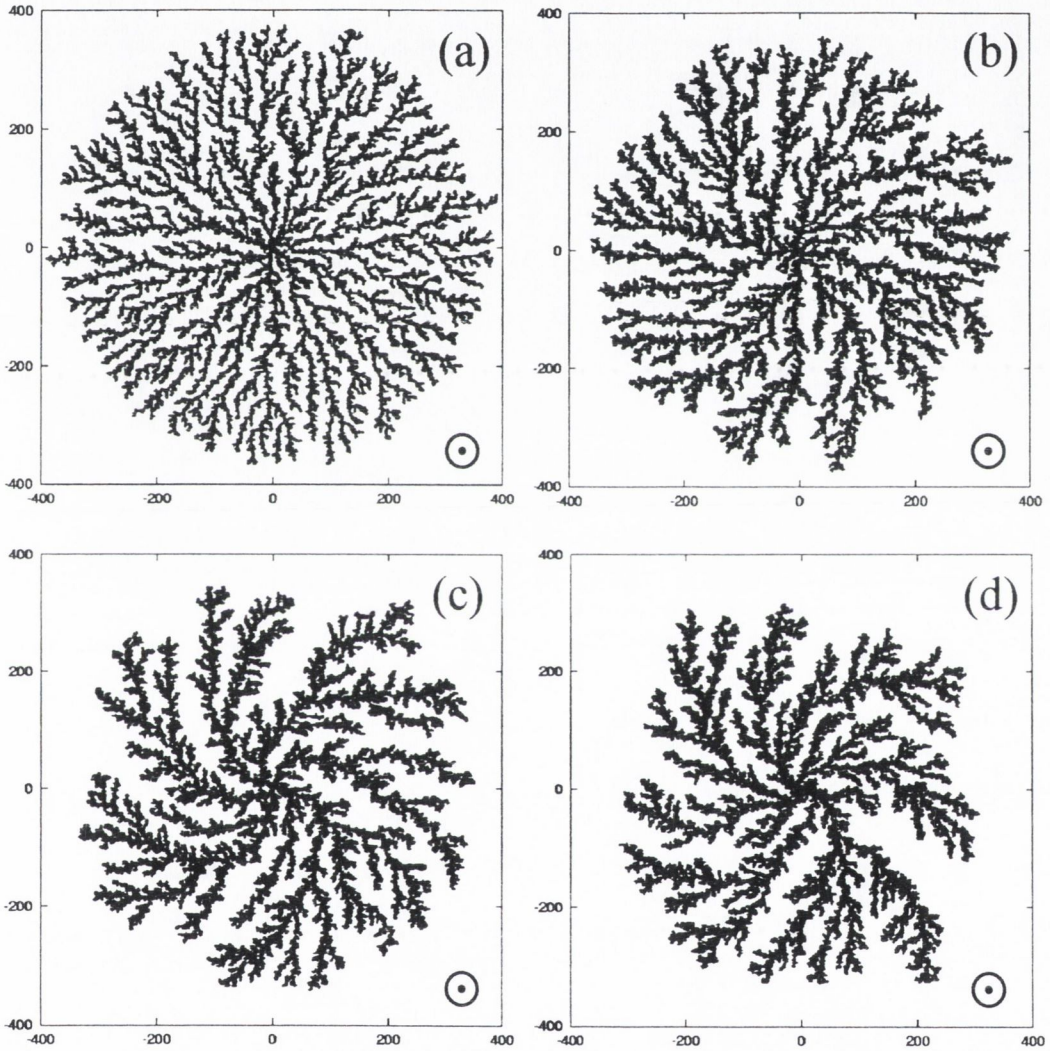
In Sec.2.1.5 two models were proposed to represent an applied magnetic field. The first considers the effect of a magnetic field on an individual ion which has moved through an angle  $\theta_{vel}$  over the previous  $N$  steps. The extent of this effect is monitored through two parameters; the angle  $\alpha_{magn}$  through which the particle is deflected relative to  $\theta_{vel}$ , and the multiplicative factor  $B_{vel}$ . Taking  $\alpha_{magn} = 20^\circ$ , the effects of varying  $B_{vel}$  are presented in Fig.35, while variations in  $\alpha_{magn}$  produce the fractals in Fig.34 where  $B_{vel} = 0.5$ .

In each case the resultant fractals are spiral outwards from the centre. The extent of the spiralling depends on the size of the magnetic field through  $\alpha_{magn}$  and  $B_{vel}$  as encountered experimentally. Individual branches become thicker and more clearly defined, as they drop in number. Fractal dimensions decrease as  $B_{vel}$  is increased, though no clear trend in the variation of  $D_f$  emerges as  $\alpha_{magn}$  is varied.

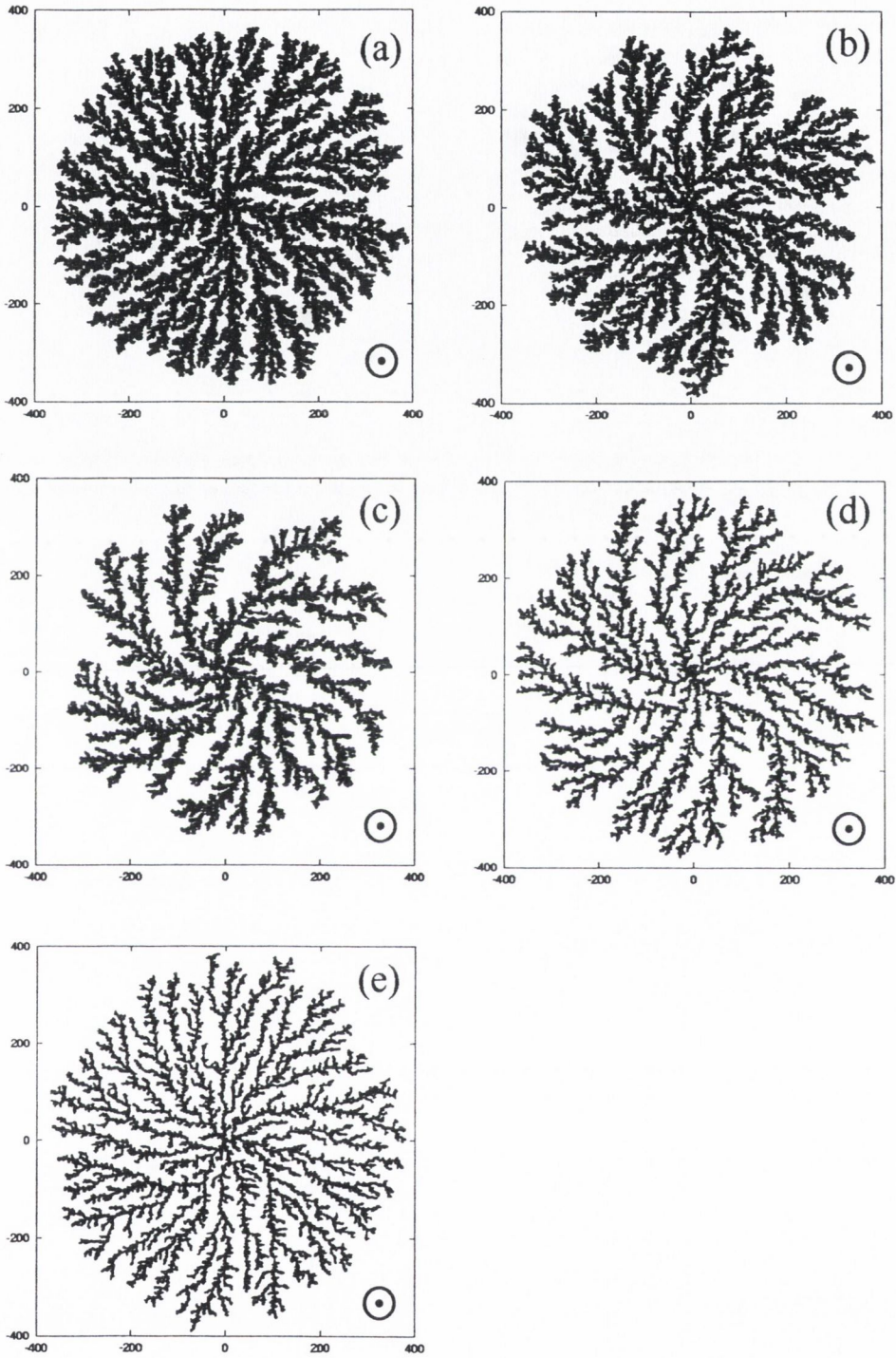
Importantly, the *chirality* of each of the spiral deposits reverses with a *reversal* in the direction of the applied magnetic field, as in Fig.37. Reversal of the magnetic field



33. Concentration is defined by the ratio  $f$  of the number of sites initially occupied within an annulus of depth  $R_{rel}$  about the central seed to the total number of sites in that area. (a)  $f = 0.005$ ,  $D_f = 1.80$ , (b)  $f = 0.1$ ,  $D_f = 1.81$ ,  $f = 0.15$ ,  $D_f = 1.83$  and (d)  $f = 0.2$ ,  $D_f = 1.83$ .



34. Numerical results for  $\alpha_{magn} = 20^\circ$ ,  $V_{cen} = 0.05$  and  $V_{mig} = 0.5$  with (a)  $B_{vel} = 0.1$ ,  $D_f = 1.81$ , (b)  $B_{vel} = 0.3$ ,  $D_f = 1.76$ , (c)  $B_{vel} = 0.5$ ,  $D_f = 1.70$  and (d)  $B_{vel} = 0.9$ ,  $D_f = 1.66$ .



35. Numerical results for  $B_{vel} = 0.5$ ,  $V_{cen} = 0.05$  and  $V_{mig} = 0.5$  with (a)  $\alpha_{magn} = 5^\circ$ ,  $D_f = 1.83$ , (b)  $\alpha_{magn} = 10^\circ$ ,  $D_f = 1.78$ , (c)  $\alpha_{magn} = 20^\circ$ ,  $D_f = 1.70$ , (d)  $\alpha_{magn} = 45^\circ$ ,  $D_f = 1.76$  and (e)  $\alpha_{magn} = 90^\circ$ ,  $D_f = 1.78$ .

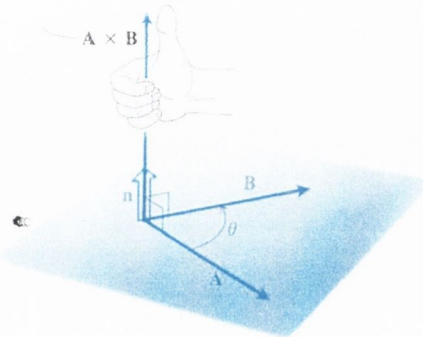


direction is represented by changing the sign of  $\alpha_{magn}$ . The sign of  $\alpha_{magn}$  for a given field orientation is determined using the right-hand rule. Fig.36 provides a reminder of this rule of ‘thumb’. A magnetic field applied *out of the plane* of the page is accordingly represented by a *negative* value of  $\alpha_{magn}$ , while a *positive* value of  $\alpha_{magn}$  indicates that the field is applied *into the plane* of the page.

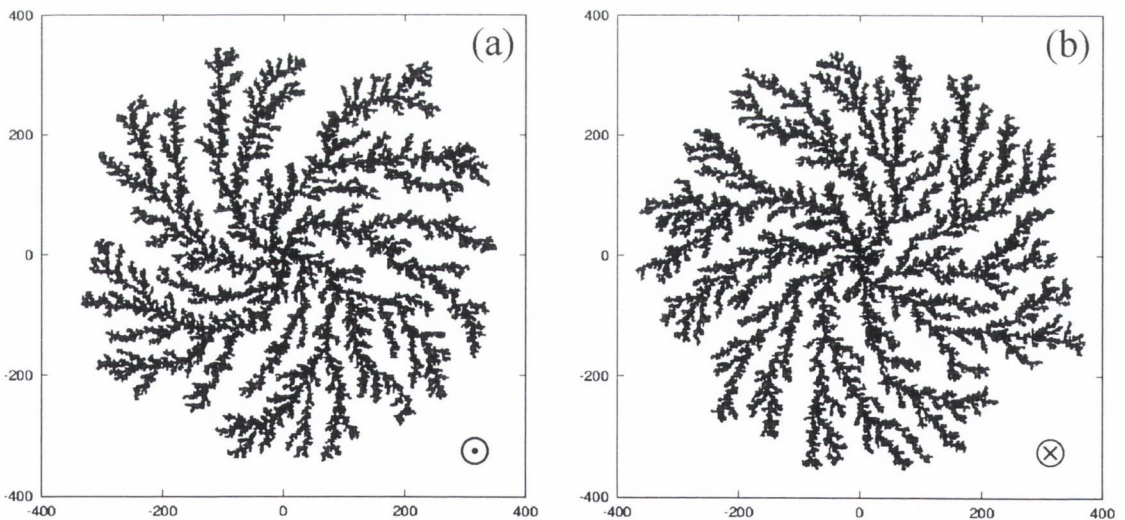
In light of the thumb rule, we re-examine the chirality of the fractals in Fig.37. While in general they have an overall structure which is similar to the experimental electrodeposits, they spiral in a direction *opposite* to that observed experimentally. Although results of this magnetic field model have been presented by Mizuseki et al [77], they did not refer to, or account for, this inconsistency with the direction of spiralling of the experimental result. It is interesting to notice, however that in Fig.35 the chirality of the deposit is less pronounced, and one might imagine that it is beginning to spiral in the opposite direction. Furthermore, this effect is not observed when the voltage is modelled simply as a drift towards centre. In order to tend towards the correct chirality, the model must first include the fact that the ions are moving towards the deposit surface. With this in mind, a new model for the magnetic field was introduced.

### **Bulk Flow Approach**

This second method considers the effect of the magnetic field induced bulk flow as it moves past the intricate fractal surface. Motion parallel to the deposit surface is indicated by increasing the probability that the particle will move through an angle  $(\theta_{dep} \pm \pi/2)$  where  $\theta_{dep}$  is the angle from the ion to the nearest point on the deposit. As above,  $(\theta_{dep} - \pi/2)$



36. Right Hand Thumb Rule : Curling the fingers of the right hand from  $\vec{A}$  through to  $\vec{B}$ , the direction in which the thumb now points indicates the direction of the cross-product vector  $\vec{A} \times \vec{B}$  (Thomas/Finney 1988).



37. The chirality of the numerical deposits reverses when the direction of the applied magnetic field is reversed. (a)  $\alpha_{magn} = -20^\circ$  for a magnetic field applied *out of the plane* while (b)  $\alpha_{magn} = 20^\circ$  for a field applied *into the plane*.

indicates that the magnetic field is applied out of the plane of the cell, and  $(\theta_{dep} + \pi/2)$  indicates that it is applied out of the plane. For the  $-\pi/2$  case, results for a number of values of the multiplicative constant  $B_{flow}$  are shown in Fig.38.

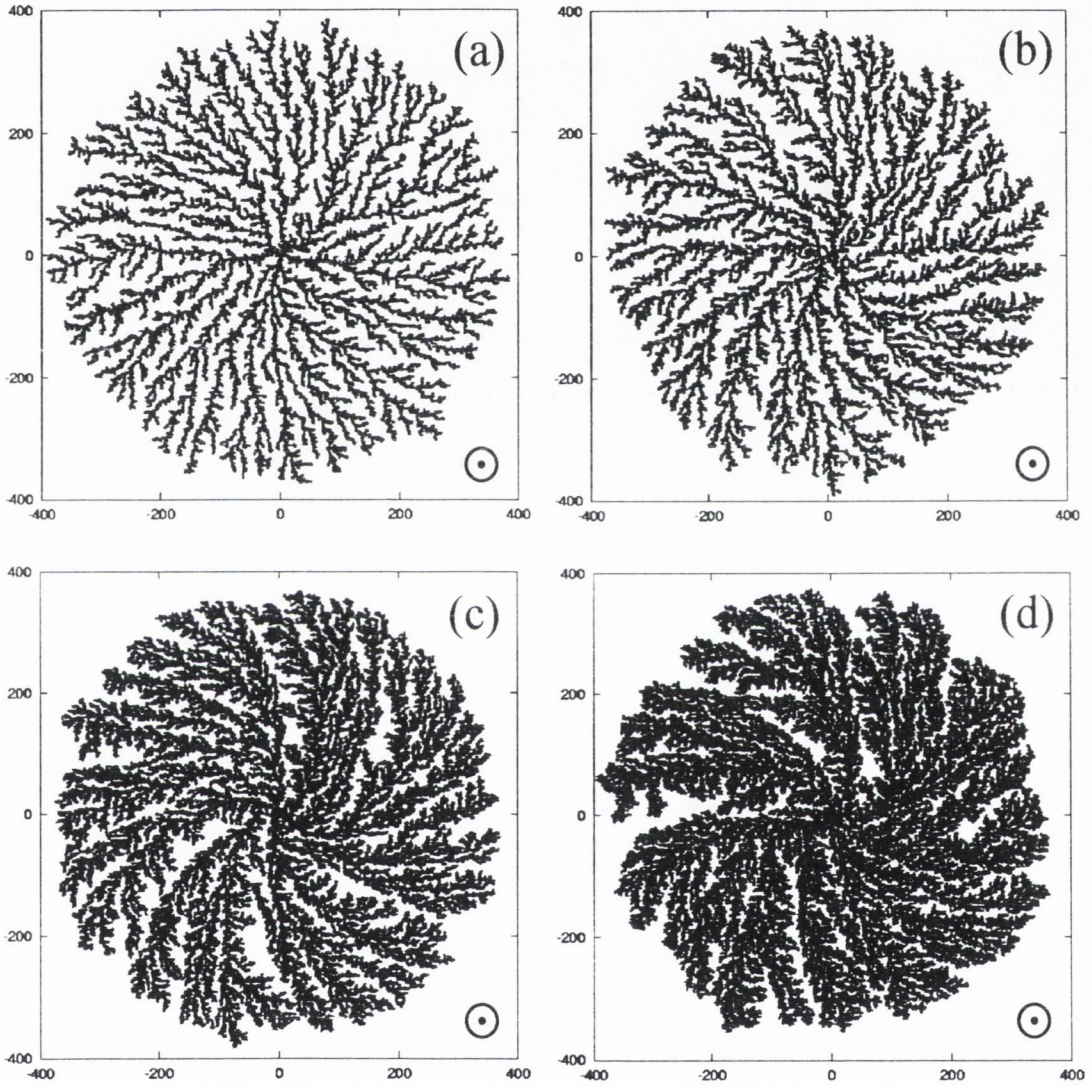
As before, when we reverse direction of the applied field by reversing the direction of the flow past the surface, we also change the chirality of the resultant deposit as in Fig.39.

The chirality achieved with this model is at all times in agreement with the experimental result of Fig.14.

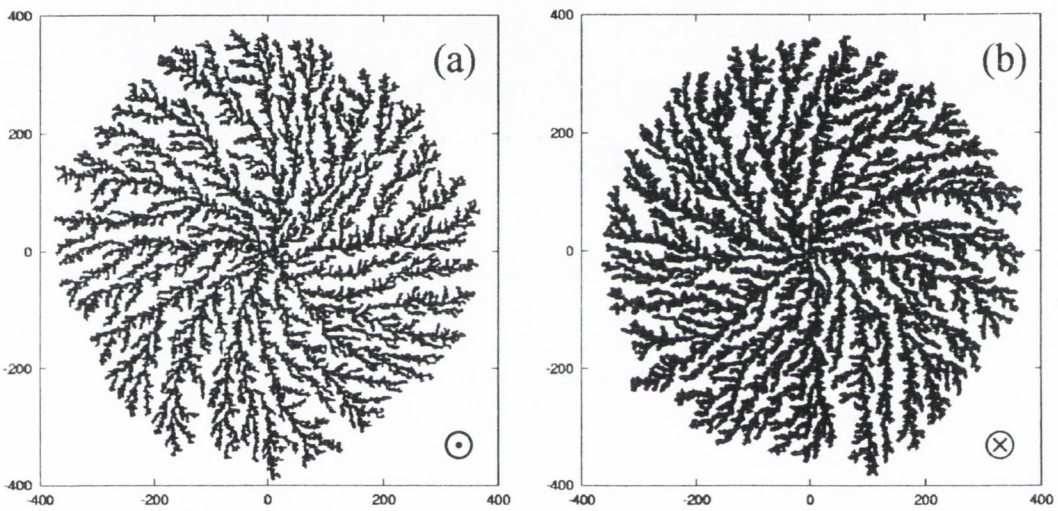
In the first model, where particles respond to the magnetic field in an uncorrelated fashion at every distance from the deposit, the spiral structure is the result of particles ‘backing up’ from the ends of branches. For both the bulk flow model and the experimental data, however, particles appear to flow along following the contour of the curving branch until they eventually stick to the end. That is to say that the branches curve and grow in the same direction as the flow of electrolyte. This important comparison seems to strongly suggest that the effect of the magnetic field is largely local or, at the very least, that the intricate structure of the deposit surface is essential to the growth process.

### 3.1.4 Reaction Kinetics

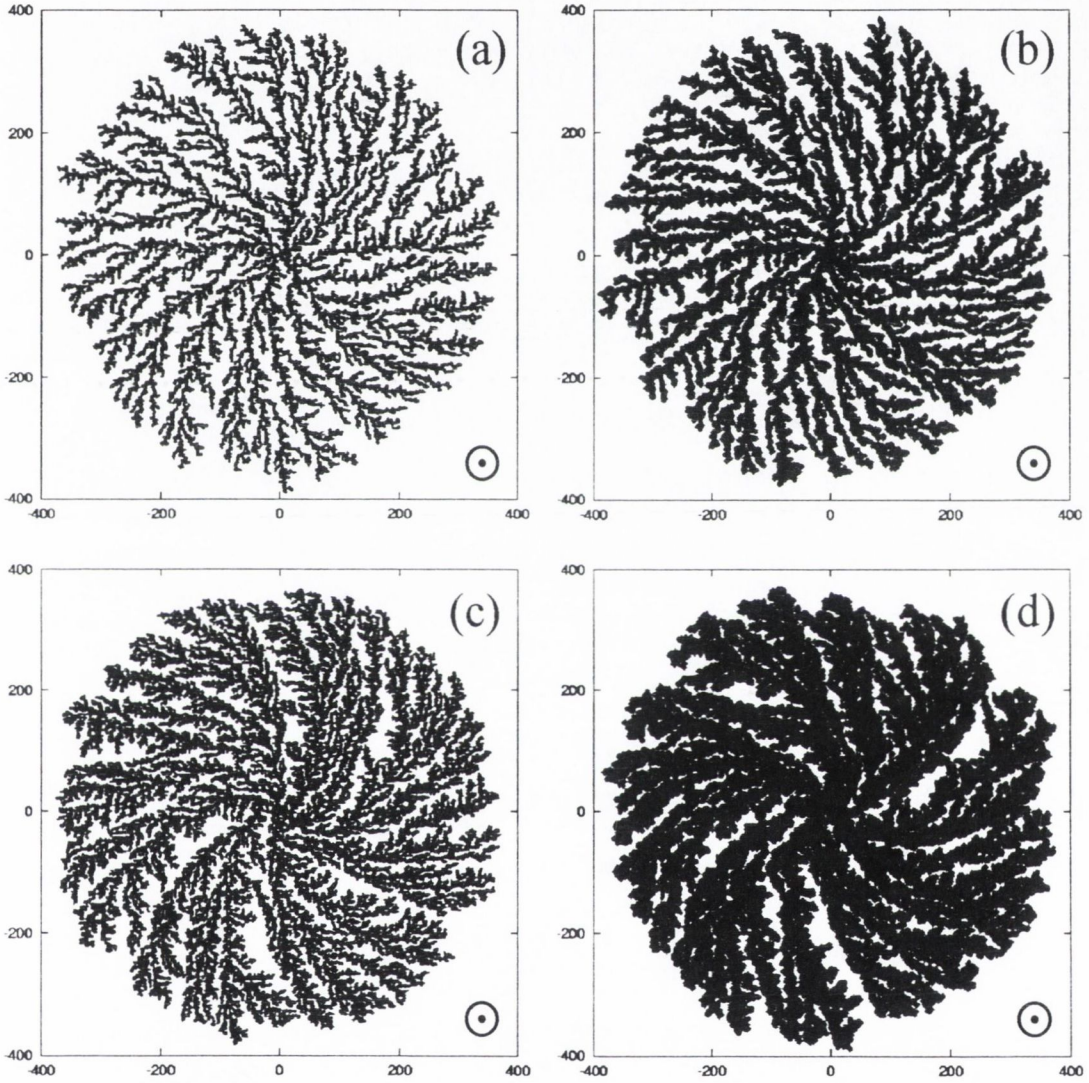
Reaction kinetics are modelled through a variable sticking probability  $p$ ,  $0 < p \leq 1$ . Low values of  $p$  represent slow reactions. Fig.40 outlines the numerical effect of varying  $p$  from  $p = 1.0$  and  $p = 0.1$  for  $B_{flow} = 0.1$  and  $0.2$  respectively. In each case the result is similar, in that individual branches become thicker and more clearly defined. The density of the deposit is increased, as is its fractal dimension.



38. When the field is applied into the plane of the cell, the particle tends to move through an angle  $(\theta_{dep} - \pi/2)$ . Deposits become more dense and compact for (a)  $B_{flow} = 0.05$ ,  $D_f = 1.82$ , (b)  $B_{flow} = 0.1$ ,  $D_f = 1.81$ , (c)  $B_{flow} = 0.2$ ,  $D_f = 1.84$  and (d)  $B_{flow} = 0.3$ ,  $D_f = 1.84$ .



39. The chirality of the deposit is reversed by reversing the direction of the magnetic field. This is achieved by defining flow past the surface as being through an angle (a)  $(\theta_{dep} - \pi/2)$  for a magnetic field *out of the plane* of the page and (b)  $(\theta_{dep} + \pi/2)$  for a magnetic field *into the plane*.



40. Using the bulk flow magnetic field model with  $V_{cen} = 0.05$ ,  $V_{mig} = 0.5$  then (a) has  $B_{flow} = 0.1$ ,  $p = 1.0$ ,  $D_f = 1.81$ ; (b)  $B_{flow} = 0.1$ ,  $p = 0.1$ ,  $D_f = 1.83$ ; (c)  $B_{flow} = 0.2$ ,  $p = 1.0$ ,  $D_f = 1.84$ ; and (d)  $B_{flow} = 0.2$ ,  $p = 0.1$ ,  $D_f = 1.85$ .

### 3.1.5 Vertical Cell

#### Gravity

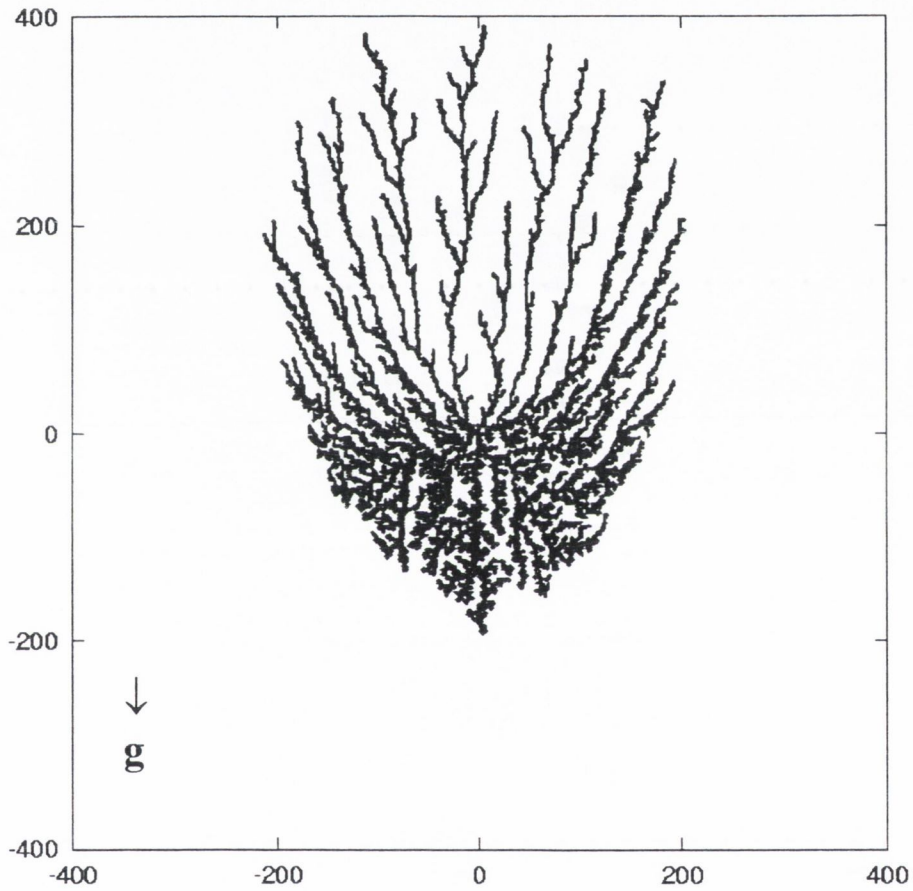
As detailed in Sec.2.2.1, gravity is introduced by considering swirls of fluid *above* the deposit, and upward flow at the *side* of the deposit, due to natural convection. It is important to consider both of these elements to correctly model the effect.

At a first approximation one might be tempted only to consider gravity acting downwards from high to low density regions. Doing so, even for a large gravitational factor  $G_{above} = 0.8$  (Eq.2.55), produces a slight asymmetry about the x-axis, but does not suffice to reproduce the columnar structures of Fig.15(a).

Instead we must also consider that gravity induces an upwards flow within a density gradient at a surface. Although the extent of the effect varies somewhat with the values of  $G_{side}$  (the multiplicative factor determining the extent of the preferential movement upwards along the surface from Eq.2.57 and 2.58) and  $\gamma_{side}$  (the angular range within which a particle is considered to be alongside an occupied site, Eq.2.56), the experimentally observed columnar structure of Fig.15(a) begins to emerge, indicating that it is upwards swirling at the sides which is predominantly responsible for the experimental result. A typical numerical result is shown in Fig.41.

#### Applied Magnetic Field

On applying the bulk flow, local magnetic field model, structures of the kind shown in Fig.42 emerge. The interplay between natural convection and the magnet field is very subtle [82]. This pattern has the interesting property that its chirality is somewhat ill-



41. Natural convection takes place *both* above and to the sides of branches of the deposit. The combined effect is shown for  $G_{above} = 0.5$ ,  $\gamma_{side} = 10^\circ$ ,  $G_{side} = 0.5$  and  $\gamma_{side} = 45^\circ$ .



defined. It has regions of strong, opposing chirality, in addition to regions where no clear spiralling is observed at all. This provides an interesting comparison with the experimental observation that in the vertical cell, although spiral patterns often emerge when a magnetic field is applied, the resultant chirality is variable; sometimes the chirality is the same as the horizontal case, sometimes opposite (as in Fig.15(b)), and often flat regions or regions of mixed chirality are observed within the same deposit.

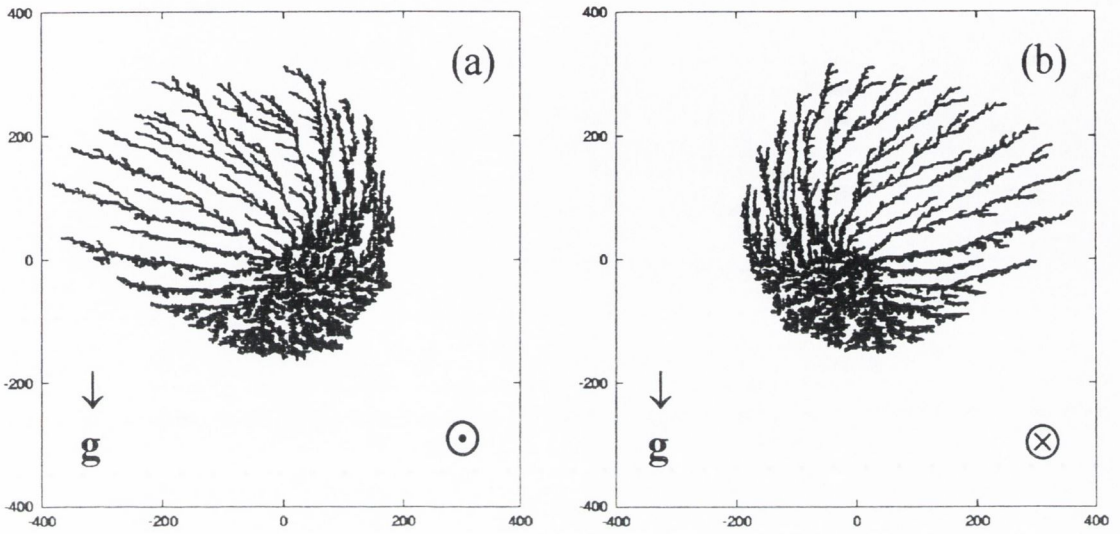
If the magnetic field is introduced via the ‘individual particle’ model, little variation from Fig.41 is observed. If, however, the ‘individual particle’ magnetic field model is applied, with  $\alpha_{magn} = 90^\circ$ , *close to the deposit only*, then Fig.42 is reproduced. This indicates that the key effect in this system is that of the magnetic field on the ions caught in the natural convective flow *close to the deposit surface*.

## 3.2 Linear Electrodes

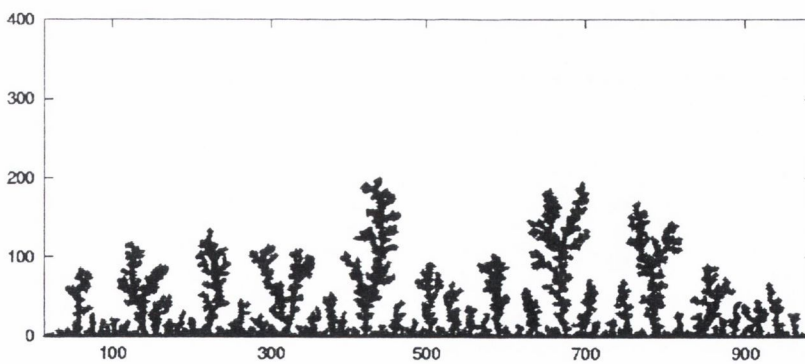
In the low concentration, low voltage regime, and the absence of a magnetic field, the linear equivalent of the basic DLA pattern of Fig.29(a) is shown in Fig.43. The experimental apparatus is held horizontally, but numerically the cathode is taken to be in the ‘downwards’ direction.

### 3.2.1 Applied Voltage

These fern-like structures become more dense with more clearly defined branches as the effects of applied voltage and concentration gradient are considered. Considering first the basic approximation that the effect of an applied voltage is to cause the metal ions to drift



42. Natural convection combined with a magnetic field applied (a) out of the plane and (b) into the plane. The mixed chirality of these structures is in agreement with experimental observation.



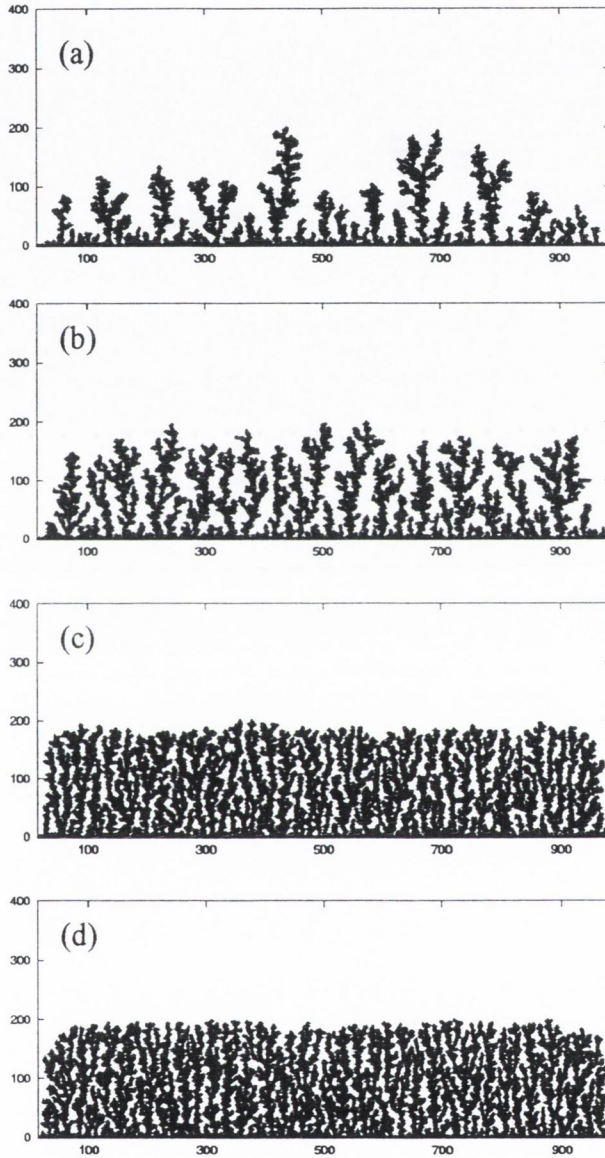
43. A linear DLA structure is achieved at low concentration and low voltage.

*downwards* towards the cathode, the results of Eq.2.59 are shown in Fig.44 as the patterns become more dense at increasing  $V_{linear}$ .

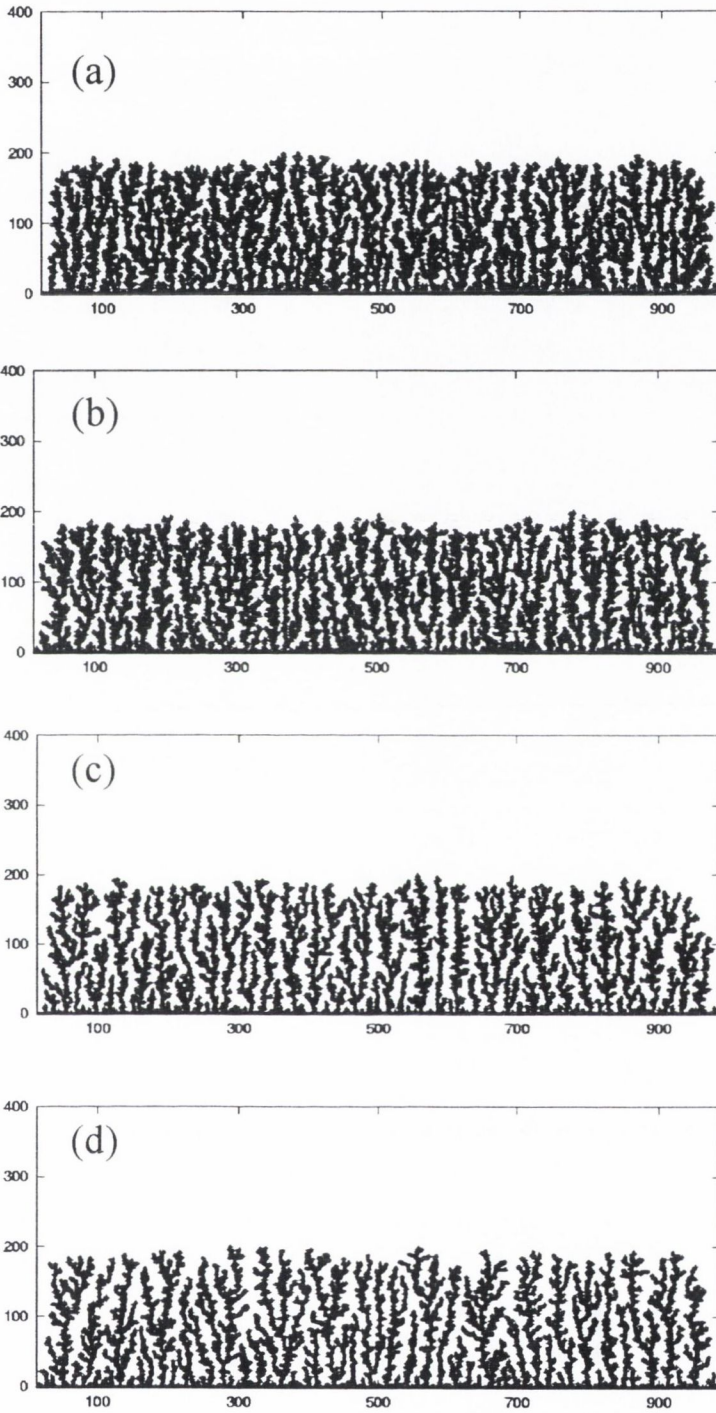
As in Sec.3.1.1, however, the voltage is more accurately modelled close to the electrode by considering that electric field lines are perpendicular to the surface. Thus over a region  $R_{look}$  (Fig.25) the ion is drawn in perpendicular to the surface with a  $1/d_{deposit}$  dependence, where  $d_{deposit}$  is the distance from the ion to the nearest occupied site. Outside  $R_{look}$ , the voltage is simply modelled as the basic downwards drift. Fig.45 shows the still dense though increasingly ramified results of this modification.

### 3.2.2 Applied Magnetic Field

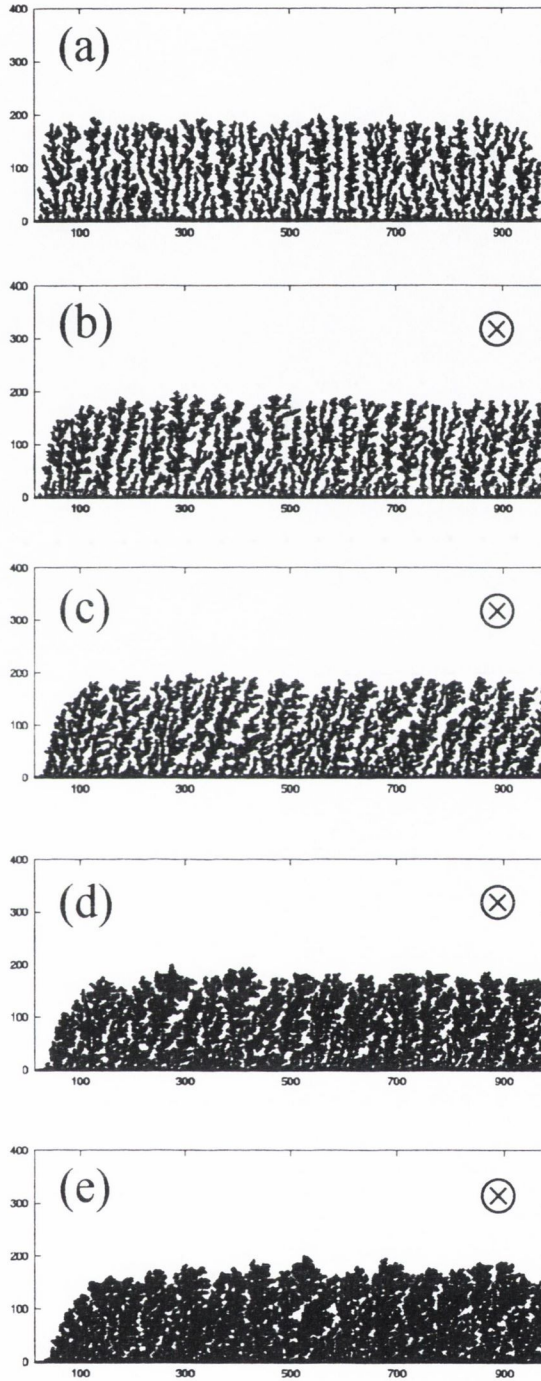
Fig.46 shows the effect of a magnetic field introduced through the second, ‘bulk flow’ magnetic field model. (Remember that in the ‘bulk flow’ scheme, the magnetic field is modelled as inducing a flow parallel to the surface of the deposit.) Clearly the deposit tends to ‘lean’ one way or another depending on the direction of the applied magnetic field. It should be pointed out the ‘individual particle’ magnetic field model also produces leaning deposits, but with a tilt *opposite* in direction to that of Fig.46. Again, as in the circular electrode case, it is the results of the *bulk flow model* which correctly reproduce the experimental directionality determined from the right-hand-rule (Fig.36). Fig.47 demonstrates the reversal in the direction of the ‘leaning’ effect. Similar effects have been observed by Tanimoto et al when modelling the effect of a magnetic field gradient [83].



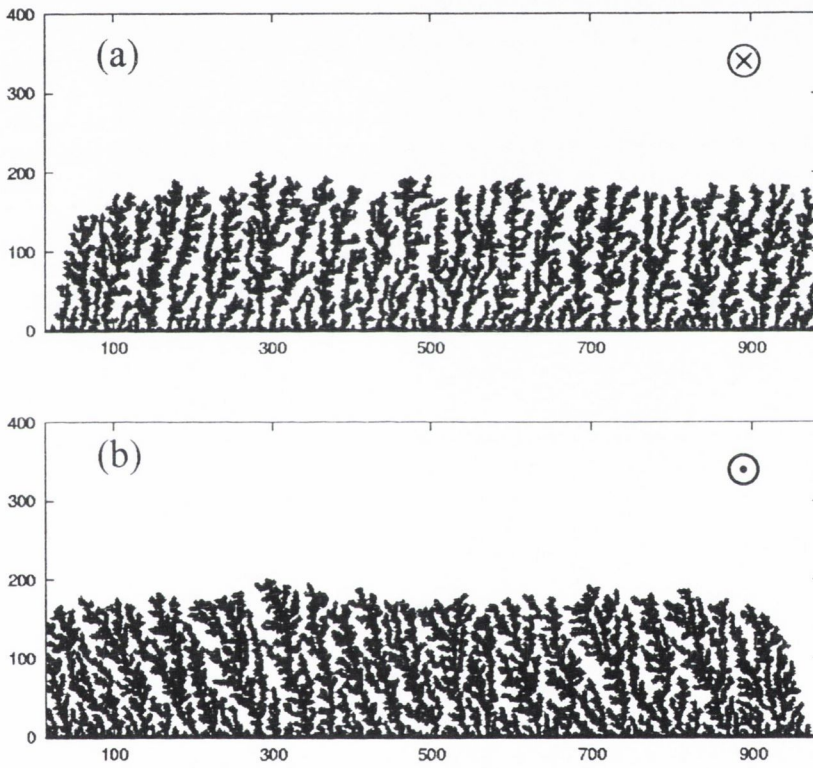
44. In the basic voltage model, ions drift preferentially downwards with (a)  $V_{linear} = 0$  (basic DLA as in the previous figure), (b)  $V_{linear} = 0.01$ , (c)  $V_{linear} = 0.1$  and (d)  $V_{linear} = 0.3$ .



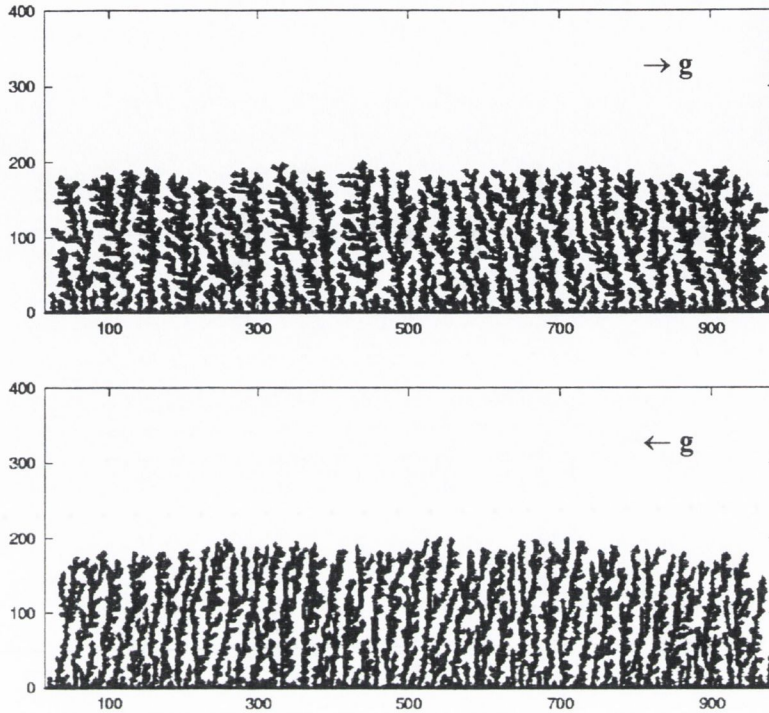
45. Far from the electrode, applied voltage is simply modelled as a downwards drift with  $V_{linear} = 0.1$ . Within a distance  $R_{look} = 10$  sites of the deposit, however, ions are drawn in perpendicular to the surface. (a)  $V_{mig} = 0.1$ , (b)  $V_{mig} = 0.3$ , (c)  $V_{mig} = 0.5$  and (d)  $V_{mig} = 0.7$ .



46. Using (a)  $B_{flow} = 0$  with  $V_{linear} = 0.1$  and  $V_{mig} = 0.7$  as a point of comparison, the figures consider results for a linear electrode when the magnetic field is considered as inducing a flow parallel to the surface of the deposit for (b)  $B_{flow} = 0.05$ , (c)  $B_{flow} = 0.1$ , (d)  $B_{flow} = 0.2$  and (e)  $B_{flow} = 0.3$ .



47.  $B_{flow} = 0.1$  for (a) the magnetic field applied into and (b) out of the plane of the page.

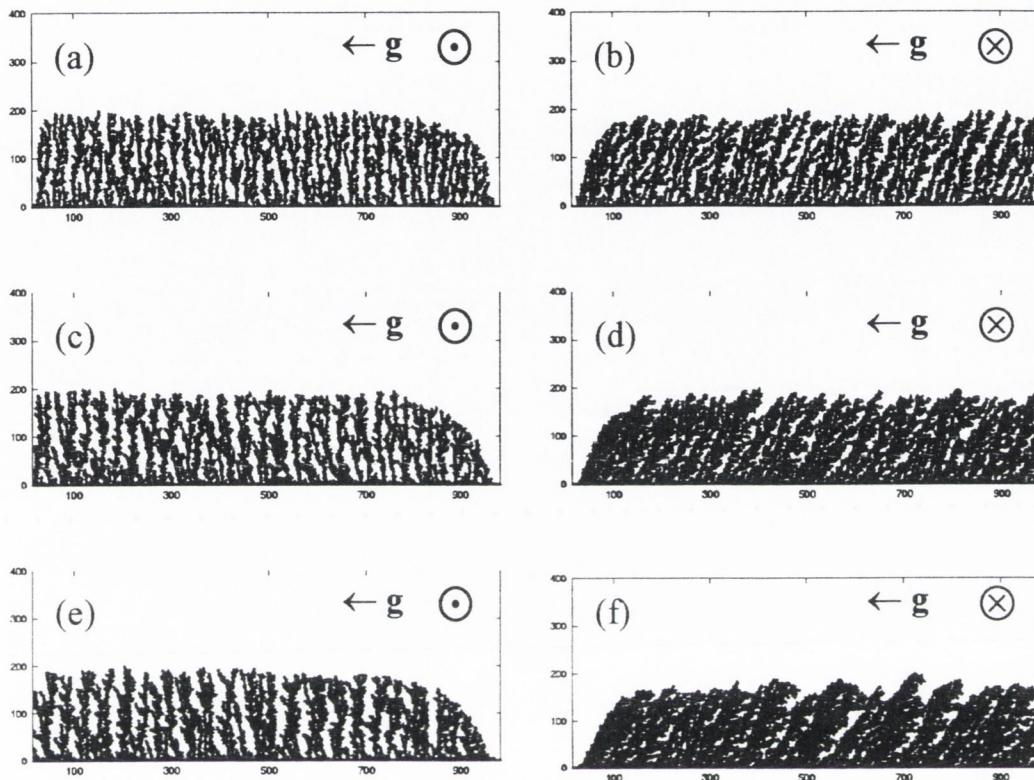


48. Numerical results for  $G_{above} = G_{side} = 0.7$  (a) and (b) for gravity applied in two opposite directions.

### 3.2.3 Gravity

Natural convection due to gravity is implemented, as in Section 2.2.1, by convective swirling, above and to the sides of branches of the deposit. The effect as shown in Fig. 48, is to cause a slight tilting of the branches of the linear deposit. The direction of this tilting is in agreement with the experimentally observed result as shown in the figure.





49. The combined effects of gravity and an applied magnetic field tend to either reinforce or cancel each other depending on their relative orientations as shown for  $G_{above} = G_{side} = 0.7$ , with  $B_{flow} = 0.05$  in (a) and (b),  $B_{flow} = 0.1$  in (c) and (d), and  $B_{flow} = 0.15$  in (e) and (f).

### 3.2.4 Gravity and Magnetic Field

Given that the effect of both gravity and magnetic field is to cause a tilting of the branches of the deposit, their combined effects tend to either reinforce or cancel each other depending on their relative orientations as shown in Fig.49. As little experimental data exists for the combined effect of gravity and magnetic field in the linear electrode case, however, the accuracy of this final prediction cannot yet be clearly determined.

# Chapter 4

## Magnetohydrodynamic Flow through an Open Channel

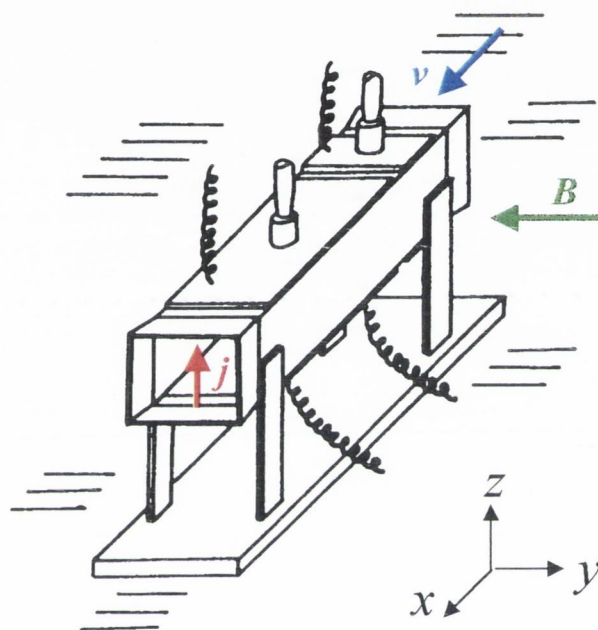
### 4.1 The Aogaki Cell

In the previous chapters we have considered the effect of a magnetic field on the morphology of electrodeposited structures. It has also been well established, however, that an applied magnetic field can enhance the plating current  $j$  at an electrode. In particular, a

$$j \propto B^{1/3} \quad (4.60)$$

relationship has been reported [32][86][94], and in some cases  $j \propto B^{1/2}$ [92], or  $j \propto B^{1/4}$  have been observed [84][85]. Leventis et al have derived a  $j \propto B^{1/3}$  relationship for deposition at millielectrodes [87]-[88], while White et al have shown an applied magnetic field to enhance the plating current on the scale of microelectrodes [89], where the force due to an applied magnetic field gradient has also been considered [90]- [91]. The relationship of Eq.4.60 was clearly established in a very neat experimental set-up devised by Aogaki et al. [93][94].

The system consists of a rectangular cell as in Fig.50, with electrodes placed on the top and bottom panels. The cathode is placed on the top panel, so that the current of metal ions passes vertically upwards from anode to cathode, in order to minimise effects due to natural convection. The entire cell is then immersed in a large bath filled with electrolyte.



50. The Aogaki Cell. Current flows vertically upwards from anode to cathode in the presence of a perpendicular applied magnetic field. This induces a bulk flow of solution through the cell, perpendicular to both  $j$  and  $B$  (Aogaki 1975).

The electrolyte may consist of  $\text{CuSO}_4$  in water with concentrations ranging from 0.02-0.076 M. In contrast to the system modelled in Chapter 2, this electrolyte also contains a strong, acidic supporting electrolyte of 1M  $\text{H}_2\text{SO}_4$ .

A magnetic field is applied across the cell, perpendicular to the direction of current flow, as shown in the figure. By Eq.1.36, a flow of the electrolyte is induced along the length of the cell, perpendicular to both  $j$  and  $B$ .

## 4.2 Interplay between Convective Flow and Diffusion

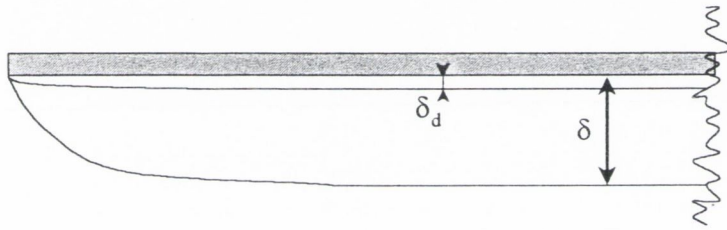
As described in Sec.1.5.5, in a quiescent electrolyte as the supply of ions in the vicinity of the electrode is exhausted, the diffusion layer will gradually extend into the bulk until its thickness is ultimately limited by natural convection. In the case, however, that there is hydrodynamic flow of the electrolyte past the electrode surface, the diffusion layer is constantly replenished with ions. The diffusion layer thickness can thus be maintained at a given value depending on the flow velocity <sup>6</sup>. Depending on the profile of the flow, relationships may be defined between the thickness of the diffusion layer  $\delta_d$  and the hydrodynamic boundary layer thickness  $\delta$ .

In particular in the case of bulk flow with velocity  $U$  past an infinite flat plate, the classic boundary layer profile, shown in Fig.51, is established. The thickness of such a boundary layer is generally [50] given by

$$\delta = 5\sqrt{\frac{\nu x}{U}} \quad (4.61)$$

---

<sup>6</sup> It is for this reason that some stirring mechanism, such as a paddle, magnetic stirrer, or rotating disc electrode, is often used to maintain a high, constant current in industrial processes.



51. In the case of flow past a flat plate, the classic hydrodynamic boundary layer profile emerges. The diffusion layer is also shown for comparison.

The  $x$  and  $y$  components of velocity within the boundary layer are given by Levich [49] as

$$v_x = \frac{1.33}{4} \frac{U^{3/2}}{\nu^{1/2} x^{1/2}} y \quad (4.62a)$$

$$v_y = \frac{1.33}{16} \frac{U^{3/2}}{\nu^{1/2} x^{3/2}} y^2 \quad (4.62b)$$

These expressions are then used in the solution of the convective diffusion equation (Eq.1.17) given, in the steady state, by

$$v_x \frac{\partial c}{\partial x} + v_y \frac{\partial c}{\partial y} = D \left( \frac{\partial^2 c}{\partial x^2} + \frac{\partial^2 c}{\partial y^2} \right). \quad (4.63)$$

with the additional approximation that  $\frac{\partial^2 c}{\partial x^2} \ll \frac{\partial^2 c}{\partial y^2}$  so that the first term on the right hand side may be neglected. From this, Levich ultimately derives the expression

$$\left( \frac{\partial c}{\partial y} \right)_{y=0} = 0.34 (c_\infty - c_0) \sqrt{\frac{U}{\nu x}} \left( \frac{\nu}{D} \right)^{1/3} \quad (4.64)$$

for the concentration gradient at the electrode surface. Given the assumption of Section 1.5.5 that the concentration gradient across the diffusion layer is roughly linear, then the diffusion layer thickness can be given as

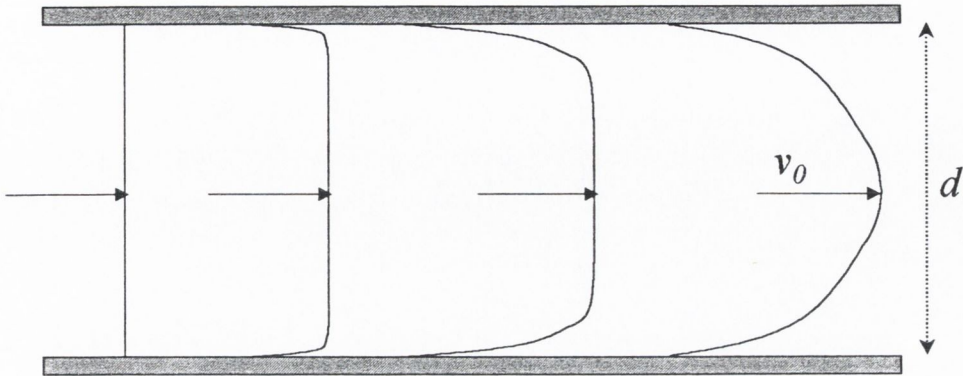
$$\delta_d \approx 3 \sqrt{\frac{\nu x}{U}} \left( \frac{D}{\nu} \right)^{1/3} \quad (4.65)$$

which combined with Eq.4.61 relates it to the boundary layer thickness by

$$\delta_d \approx 0.6 \left( \frac{D}{\nu} \right)^{1/3} \delta. \quad (4.66)$$

Given that the systems under consideration have diffusion coefficients of  $D \sim 1 \times 10^{-9} \text{ m}^2\text{s}^{-1}$ , and viscosity  $\nu \sim 1 \times 10^{-6} \text{ m}^2\text{s}^{-1}$ , we can, in the case of flow past a long, flat electrode, make the rough approximation that

$$\delta_d \approx 0.1 \delta. \quad (4.67)$$



52. Poiseuille flow into a narrow pipe.

Therefore, for the simple geometry of current plating to a flat electrode, in the presence of a flow of the electrolyte with bulk velocity  $U$  past the electrode, we could estimate the diffusion current density  $j$  simply by calculating the thickness of the hydrodynamic boundary layer, and then, from Eq.4.67, inserting a value for  $\delta_d$  into Eq.1.22.

In our geometry, however, we are considering flow *between* two flat plates, separated by some distance  $d$ . In the case that  $d$  is very large compared to the lengths of the plates, then the flow past each plate is essentially that described in Eq.4.62. As  $d$  is reduced, however, the two boundary layers begin to interact with each other, resulting in flow which is intermediate between the boundary layer flow of Fig.51 and the *Poiseuille* flow of Fig.52. Unlike boundary layer flow, where velocity gradients are restricted to regions close to the walls with a uniform velocity throughout the bulk solution, here the velocity gradient persists into the bulk, with the velocity reaching a maximum value of  $v_0$  only at the centre of the channel. There is no  $y$ -component to the velocity at any point in the channel.

Clearly in this case the thickness of the diffusion layer cannot be defined by the simple approximation of Eq.4.67. Rather an expression, given by Levich [49], for the concentration gradient at the wall in this instance is

$$\left(\frac{\partial c}{\partial y}\right)_{y=0} = 0.845 (c_{\infty} - c_0) \left(\frac{v_0}{Ddx}\right)^{1/3} \quad (4.68)$$

on the assumption that  $\nu \gg D$ . This equation is valid over a distance  $H$  along the plates, over which a steady state diffusion layer is being established. According to Levich [49],  $H \sim \text{Re} \cdot \text{Pr} \cdot (d/2)$ ; typically  $H \gg h$ , where  $h$  is the distance over which a steady-state velocity profile is established. Beyond  $H$ ,  $\delta_d$  is independent of  $x$ .

### 4.3 Aogaki's Theoretical Prediction and Experimental Result

Based on the theory of the previous section, Aogaki et al. [94] have derived an elegant theoretical model for the magnetic field effect on the current density in this system. Firstly [93] it is established that, in the case of large separation of the plates, the bulk velocity of the flow is related to the driving magnetic field by

$$\frac{1}{2}U^2 = -\frac{1}{\rho}\Delta p_0 + \frac{1}{\rho}B\bar{j}(x_2 - x_1) \quad (4.69)$$

where  $\bar{j}$  is the average current density over the electrode,  $\rho$  is the density of the fluid,  $\Delta p_0$  is the pressure difference between the outlet of the channel and  $x = \infty$  which, under standard experimental conditions, is negligibly small, and  $x_1$  and  $x_2$  indicate the range of the electrode on an x-axis which has its zero point at the opening of the channel.



Combining this with Eq.1.22, under the assumption of boundary layer flow past the plate, the following expression for  $\bar{j}$  is determined as

$$\bar{j} = H c_{\infty}^{4/3} B^{1/3} - 0.333 \Delta p_0 (x_2 - x_1)^{-1} B^{-1} \quad (4.70)$$

given that at limiting current the ion concentration at the wall  $c_0 = 0$ . The factor  $H$  is given by

$$H = 0.753 (nFD)^{4/3} (\nu/D)^{4/9} \nu^{-2/3} \rho^{-1/3} (\sqrt{x_2} - \sqrt{x_1})^{4/3} (x_2 - x_1)^{-1}. \quad (4.71)$$

This theoretical prediction agrees with their experimental data to within a multiplicative factor of  $\gamma^{1/3}$ , where  $\gamma$  takes different values of order 0.1 for different geometries. In the case of the geometry considered here  $\gamma = 0.118$ .

In the case of Poiseuille flow [92], however, the current density is expected to vary as

$$\bar{j} = K c_{\infty}^{4/2} B^{1/2} \quad (4.72)$$

where

$$K = 0.504 (nF)^{3/2} Dh^{1/2} (\nu\rho l)^{-1/2}, \quad (4.73)$$

and  $h$  is the separation between plates of length  $l$ .

## 4.4 Numerical Model

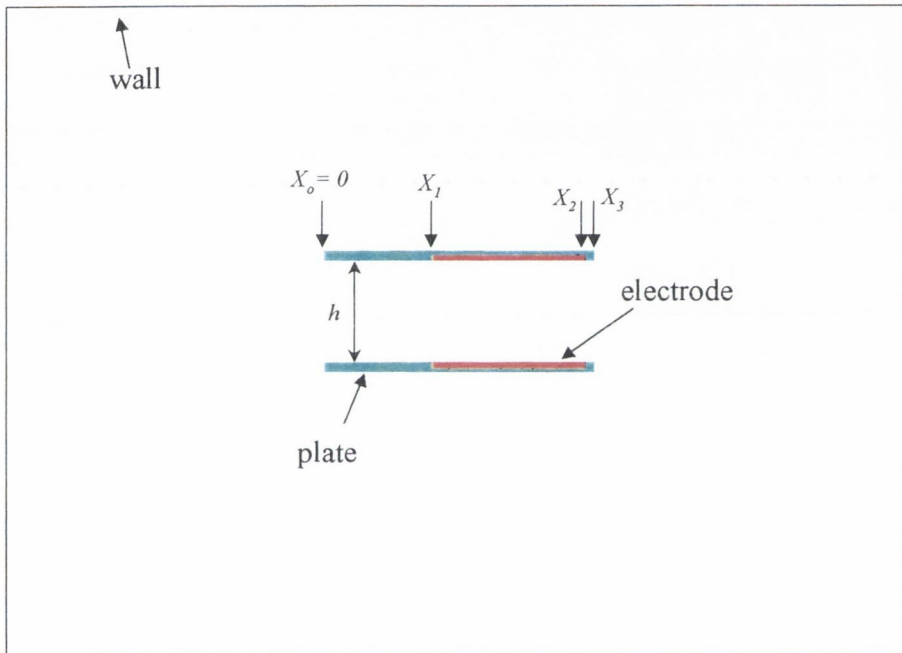
### 4.4.1 The Full Geometry

The problem was approached numerically in a manner similar to that adopted by Ngo Boum et al [95]-[97]. The model was developed using the commercial finite element hydrodynamics package, FLUENT. (Finite difference methods, however, can also be applied to such convective-diffusion problems as outlined by Fahidy [98].) Here the system was simplified to a 2-dimensional model as in Fig.53 consisting of two flat plates contained within a rectangular cell. Regions are defined on the plates which represent the electrodes between which current passes.

The geometry is defined using a general script so that all of the key parameters of the system are easily varied; the length, thickness and separation of the plates, the dimensions of the outer container, as well as the boundary conditions on all surfaces. In the case of the results presented we have used the Aogaki's geometry with  $x_o = 0$ ,  $x_1 = 4.5$  cm,  $x_2 = 9.5$  cm and  $x_3 = 10.0$  cm.  $h = 5.0$  cm and the separation between the outer walls is 30 cm.

An initial value for current density is defined everywhere between the electrodes. A script was written to add the Lorentz bulk  $\mathbf{j} \times \mathbf{B}$  force term to the Navier-Stokes Eq.1.37. The three key dynamical equations governing the behaviour of the system are then solved *simultaneously*; namely the Navier-Stokes equation Eq.1.37,

$$\frac{\partial \mathbf{v}}{\partial t} + (\mathbf{v} \cdot \nabla) \mathbf{v} = -\frac{1}{\rho} \nabla p + \nu \nabla^2 \mathbf{v} + \frac{\mathbf{j} \times \mathbf{B}}{\rho}$$



53. The basic two-dimensional geometry consists of two flat plates contained within a rectangular cell.

the continuity equation Eq.1.25

$$\nabla \cdot \mathbf{v} = 0$$

and the steady state convective diffusion equation Eq.4.63

$$D\nabla^2 c - \mathbf{v} \cdot \nabla c = 0.$$

From the final equation we determine the value of the concentration gradient  $(\partial c / \partial y)_{y=0}$  at the cathode surface. Thus from

$$j = nFD \left( \frac{\partial c}{\partial y} \right)_{y=0} \quad (4.74)$$

the current at every point on the electrode surface is calculated. As the present geometry consists simply of two parallel electrodes of macroscopic dimensions, we assume that the current passes in a straight line, perpendicular to the plates. Thus for a given value of  $x$  along the plate, the current density at  $y$  is equal to the current density calculated at the wall; that is  $j(x, y) = j(x, y = 0)$ . So new values for  $j$  have now been assigned to every point between the electrodes.

These new  $j$  values for the Lorentz force are passed back into the Navier Stokes equation, which generates new values for  $j$  and so on .... Thus for a given value of  $B$ , we repeatedly solve for  $j$  until the system converges on a self-consistent solution.

Note that although a single average value of  $j$  is used everywhere at the very first iteration, thenceforth every point on the mesh between the electrodes is assigned its own local value of  $j$ . In establishing convergence between successive iterations, however, the point of comparison is the average value of  $j$  along the cathode surface.

The concentration boundary conditions are as follows:

- Container walls :  $c = c_\infty$ ;
- Non-electrode plate walls :  $c = c_\infty$ ;
- Cathode surface :  $c = 0$ ;
- Anode surface :  $c > c_\infty$

Two approaches to the boundary conditions on velocity have been separately examined, namely:

- $v = 0$  on all solid surfaces;
- $\partial v / \partial x = 0$  at the surfaces to the left and right of the outer container (i.e. these are not solid surfaces, but infinite sources and sinks of fluid), and  $v = 0$  on all other solid surfaces.

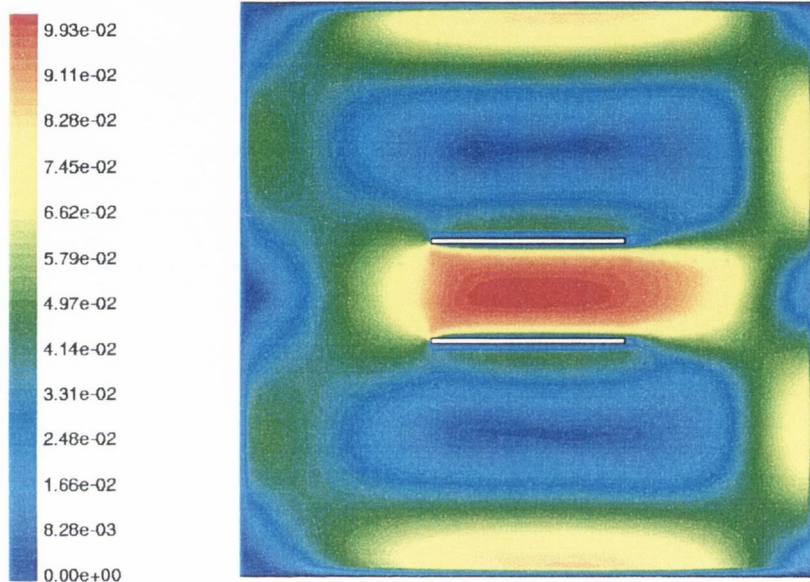
# Chapter 5

## Magnetohydrodynamic Simulation

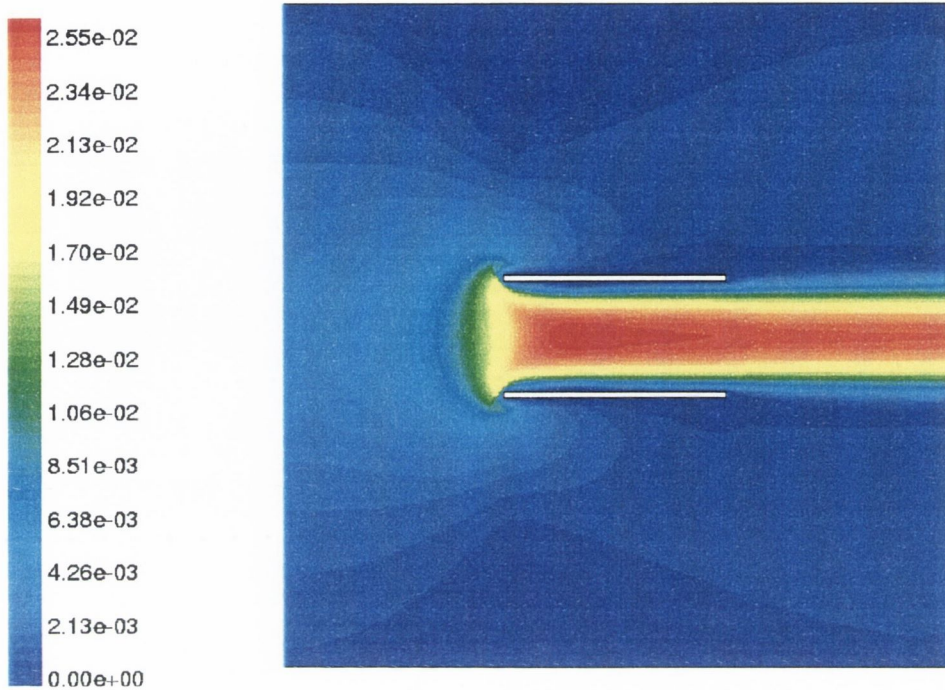
### 5.1 Velocity Profiles

In the first instance, we simulated the entire system consisting of two flat plates (electrodes displaced right of centre as in Fig.53) immersed in electrolyte contained between four solid walls. A typical velocity profile emerging from this simulation is shown in Fig.54. The Lorentz force acting on the solution carrying current between the electrodes, by the continuity equation, induces a bulk flow of the electrolyte down through the whole length of the cell. The high velocity jet emerging from the end of the tube, can result in complex flows at the walls of the outer container as seen in the figure. This behaviour in the outer regions of the system has a negligible effect on the flow within the tube, yet adds considerably to the computation time and the difficulty in achieving convergence of the solution. As a result, the system was somewhat simplified by changing the boundary conditions on the left and right hand walls of the outer container. The top and bottom surfaces remain solid, with the  $\mathbf{v} = 0$ , 'no-slip', boundary condition. Now, however, the left and right hand faces are given zero gradient boundary conditions; that is to say that they provide infinite sources and sinks of fluid.

A typical velocity profile obtained using these new boundary conditions is shown in Fig.55 for a concentration  $c_\infty = 76 \text{ mol/m}^{-3}$  at an applied magnetic field of  $B = 0.2 \text{ T}$ . Along the interior surface of the plate walls, a hydrodynamic boundary layer is established.



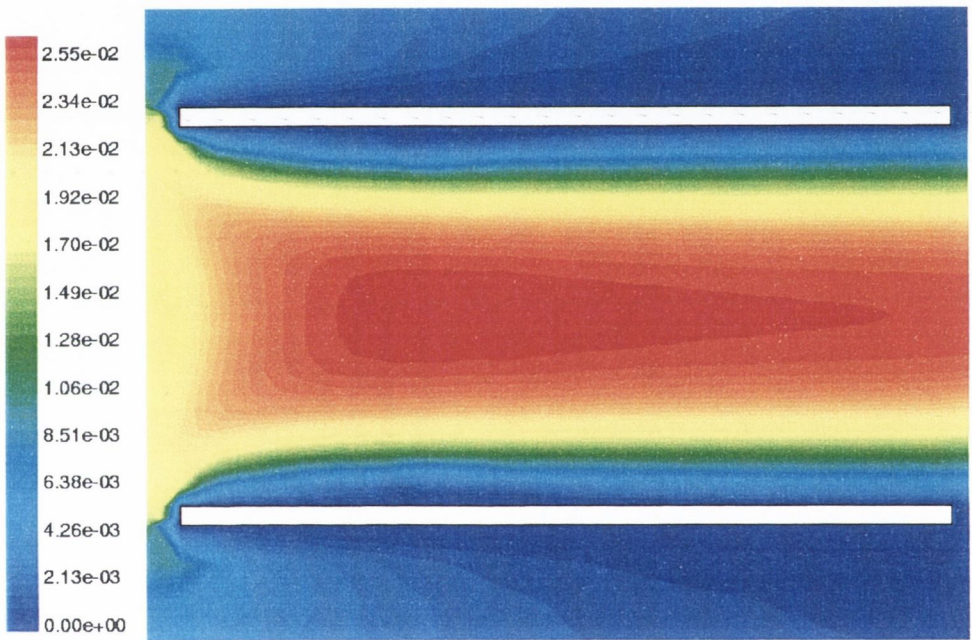
54. The two flat plates are surrounded by four solid walls. Current flowing between the electrodes experiences a Lorentz force which forces fluid down along the length of the cell. At high fields, the high velocity flow results in complex motion at the walls of the surrounding container.



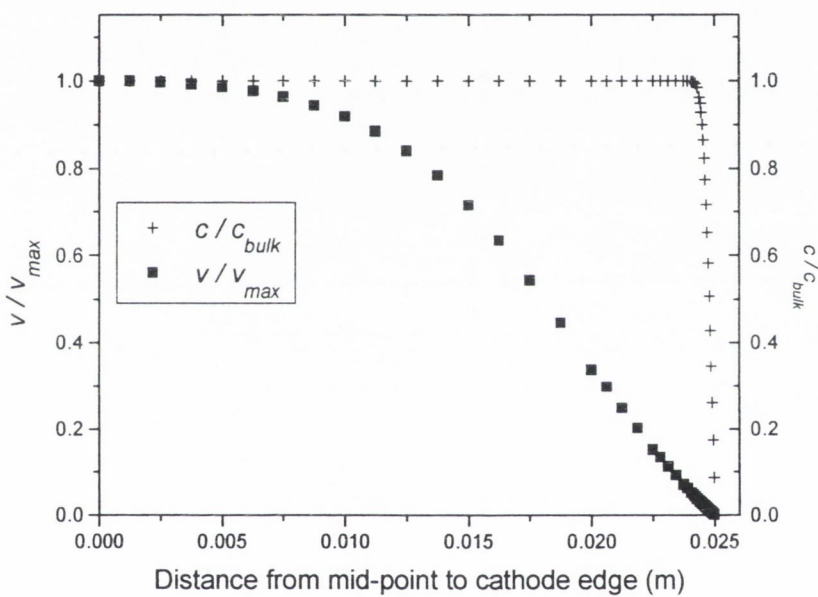
55. As in the previous figure, but now the left and right faces of the outer container have been given zero gradient boundary conditions, so that they act as infinite sources and sinks for the fluid.

Fig.56 zooms in on this profile between the plates. The thickness of the diffusion layer is very small compared to the region over which the velocity gradient occurs as illustrated in Fig.57 which compares the velocity and concentration profiles along a line from mid-point between the plates to the electrode edge at the middle of the cathode. Note that although the two boundary layers interact with each other to some extent, this is *not* Poiseuille flow.





56. The velocity profile between the plates.



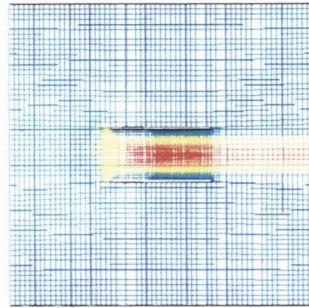
57. The velocity and concentration profiles plotted as  $v/v_{max}$  and  $c/c_{\infty}$  respectively along a line drawn from the mid-point between the electrodes to the edge of the cathode. The diffusion layer is clearly contained well within the hydrodynamic boundary layer.

## 5.2 The Mesh

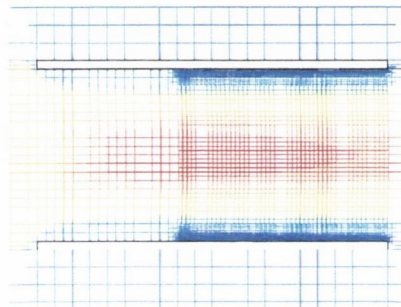
The biggest difficulty in attempting to solve this problem, as should be apparent from Figs.55-57, is that the regions of interest in the problem occur over many different orders of magnitude. The outer cell has width  $3 \times 10^{-1}$  m, although significant variations in the velocity profile occur only over the width of the tube  $\sim 1 \times 10^{-2}$  m, but the concentration variation occurs entirely within the diffusion layer  $\sim 1 \times 10^{-4}$  m. This demands the use of a highly refined mesh along the electrode wall, but the use of such a mesh at every point in the system would be an enormous waste of resources. In fact, it transpired that meshing proved to be one of the most time-consuming aspects of the problem. Ultimately the mesh used was refined to successively high degrees over different regions of the problem, as illustrated in Fig.58.

## 5.3 Current Density Profiles

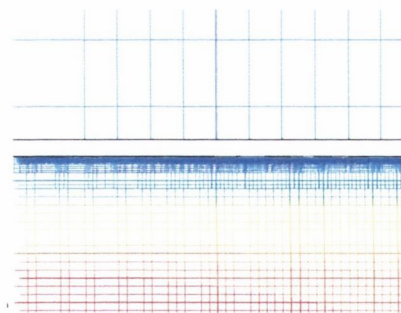
Once the solution has reached convergence, the value of  $(\partial c / \partial y)_{y=0}$  is calculated at each point on the electrode surface. From this, the diffusion current density  $j$  is calculated from Eq.4.74. As diffusion is the dominant mode of mass transport in this system, at each node  $(x, y)$  we assign  $j(x, y) \equiv j(x, 0)$ . Fig.59 considers the variation in  $j$  along the electrode surface at low  $B$  values. For values of magnetic field up to  $B \approx 0.2$  T, the current displays a sharp peak at the leading edge of the electrode, which decreases gradually along its length. This corresponds clearly with the behaviour (Fig.59(b)) of the concentration gradient over the same region. Here, due to the flow of fluid past the plate, a sharp increase in the



(a)



(b)



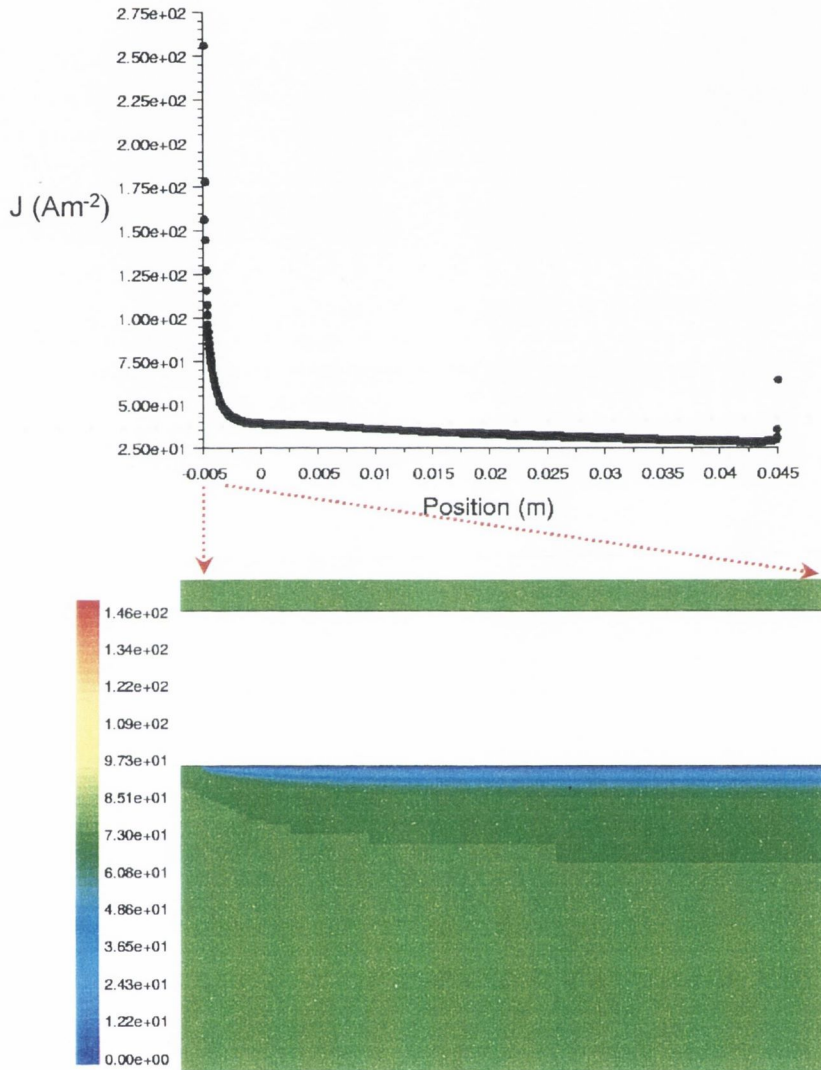
(c)

58. The mesh was refined to different degrees over different regions of interest as illustrated by increasing zooms; (a) the whole system, (b) between the plates, (c) at the electrode surface.

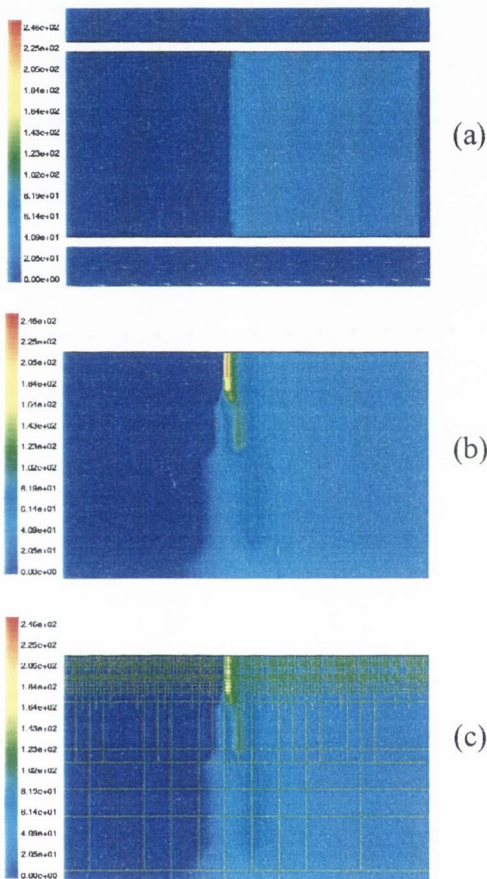
diffusion layer thickness from zero is observed at the electrode edge, which then gradually increases in value along the surface. Fig.60 shows the steady-state distribution of current density between the plates. (b) shows the sharp peak in the current density at the leading edge of the plate which is to some extent smoothed out by the mesh at a distance from the electrode as shown in (c).

Less clear cut, however, is the profile of  $j$  along the electrode surface at higher  $B$  values, as shown in Fig.61(a). In this case the current density shows a sharp peak at the very edge of the electrode which suddenly drops off, only to rise more gradually to a maximum further down the plate. This peak falls off again slowly before peaking again briefly at the end of the plate. Fig.61(a) shows the corresponding concentration distribution at the surface. Here we see nothing like the smooth, boundary layer style diffusion layer profile of Fig.59(b) where the ionic material is dragged down along the channel by the fluid flow. In this case rather, ions appear to have been dragged backwards away from the leading edge of the electrode to some extent. In this case the diffusion layer is in fact quite thick at the leading edge of the electrode and decreases in thickness up to a point some distance along the electrode beyond which it slowly increases in thickness again. As the solution of the convective-diffusion equation 4.63 depends strongly on the solution of the Navier-Stokes equation, we turn to the velocity profile for an explanation.

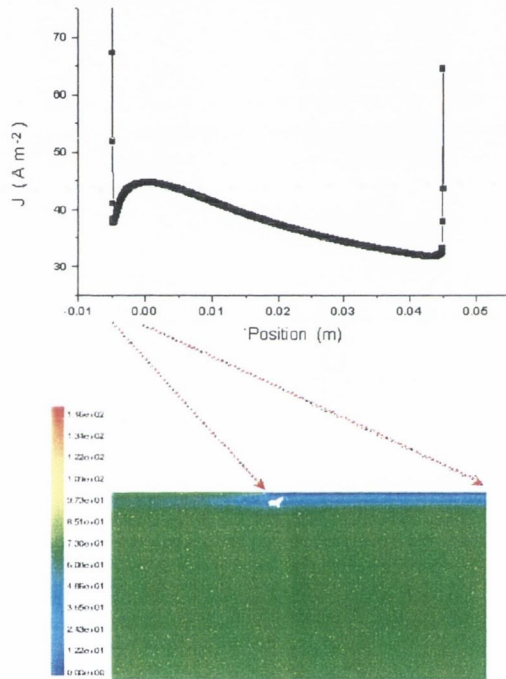
The colour plots of the flow in Fig.55-56 seem to demonstrate smooth, laminar flow through the channel in the positive  $x$ -direction. Examining this flow more carefully, however, using arrow plots to assess not only the *magnitude* of the velocity, but also the *direction* of the flow, points to an interesting phenomenon; eddy-current swirling is observed



59. For  $B = 0.2$  T, and  $c_\infty = 76$  mol/m<sup>3</sup>, (a) the profile of current density along the electrode surface shows a sharp peak at the leading edge, which decreases gradually; (b) the corresponding concentration profile shows a sharp increase in the diffusion layer thickness at the electrode edge, gradually increasing over the length of the electrode.



60.(a) The current distribution between the electrodes at  $B = 0.2$  T. (b) zooms in by a factor of 10 on the sharp peak in the current density at the leading edge of the plate which is to some extent smoothed out by the mesh at a distance from the electrode as shown in (c).



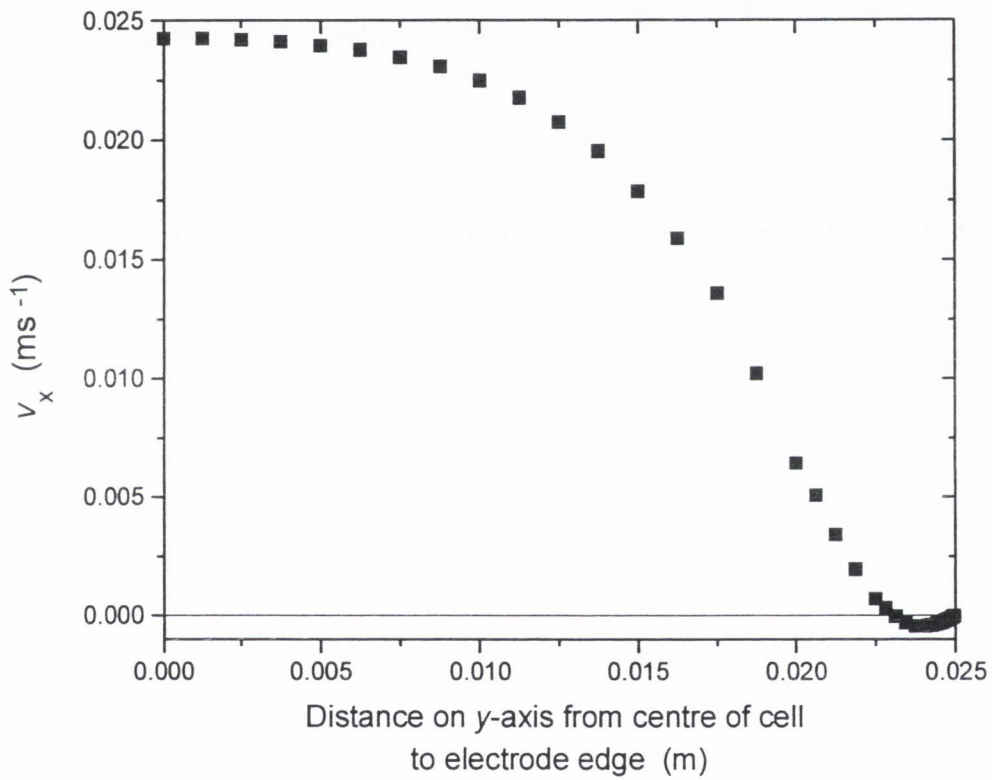
61. For  $B = 0.3$  T, and  $c_\infty = 76$  mol/m<sup>3</sup>, (a) the current density along the surface of the electrode; (b) the corresponding concentration profile at the leading edge of the electrode.



along the walls at the mouth of the opening. Even in the case of low  $B$ , as shown in Fig.63 for  $B = 0.2$  T, just inside the mouth of the channel a region can be identified at the plate surface where the fluid actually flows in the *negative*  $x$ -direction. Note that although the magnitude of the velocity in this region is very tiny, it is nonetheless reverse flow. At low  $B$ , however, this eddy current swirling does not extend as far as the electrode surface, and so the diffusion layer remains undisturbed.

At higher  $B$ , on the other hand, this swirling becomes more intense, persisting right down over the beginning of the electrode, as illustrated in Fig.64. The vortex region, where the velocity profile rotates from reverse to laminar flow can be identified some distance along the electrode surface. The profile of  $v_x$  along the  $y$ -axis, shown in Fig.62, indicates the region of reverse flow at the electrode edge. This accounts for the unusual concentration distribution of Fig.61(b) insofar as the reverse flow drags ions away from the electrode, destroying the anticipated smooth diffusion layer of Fig.59(b). The outline of the diffusion layer is thus separated into two regions, one contained within the boundary layer of flow in each of the two directions, with a minimum thickness at the vortex point between the two flow directions.

This phenomenon, and its effect on the current distribution, are most clearly illustrated in Fig.65. These graphs plot normalised values of  $j$  at the electrode surface, and normalised values of  $v_x$  100  $\mu\text{m}$  from the plate surface at and around the electrode. Here we see the region of eddy current swirling as a negative region on the plot of  $v_x$ . For  $B = 0.2$  T, the region of reverse flow does not extend to the electrode, and the current density profile is as expected in the case of laminar flow. For the case of  $B = 0.3$  T, however,

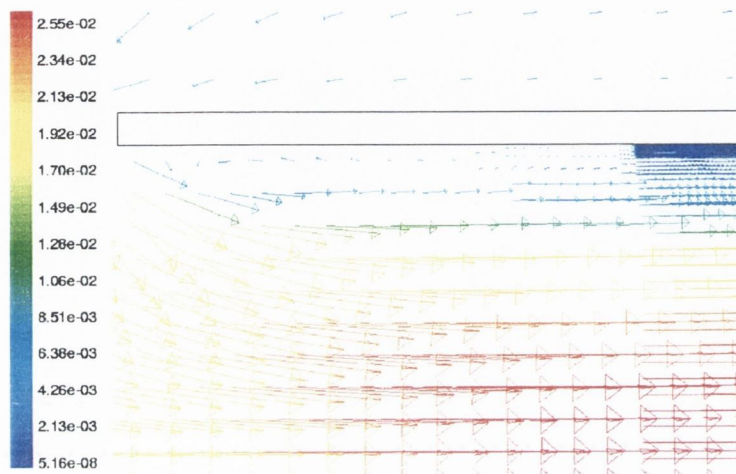


62. At the leading edge of the electrodes, plot of  $v_x$  along the  $y$ -axis from the mid-point between the electrodes to the cathode. Negative values indicate the region of reverse flow.

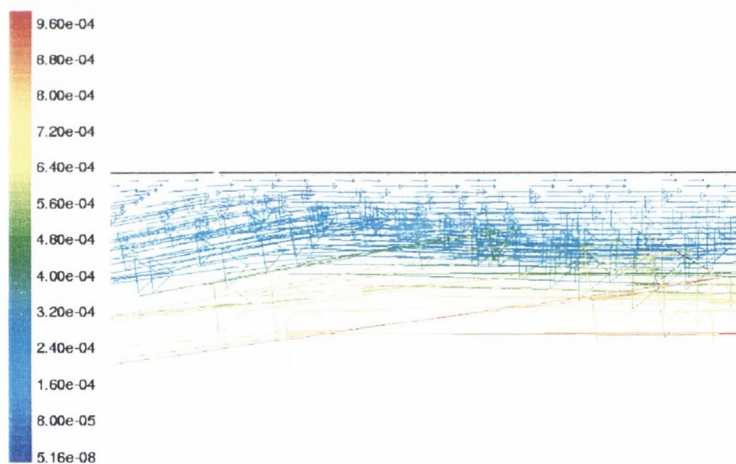
where the reverse flow does extend beyond the electrode edge, we can identify that region of the electrode where  $j$  drops from its edge peak, and then climbs to the second maximum as corresponding with the region of reverse flow. As the flow returns to forward flow, the current density profile tails off to lower values with a profile similar to that of the laminar flow  $B = 0.2$  T case. We also see in both cases that the edge peak of  $j$  has a small local effect on the velocity profile, but is clearly not responsible for the reverse flow, which is a hydrodynamic effect of the electrolyte passing over the outer edge of the channel.

## 5.4 Current Enhancement

Considering now the overall variation of  $j$  as a function of  $B$ , for concentrations of  $c_\infty = 76 \text{ mol/m}^{-3}$  and  $28 \text{ mol/m}^{-3}$ , the results are shown in Fig.66. Overall an excellent agreement is found with both experiment and theoretical prediction. At fields  $B \gtrsim 0.3$  T,  $j$  plotted against  $B^{1/3}$  falls nicely in with a linear fit as shown in the figure. At lower fields, however, the current value tends to level out towards the value of the zero-field limited diffusion current of Eq.1.24. The limiting diffusion current is determined, in the absence of forced convection, by the time  $t$  before natural convective effects limit the growth of the diffusion layer thickness. As this system is devised with the cathode placed horizontally on the upper wall of the cell, specifically to reduce natural convective effects, we may expect that  $t$  is somewhat larger than the typical value of 30 s for a vertical electrode. From the Cottrell plot of Fig.67 we may expect the limiting current density to be of the order  $30 \text{ Am}^{-2}$ . This is approximately the value that limits the magnetic field effect of Fig.66(a). This important point deserves emphasis, as experimental data presented in the literature

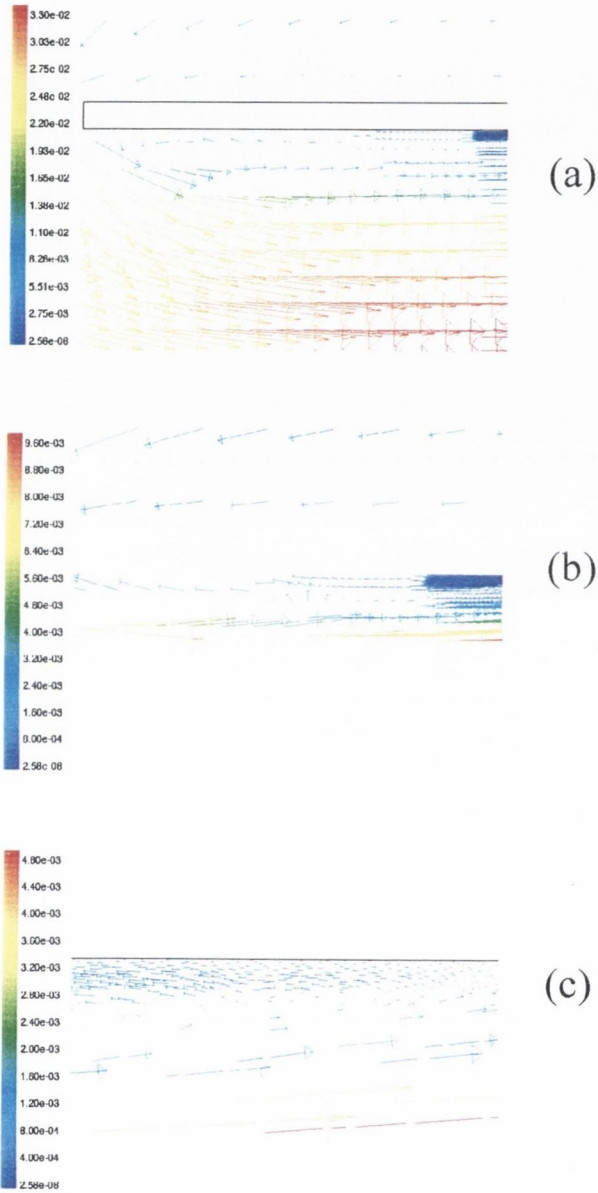


(a)

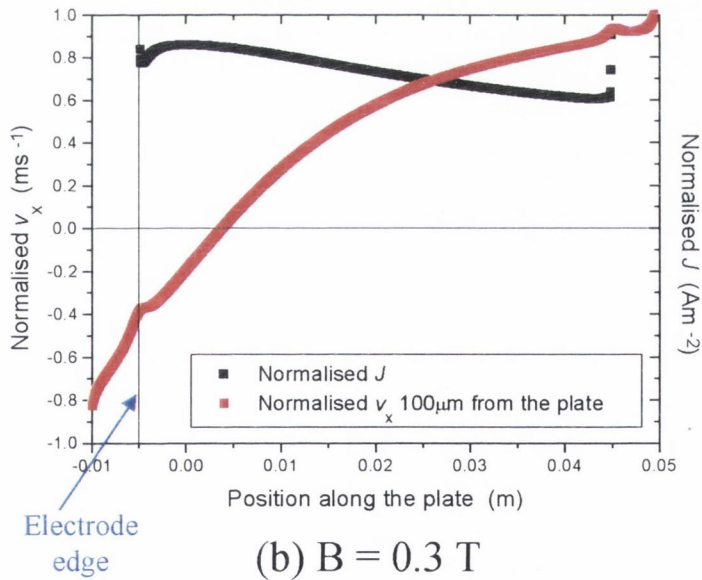
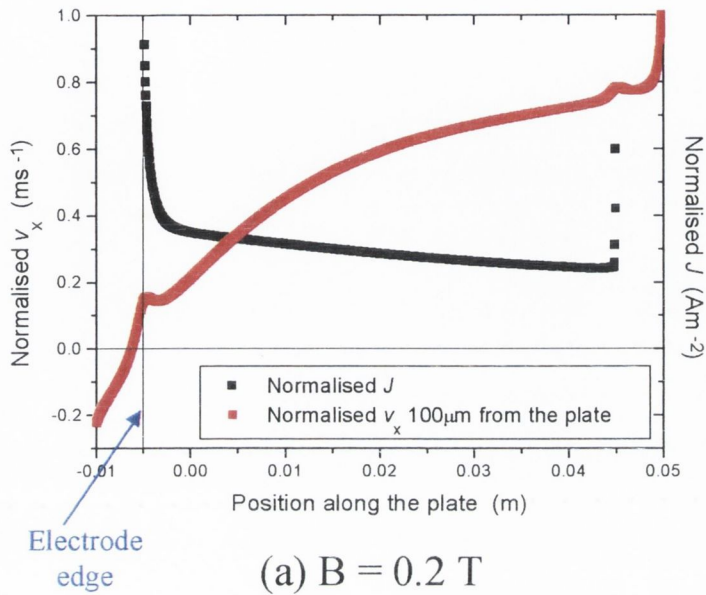


(b)

63. At  $B = 0.2$  T, an arrow plot reveals that (a) although the flow is in the positive  $x$ -direction in the bulk in the channel, at the mouth of the cell eddy-current behaviour is observed at the wall. The fluid actually moves in the *negative*  $x$ -direction at the wall. (b) zooms in on the electrode edge (which appears to the extreme right of (a)) showing that in this case the eddy current swirling does not extend to the electrode.



64. At  $B = 0.3$  T an arrow plot (a) of the velocity shows that the eddy swirling is again present inside at the inlet; (b) the eddies continue strongly into the region leading up to the electrode edge and (c) in this case they persist past the leading edge of the electrode.



65. The  $x$ -component of velocity ( $20 \mu\text{m}$  from the surface) along the plate length and the current density (normalised to  $j \times 10^{-6}$ ) along the electrode length are both plotted for (a)  $B = 0.2$  T and (b)  $B = 0.3$  T.

may lead one to believe that the  $j \propto B^{1/3}$  relationship yields a straight line graph through the origin. This, importantly, is not the case, as we must remember that current flows in the absence of any applied magnetic field. Thus there must exist some threshold below which the magnetic field induced convection is not sufficient to appreciably change the thickness of the diffusion layer. Magnetic field enhancement of the plating current should only be observed, therefore, above this threshold magnetic field value.

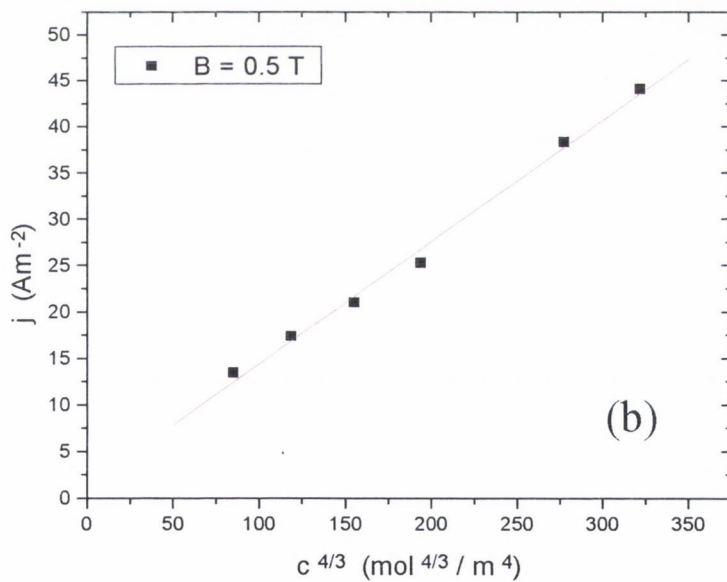
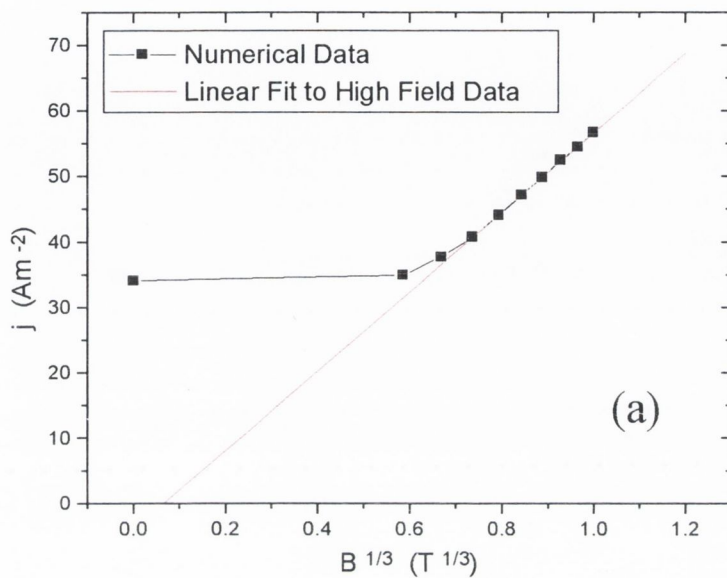
The dependence of the current density on the concentration of the ions in solution in the presence of a fixed magnetic field is shown in Fig.66(b). Here, for a constant value of  $B = 0.5$  T we see good agreement with the linear dependence of  $j$  on  $c_\infty^{4/3}$  predicted in Eq.4.70.

Combining the data of Figs.66(a) and (b) into Fig.68, we see that our numerical model has very closely reproduced the observed

$$j \propto c_\infty^{4/3} B^{1/3}$$

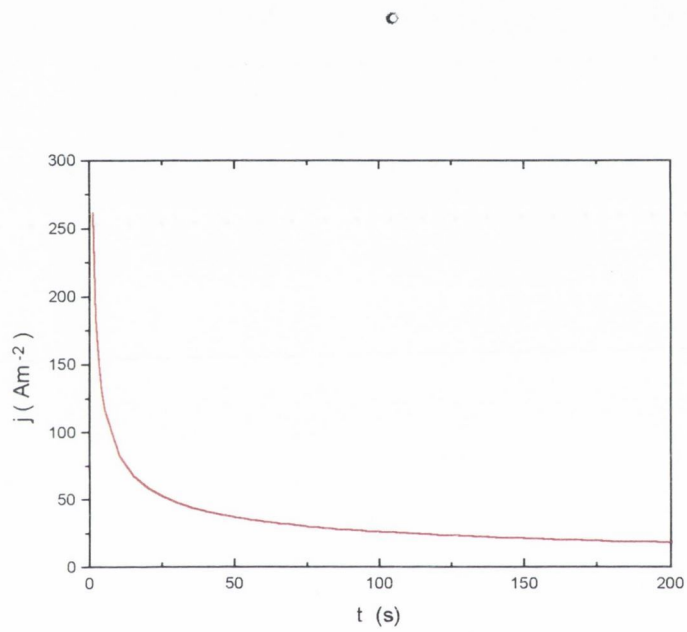
relationship over a range of values of concentration and applied magnetic field.

Fig.69 shows the comparison between our numerical data, the theoretical prediction of Aogaki from Eq.4.70 and 4.71 and his experimental results. Our simulation shows very good agreement with the theoretical values. The  $j \propto c_\infty^{4/3} B^{1/3}$  form of the experimental data is reproduced, although our absolute values are somewhat larger.

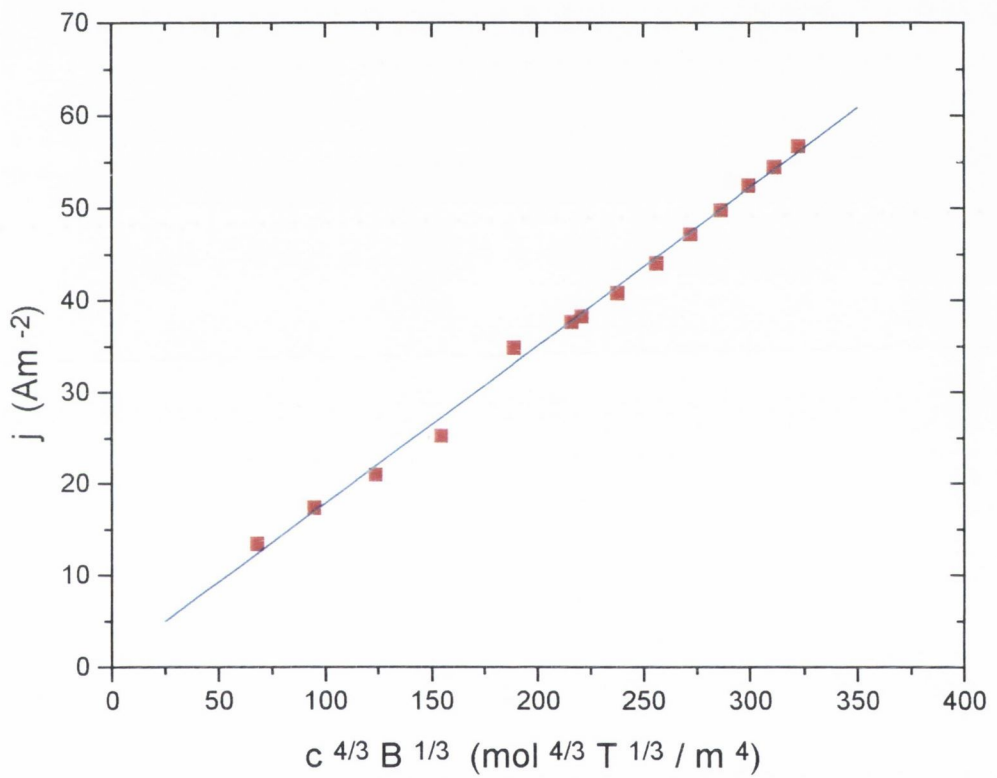


66. For concentration  $c_\infty = 76 \text{ mol/m}^{-3}$  (a) plots  $j$  against  $B^{1/3}$ . The straight line shows a linear fit to the higher field data, while the lower field value levels off to the zero field value. (b) plots  $j$  against  $c_\infty^{4/3}$  at a constant value of  $B = 0.5 \text{ T}$ . The straight line shows a linear fit to the data.

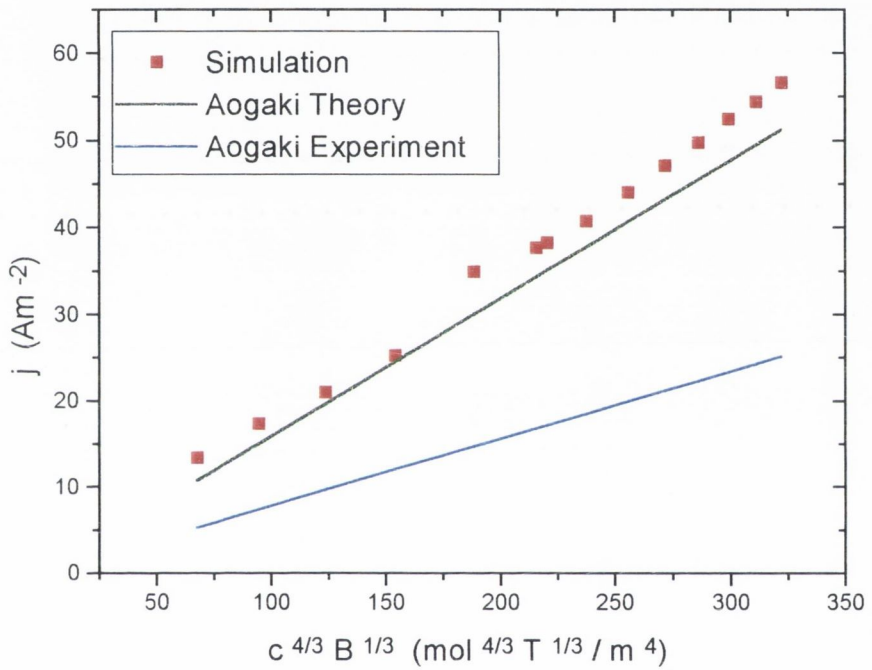




67. Variation of the zero-field limited diffusion current with time.



68. Plot of  $j$  against  $c^{4/3} B^{1/3}$  data shown together with a straight line fit.



69. Calculated  $j$  values are in very good agreement with the Aogaki analytical model and both are somewhat larger than the experimental data.

# Chapter 6

## Discussion

We have shown how the interplay between magnetic fields and electrodeposition results in a variety of phenomena which can be successfully modelled numerically. Very striking is the success of a rather simple DLA model in reproducing the fractal patterns observed when a magnetic field is applied perpendicular to a flat electrochemical cell. Good agreement with the experimental results is achieved for both linear and circular electrode geometries.

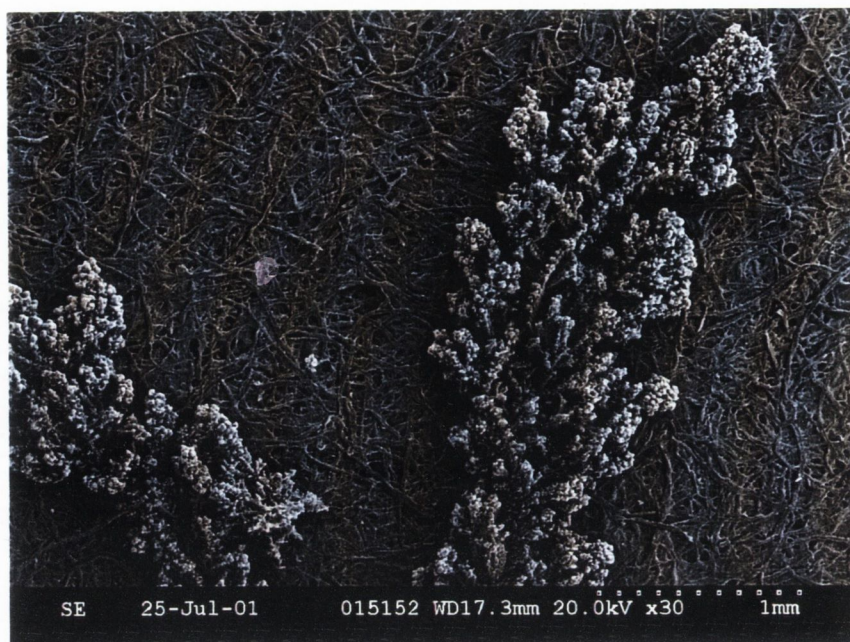
The very fact that any observable agreement is achieved between the experimental and modelled irregularities of the deposits, points to their fractal nature. As outlined in Section 1.1, one of the key properties of fractals is their scale-invariance, which means that their structure and the degree of their irregularity is similar at all scales. These simulations challenge that definition in attempting to relate our simulation to some length scale in the real problem.

One approach to defining a convenient length scale for our deposits, relates to the hydration spheres about the moving ions. Consider that each metal ion is, as outlined in Sec.1.5.1, surrounded by a sheath of water molecules, which extends to at least one hydration sphere of 6 water molecules. The real size of a moving ion is thus limited by the size of its hydration sphere. Given that one mole of  $\text{H}_2\text{O}$  occupies  $18 \times 10^{-6} \text{ m}^{-3}$ , then 6 water molecules occupy  $\sim 18 \times 10^{-29} \text{ m}^{-3}$ , and thus the hydration sphere has diameter  $\sim 0.7 \text{ nm}$ . Thus if we consider that in our simulation, two moving particles may not occupy

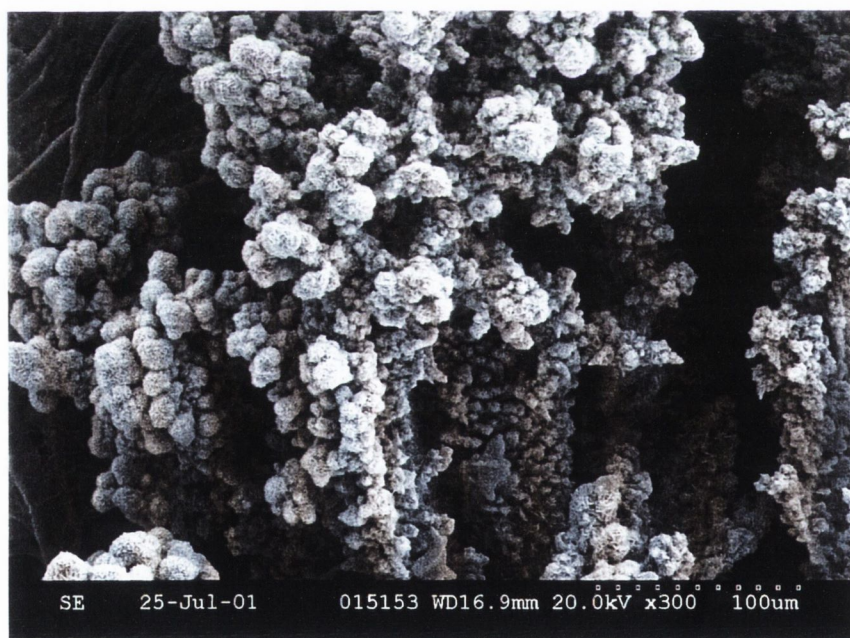
the same site, then we may set a length scale that the spacing between neighbouring sites  $\sim 0.7$  nm. Thus a numerical lattice of  $800 \times 800$  represents a fractal of width  $\sim 0.5$   $\mu\text{m}$ . Our box-counting log-log plots indicate self-similarity over two orders of magnitude, but given that the experimental electrodeposits have width  $\sim 0.01$  cm, the similarity between the experimental and numerical results indicates that these structures may be self-similar over a further 4 or 5 orders of magnitude. If this is the case, they may truly be considered to be fractal.

This hypothesis has probed in a recent examination of zinc electrodeposits in the electron microscope. This study confirms that the deposits are roughly self-similar from a scale of mm to  $\mu\text{m}$ . The original deposit was  $\sim 25$  mm in diameter, and their floral structure is maintained, Fig.70, over four orders of magnitude to the  $10$   $\mu\text{m}$  scale of Fig.71(a). On the  $1$   $\mu\text{m}$  scale of Fig.71(b), however, individual zinc crystallites with smooth surfaces are seen in the deposits. These crystallites are the elementary building blocks of the structure and set a limit to its fractal behaviour. The growth of such a crystallite is initiated by a nucleation process about which growth proceeds. Interpreting our simulations in the context of this data, a random walker sticking to the simulated electrodeposit may in some way be equivalent to the nucleation and growth of a single micron-sized crystallite. Such a nucleation and growth mechanism is also consistent with Fleury's SEM and AFM analysis of branched fractal electrodeposits [99], which points to polycrystalline growth developing out of oscillatory nucleation events.

With this in mind we consider the number of particles involved in a typical numerical aggregate compared to the number of ions reduced in a typical experiment. Experimen-

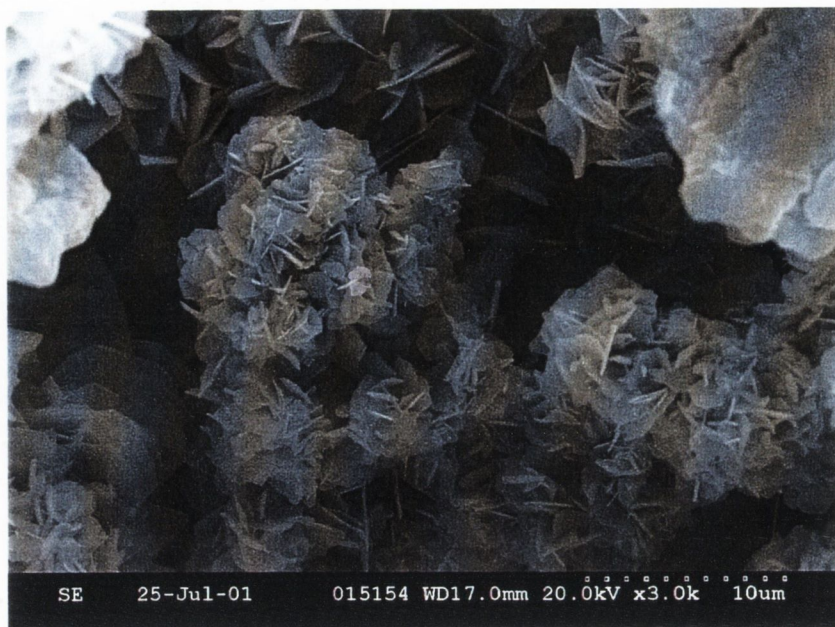


(a)

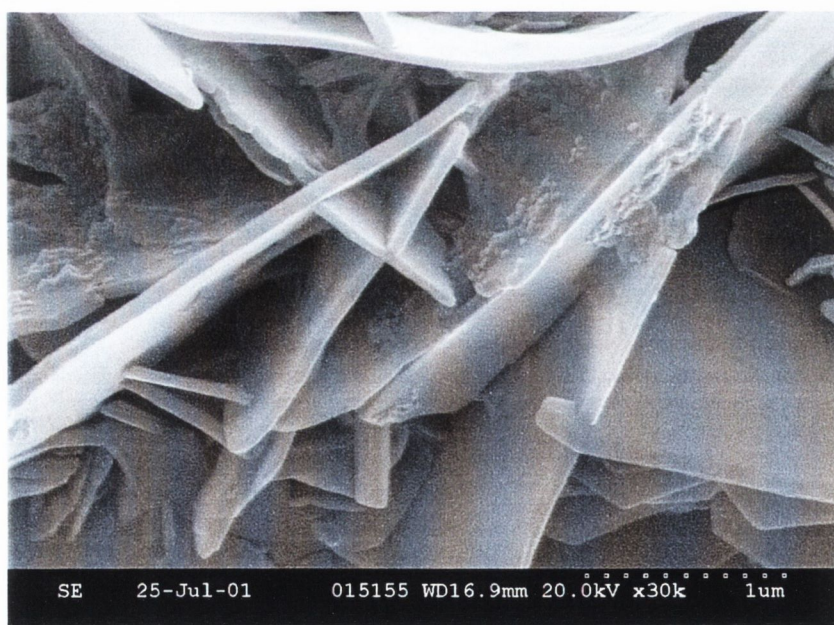


(b)

70. SEM images of a dense radial zinc electrodeposit at a scale of (a) 1 mm and (b) 100  $\mu\text{m}$ .



(a)



(b)

71. SEM images of the fractal of the zinc electrodeposit of the previous figure at a scale of (a)  $10\ \mu\text{m}$  and (b)  $1\ \mu\text{m}$ . The fractal structure breaks down and individual zinc crystals emerge on the  $1\ \mu\text{m}$  scale.

tal deposits such as those in Fig.14 contain  $\sim 10^{20}$  atoms, while the simulated fractals of Fig.38 contain only  $\sim 10^5$  atoms. This might suggest that the fractals really are self similar over at least 5 orders of magnitude, from a scale of mm to nm. Alternatively, as seems possible based on these SEM results, we may interpret the disparity between the number of experimental and numerical atoms as indicating that each atom in the simulation actually represent a cluster of  $\sim 10^{15}$  atoms. One must bear in mind, of course, that the experimental cell is not entirely two dimensional on the scale of the crystallites and does, of course, have some small thickness ( $\sim 200 \mu\text{m}$ ).

Such crystalline structure has also been observed by Grier et al [22] from transmission electron micrographs and x-ray diffraction, but only for dendritic deposits. In their study DLA-like aggregates displayed an amorphous structure, with rough, unfaceted tips evident on a scale of less than 30 nm. Thus the crystallographic and scaling properties of a deposit may depend on the conditions under which it is grown.

The problem of scale leads us to important questions regarding the scales over which the various effects in the model should be deemed to act. For example, the value of  $R_{look}$ , that radius about a particle within which the program scans for an occupied site on the deposit, is used repeatedly throughout the simulations. Firstly, as there is no supporting acidic electrolyte present in the fractal experiments, the migration force is long range, and falls off in two dimensions as  $1/d_{deposit}$  into the solution as shown in Section 2.1.2, where  $d_{deposit}$  is the distance from the ion to the nearest point on the aggregate. Although, in principle,  $d_{deposit}$  should be calculated for every particle at every step, this would prove very computationally costly. Furthermore, it is found numerically that the significance of



this  $1/d_{deposit}$  dependence is seen to saturate within  $d_{deposit} \sim 10$  sites. This results in our selection, in Section 3.1.1, of  $R_{look} = 10$  sites. Beyond  $R_{look}$  the effect of the applied electric field is simplified to a small, constant drift towards the deposit. So in this sense  $R_{look}$  may be taken to be the range over which migration is most significant. If we identify the site in the simulation with the dimensions of a crystallite in the deposit,  $R_{look} \sim 20 \mu\text{m}$ .

Numerically, we use the same value of  $R_{look}$ , however, when considering the effects of natural convection. Natural convection is induced by a density gradient between regions of ion-rich and ion-poor solution. As detailed in Section 1.5.5, in the vicinity of the electrode surface a concentration (density) gradient develops between the bulk solution with concentration  $c_\infty$  of metal ions, and the surface of the electrode where  $c_0 = 0$  as all the ions have been reduced to metal atoms. Natural convective flows develop as a result of this concentration gradient which exists within the diffusion layer which typically has thickness  $\delta_d \sim 100 \mu\text{m}$ . Although these flows conceivably develop to become larger scale effects in the case of the vertical cell, this is the scale on which they originate. Thus when we model natural convection within  $R_{look}$  of the deposit, we are effectively setting  $R_{look}$  within  $\delta_d$ . Alternatively one could argue that although we limit our simulation of natural convection to regions close to the surface, that this is really just the local effect of a larger scale convective flow.

Such an argument may be supported by the results from the numerical introduction of an applied magnetic field. Our first model for magnetic field considers the electrolyte effectively as a collection of ions, each of which experiences a force due to a magnetic field. In this case, although the Lorentz force  $\mathbf{F}_{Lor} = q\mathbf{v} \times \mathbf{B}$  is perpendicular to both  $\mathbf{v}$  and  $\mathbf{B}$ ,

the net effect will be to deflect the ion by some angle  $\alpha_{magn}$  to its ballistic trajectory along  $\mathbf{v}$ . The inadequacy of this model, however, was its failure to consider that  $\mathbf{B}$  is not acting on each ion in isolation, but on all of the ions in solution, so we must consider the cumulative effect of  $\mathbf{B}$  on  $\mathbf{j}$ . This results, not in a deflection of the motion of an individual particle, but in a bulk flow of the material with some velocity in a direction perpendicular to both  $\mathbf{B}$  and  $\mathbf{j}$ . Any such flow is confined by the ‘no-slip’ condition (Eq.1.30) to flow parallel to any solid surface in its path; that is it must flow parallel to the surface of the electrode. We limit our model, therefore, to considering the effect of this flow on particles close to the surface. That is not to imply, however, that the magnetic field necessarily acts only close to the electrode surface. Rather the assumption is that this Lorentz forced convective flow is everywhere in the cell perpendicular to both  $\mathbf{B}$  and  $\mathbf{j}$ , but that we can reduce computation time by considering its effects close to the surface only. In this sense, although  $R_{look}$  marks the limiting distance within which we consider this flow, it need not mark the limit of the flow itself.

This approach is also consistent with the electrokinetic theory of Olivier et al [51][53] who argue that the effect of the applied magnetic field is equivalent to inducing a non-electrostatic field parallel to the electrode surface, which pulls ions along the surface according to electrokinetic effects. Their theory (Section 1.6.2) does not prohibit bulk convective flow under a magnetic field, but instead argues that all effects can be accounted for by considering only local electrokinetic effects beyond the outer Helmholtz plane close to the electrode.

In these simulations, the ionic concentration is modelled simply by allowing many particles to move and stick simultaneously. It would be interesting, however, to extend the model to allow for a more complex concentration map about the fractal tips due to the local electric field [100] [101]. This could prove especially useful in a three-dimensional DLA simulation where gravitational convection close to the tips in the small third dimension is relevant [68].

The numerical data presented in this study considers only the effect of a magnetic field on the growth of fractals of non-magnetic metals. The deposition of magnetic materials, however, in an applied magnetic field results in quite different structures as shown by Bodea et al [35]. As a development of our numerical study, it might be interesting at some later stage to introduce a term for the force  $\mathbf{F} = -\nabla(\mathbf{m} \cdot \mathbf{B})$  on magnetic dipole moment  $\mathbf{m}$  of a magnetic ion due to the combination of the externally applied magnetic field and that magnetic field due to the fractal aggregate itself. It would also be interesting to determine the magnetisation curves of these magnetic fractal structures.

In the case of our magnetohydrodynamic simulations of current enhancement due to forced convection in the Aogaki cell, the agreement of the numerical result with experimental observations and theoretical predictions for

$$j \propto c_{\infty}^{4/3} B^{1/3}$$

is very satisfactory. A number of assumptions and simplifications are made, however, in building our numerical model.

In principle the electric and magnetic fields involved in these calculations should take the effective values inclusive of the secondary effects of induced Hall voltage due

to charged particles moving in a magnetic field, and the induced magnetic field due to the velocity of these charged particles. In practice, however, these secondary perturbations may be ignored [93][95] due to the small ionic carrier mobilities. By contrast, large electron mobilities make these secondary effects non-negligible in the case of liquid metal melts.

In our simulation we have considered only the diffusion current density in our calculation of  $j$ . As we are in the mass-transport limited regime (i.e. the region of a plot of current density against applied voltage where the reaction kinetics are very much faster than the rate of diffusion of material across the diffusion layer, and thus the current density is limited only by the speed of diffusion; in this region the current density is independent of increasing voltage), diffusion is the limiting process determining  $j$ . That is to say that migration of the ions under the applied electric field of Eq.1.18 is insignificant in determining the limiting current density. This is particularly valid given that the electrolyte in this system contains, as well as  $\text{CuSO}_4$ , a strong, acidic supporting electrolyte of  $1\text{M H}_2\text{SO}_4$  which screens the  $\text{Cu}^{2+}$  ions from the applied electric field. In the bulk solution it is these excess ions of the supporting electrolyte which carry the bulk of the current density. These ions draw the electrolyte towards the electrode by migration under a small potential gradient, diffusion not being relevant in the bulk as no concentration gradient exists here. Nonetheless, diffusion is the rate determining process and by continuity the value of the migrative current density in the bulk must equal that of the diffusion current density calculated at the surface.

Aleman et al [95][96] introduce a migration term into their magnetohydrodynamic simulations, on the grounds that, although migration does not affect the absolute value for

the limiting current, its effect far from the diffusion layer may affect the *distribution* of  $j$  in the bulk solution. In particular for a complex electrode geometry the electric field lines may not be exactly perpendicular to the electrode surface, but may bend somewhat out into the bulk. Accordingly, their expression for  $j$  is given by

$$\begin{aligned} \mathbf{j} &= -nFD\nabla c - \sigma\mathbf{E}^* \\ &= -nFD\nabla c - \sigma\nabla\Phi^* \end{aligned} \quad (6.75)$$

where the apparent electric field  $\mathbf{E}^*$ , due to the apparent potential  $\Phi^*$  is introduced such that the steady state conservation of current density (Eq.1.15) is satisfied.

As the geometry under consideration here consists of two, macroscopic, flat electrodes, however, the electric field lines between them deviate from linearity only close to the electrode edges. In the bulk of the fluid between the plates, therefore, our approximation of  $j(x, y) = j(x, 0)$  remains sufficient. For such a simple cell configuration, the addition of a migration term in the bulk serves only as a perturbation to the dominant diffusion current density. A more complicated geometry, however, involving a strongly non-linear distribution of electric field lines will require inclusion of the second term of Eq.6.75.

The results of Fig.66 for  $c = 76 \text{ mol m}^{-3}$  show a clear linearity between  $j$  and  $B^{1/3}$  for  $B \gtrsim 0.3 \text{ T}$ . Below this value, the results tend towards the value for limiting diffusion current density in the absence of an applied magnetic field. This important point emphasises the fact that only above some limiting value of magnetic field (for a given concentration and cell geometry) does the magnetic field generate a forced convective flow strong enough to affect the thickness of the diffusion layer, and thus the current density. So

it is important to note that this curve *does not* pass through the origin. Rather it levels out to the value of the limiting current density by natural convection.

The absolute values calculated for the current density are in very close agreement with the theoretical predictions of Aogaki in Eq.4.70. They are, however, somewhat larger than the experimental observation. This is most likely due to the fact that the zero gradient boundary conditions on the external walls of the numerical cell allow the electrolyte to flow faster than it would if fully confined by solid boundaries. This will tend to decrease the boundary layer thickness, and thus increase the current density.

It is very interesting, however, that such good agreement should exist with Aogaki's analytical model, as his model derives the relationship of Eq.4.70 on the assumption of smooth boundary layer flow past the electrode surfaces. On the contrary, however, we find that eddy currents caused by rapid flow past the leading edge of the channel wall can extend well beyond the electrode edge at high velocities. The result is that complex velocity, and thus concentration, profiles can exist at the electrode. Yet from Fig.68, our model reproduces the  $j \propto c_{\infty}^{4/3} B^{1/3}$  relationship predicted by Aogaki in both form and magnitude. We can understand this by dividing the electrode into two sections, the downstream section with flow in the normal, forward direction, and the upstream section with the back streaming flow. Within each section the flow is uniform and parallel to the surface. Thus Aogaki's model for the hydrodynamic flow effect on the diffusion layer profile may be applied to each section separately. The result is overall compliance with his theoretical prediction. Aogaki has elsewhere [102][103] proposed a theory for the effect of an applied magnetic field on dissolution at an electrode based on a theory of micro-vortices whose cumula-

tive effect is to produce a number of larger macro-vortices at the electrode surface. In this model, microscopic defects on the surface result in local currents which, under the Lorentz force, generate micro-vortices. Although our model does not consider such microscopic features of the system, there may ultimately prove to be a link between deposition through this kind of vortex flow and the reverse flow which we observe here.

Further numerical work in this area may prove very useful as a guide to improving industrial plating processes. In particular, if the uniformity of the thickness of the deposit is a key consideration, it may be desirable to eliminate the enhanced deposition at the electrode edge due to the current density spike in this region. MHD simulation could be used to develop a flow guide *geometry* that would produce a uniform hydrodynamic boundary layer thickness, and thus a uniform plating current over the length of the electrode. Conversely, such considerations could possibly be applied to enhance plating at a particular point of an electrode. Such boundary layer control has been attempted by Weier et al [104]. Magnetic field sources may be designed to tailor magnetic fields to a particular application. Permanent magnets prove particularly useful for such field confinement on a variety of scales.

# Chapter 7

## Conclusions

This thesis has presented the successful application of modelling techniques to two different aspects of magnetic field effects on electrodeposition, magnetic field effects on the growth of fractal electrodeposits, and magnetic field induced current density enhancement at a flat electrode. In both cases the resultant effects proved to be due to a Lorentz force acting on the ionic current.

Our enhanced random walker model for the magnetic field effect on fractal electrodeposition in flat electrochemical cells proved effective. The morphologies produced mirrored the experimentally observed spiral patterns closely for both circular and linear electrode geometries. An attempt at defining the minimum length scale for the numerical structures indicates that they represent agglomerates of crystallites about  $2 \mu\text{m}$  in size. The similarity in the resultant morphologies suggests very strongly fractal behaviour of fractal electrodeposits, over several orders of magnitude.

Numerical simulation of magnetohydrodynamic flow in an Aogaki cell yielded a linear dependence of  $j \propto c_{\infty}^{4/3} B^{1/3}$  as seen experimentally. The origin of this effect is in the flow of electrolyte caused by the Lorentz force acting on a current density  $j$  in a magnetic field  $B$ . This flow past the electrode has an effect similar to any other form of mechanical stirring in that it continuously replenishes the supply of plating ions to the electrode, thus enhancing the plating current density. The fact that the magnitudes of our calculated current densities were larger than the experimental values is primarily due to the fact that the



open boundary conditions on the ends of our cell allowed the electrolyte to flow faster than it would in a real system. The numerical values agreed very closely, however, with Aogaki's analytical prediction. This was somewhat surprising as Aogaki's theoretical model assumes smooth laminar flow over the flat electrode surfaces, when in fact our simulation reveals an area of reverse flow which, at high flow velocities, can stretch over the electrode surface. This may be understood by dividing the electrode into two regions, one with normal and one with backwards flow. Each satisfies Aogaki's laminar flow model, and thus the  $j \propto c_{\infty}^{4/3} B^{1/3}$  relationship holds overall.

There is significant scope to apply these numerical techniques to industrial processes to modify MHD flows so as to concentrate deposition in desired regions. Such refinement would require specialised magnetic field sources, of the kind analysed in the appendices, capable of concentrating flux into a confined space.

# Bibliography

1. B. Mandelbrot, "*The Fractal Geometry of Nature*", W.H. Freeman, 1983
2. "*Fractal Forms*", editors E. Guyon and H. E. Stanley, Elsevier, 1991.
3. P. Meakin, "*Fractals, Scaling and Growth far from Equilibrium*", Cambridge University Press, 1998.
4. L.M. Sander, "*Fractal Growth Processes*", Nature, 322, pp.789-793, 1986.
5. R. Jullien, "*Aggregation Phenomena and Fractal Aggregates*", Contemp. Phys., 28, pp.477-493, 1987.
6. L. Lam, "*Non-Linear Geometry for Beginners*", World Scientific, 1998.
7. B. Mandelbrot, "*How Long is the Coast of Britain*", Science, 155, pp.636-638, 1967.
8. P.G. DeGennes, "*Scaling Concepts in Polymer Physics*", Cornell University Press, 1979,
9. M.E. Cates, "*Brownian Dynamics of Self-Similar Macromolecules*", Journal de Physique, 46, pp.1123-1126, 1985.
10. D. S. McKenzie, "*Polymers and Scaling*", Physics Reports, C27, pp.35-88, 1976.
11. L.S.Schulmann, P.E. Seiden, "*Percolation and Galaxies*", Science, 233, pp.425-431, 1986
12. X. Luo and D.N. Schramm, "*Fractals and Cosmological Large Scale Structure*", Science, 256, pp.513-515, 1992
13. A. Linde, "*The Self-Reproducing Inflationary Universe*", Scientific American, November, pp.32-39, 1994
14. M. Batty, "*New Ways of Looking at Cities*", Nature, 377, pp.574, 1995.
15. M. Batty, "*Preliminary Evidence for a Theory of the Fractal City*", Environment and Planning A, 28, pp.1745-1762, 1996.

16. M. Batty, "*The Geography of Cyberspace*", Environment and Planning B, 20, 615-616, 1993.
17. E. E. Fournier d'Albe, "*Two New Worlds: I The Infra World; II The Supra World*", Longmans Green, London, 1907.
18. A. Hollingsworth, "*Storm Hunting with Fractals*", Nature, 319, 11-12, 1986.
19. C. Nicolis and G. Nicolis, "*Weather Forecasts Still Tricky*", Nature, 321, 567, 1986.
20. S. Lovejoy, D. Schertzer and P. Ladoy, "*Fractal Characterization of Inhomogeneous Geophysical Measuring Networks*", Nature, 319, 43-44, 1986.
21. M. Matsushita, M. Sano, Y. Hayakawa and Y. Sawada, "*Fractal Structures of Zinc Metal Leaves Grown by Electrodeposition*", Phys. Rev. Lett., 53, pp.286-289, 1984.
22. D. Grier, E. Ben-Jacob, R. Clarke and L.M. Sander, "*Morphology and Microstructure in Electrochemical Deposition of Zinc*", Phys. Rev. Lett., 56, pp.1264-1267, 1986.
23. D.G. Grier, D.A. Kessler and L.M. Sander, "*Stability of the Dense Radial Morphology in Diffusive Pattern Formation*", Phys. Rev. Lett., 59, pp.2315-2318, 1987.
24. Y. Sawada, A. Dougherty and J.P. Gollub, "*Dendritic and Fractal Patterns in Electrolytic Metal Deposits*", Phys. Rev. Lett., 56, pp.1260-1263, 1986.
25. G. Marshall, S. Tagtachian and L. Lam, "*Growth Pattern Formation in Copper Electrodeposition*", Chaos, Solitons and Fractals, 6, pp.325-339, 1995.
26. C. Leger, L. Servant, J.L. Bruneel and F. Argoul, "*Growth Patterns in Electrodeposition*", Physica A, 263, pp.305-314, 1999.
27. I. Mogi, M. Kamiko, S. Okubo and G. Kido, "*Pattern Formation of Electrodeposits of Zinc in Magnetic Fields*", Physica B, 201, pp.606-10, 1994.
28. I. Mogi and M. Kamiko, "*Striking Effects of Magnetic Field on the Growth Morphology of Electrochemical Deposits*", J. Crys. Growth, 166, pp.276, 1996.
29. I. Mogi, S. Okubo and Y. Nakagawa, "*Dense Growth of Silver Metal Leaves in a High Magnetic Field*", J. Phys. Soc. Jpn., 60, pp.3200, 1991.
30. I. Mogi, "*Electrochemical Studies in Steady High Magnetic Fields*", Physica B, 216, 396-398, 1996.

31. G. Hinds, J.M.D. Coey, "*Magneto-electrolysis of Copper*", J. Appl. Phys., 83, pp.6447-6449, 1998.
32. J.M.D. Coey, G. Hinds, M.E.G. Lyons, "*Magnetic Field Effects on Fractal Electrodeposits*", Europhys. Lett., 47, pp.267-272
33. G. Hinds, M.E.G. Lyons, T. Ní Mhíocháin and J.M.D. Coey, "*Magnetic Field Effects on Copper Electrodeposition and Electro-dissolution*", J. Phys. Chem., in press.
34. S. Nakabayashi, R. Aogaki, A. Karantonis, U. Iguchi, K. Ushida and M. Nawa, "*Two-dimensional Metal Deposition at a Liquid/Liquid Interface Potential and Magnetohydrodynamic Pattern Transition*", 473, 54-58, 1999.
35. S. Bodea, L. Vignon, R. Ballou and P. Mohlo, "*Electrochemical Growth of Iron Aborescences under In-Plane Magnetic Field: Morphology Symmetry Breaking*", Phys. Rev. Lett., 83, pp.2612-2615.
36. A. Imre, Z. Vertesy, T. Paykossy and L. Nyikos, "*Morphology of Cobalt Electrodeposits*", Fractals, 1, pp.59-66, 1993.
37. A.R. Imre and L. Balazs, "*Fractal Behaviour of Tree-like Nickel and Cobalt Electrodeposits*", Fractals, 8, pp.349-353, 2000.
37. G. Hinds, "*Magnetic Field Effects on Electrodeposition and Electro-dissolution of Copper*", Ph.D. Thesis, Trinity College Dublin, 2000.
39. A. Katsuki, S. Watanabe, R. Tokunaga and Y. Tanimoto, "*The Effects of High Magnetic Field on the Deposition of Silver*", Chem. Lett., 219-220, 1996.
40. Y. Tanimoto, A. Katsuki, H. Yano and S. Watanabe, "*Effect of High Magnetic Field on the Silver Deposition from its Aqueous Solution*", J. Phys. Chem., 101, 7359-7363, 1997.
41. A. Martin, T. Ní Mhíocháin, J.M.D. Coey, "*Numerical and Experimental Investigation of Magnetic Field Effects on Zinc Deposits Grown in a Linear Electrode Flat Cell Geometry*", in progress.
42. C. M. A. Brett and A.M. Oliveira Brett, "*Electrochemistry*", Oxford University Press, 1993.
43. J. Burgess, "*Metal Ions in Solution*", Ellis Horwood Limited, 1978.
44. C. H. Hamann, A. Hamnett, W. Vielstich, "*Electrochemistry*", Wiley-VCH, 1998.

45. D. R. Crow, "*Principles and Applications of Electrochemistry*", Stanley Thornes (Publishers) Ltd., 1998.
46. D. B. Hibbert, "*Introduction to Electrochemistry*", Macmillan Physical Science, 1993.
47. J. Koryta, J. Dvorák, V. Bohackova, "*Electrochemistry*", Methuen, London, 1970.
48. J. S. Newmann, "*Electrochemical Systems*", Prentice-Hall, 1973.
49. V.G. Levich, "*Physicochemical Hydrodynamics*", Prentice-Hall Inc., 1962.
50. Munson, Young and Okiishi, "*Fundamentals of Fluid Mechanics, 3rd Edition*", Wiley, 1998.
51. A. Olivier, J.P. Chopart, J. Amblard, E. Merienne and O. Aaboubi, "*Direct and Indirect Electrokinetic Effect Inducing a Forced Convection*", Models in Chemistry, 137, pp.213-224, 2000.
52. G. Hinds, J.M.D. Coey and M.E.G. Lyons, "*Influence of Magnetic Forces on Electrochemical Mass Transport*", Electrochem. Comm., 3, 215-218, 2001.
53. O. Devos, O. Aaboubi, J.-P. Chopart, E. Merienne, A. Olivier, C. Gabrielli and B. Tribollet, "*A New Experimental Device for Magnetochemical (M.E.C.) Transfer Function Measurements*", Polish J. Chem., 71, 1160-1170, 1997.
54. J.-P. Chopart, A. Olivier, E. Merienne, J. Amblard and O. Aaboubi, "*A New Experimental Device for Convective Mass-Transport Analysis by Electrokinetic-Hydrodynamic Effect*", Electrochemical and Solid-State Letters, 1, 139-141, 1998.
55. H. L. Frisch and J. M. Hammersley, "*Percolation Processes and Related Topics*", Journal of the Society of Ind. and Appl. Mathem., 11, pp.894-918, 1963.
56. S. R. Broadbent and J. M. Hammersley, "*Percolation processes. Crystals and Mazes.*", Proc. of the Cambridge Philosophical Society, 53, pp.629-641, 1957.
57. M. Plischke and Z. Racz "*Active Zone of Growing Clusters: Diffusion-limited Aggregation and the Eden Model*", Phys. Rev. Lett., 53, 415-418, 1984.
58. T. Williams and R. Bjercknes, "*Stochastic Model for Abnormal Clone Spread Through Epithelial Basal Layer*", Nature, 236, pp.19-21, 1972.
59. T.A. Witten and L. M. Sander, "*Diffusion Limited Aggregation: a kinetic critical phenomenon*", Phys. Rev. Lett., 47, pp.1400, 1981.

60. L. M. Sander, "Diffusion Limited Aggregation: a kinetic critical phenomenon?", *Comtemp. Phys.*, 41, 203-218, 2000.
61. L. Niemeyer, L. Pietronero, and H.J. Wiesmann, *Phys. Rev. Lett.*, 52, pp.1033, 1984.
62. W. W. Mullins and R. F. Sekerka, *Phys. Rev. B*, 27, 2586, (1963).
63. R. C. Ball and R. M. Brady, "Large Scale Lattice Effect in Diffusion-Limited Aggregation", *Journal of Physics A*, 18, L809-L813, 1985.
64. V.C. Noninski, "Magnetic Field Effect on Copper Electrodeposition in the Tafel Potential Region", *Electrochimica Acta*, 42, pp.251-254 1997.
65. J.-P. Chopart, J. Douglade. P. Fricoteaux and A. Olivier, "Electrodeposition and Electrodisolution of Copper with a Magnetic Field: Dynamic and Stationary Investigations", *Electrochimica Acta*, 36, pp.459-463, 1991.
66. O.Devos, O. Aaboubi, J.-P. Chopart, A. Olivier, C. Gabrielli and B. Tribollet, "Is there a Magnetic Field Effect on Electrochemical Kinetics?", *J. Phys. Chem. A*, 104, 1544-1548, 2000.
67. W. Huang and D. Brynn Hibbert, "Computer Modelling of Electrochemical growth with Convection and Migration in a Rectangular Cell", *Phys. Rev. E.*, 53, pp.727-730, 1996.
68. M. Rosso, J.-N. Chazalviel, V. Fleury and E. Chassaing, "Experimental Evidence for Gravity Induced Motion in the Vicinity of Ramified Electrodeposits", *Electrochimica Acta*, 39, pp.507-515, 1994.
69. H. Mizuseki, K. Tanaka, K. Ohno and Y. Kawazoe, "A New Crystal Growth Model Based on a Stochastic Method under an External Field", *Modelling Simul. Mater. Sci. Eng.*, 8, pp.1-11, 2000.
70. T.R. Ní Mhíocháin and J.M.D. Coey, "Numerical Simulation of Magnetic Field Effects on Fractal Electrodeposits with an Adapted Diffusion Aggregation Model", *Magneto-hydrodynamics*, 37, pp.169-176, 2001.
71. T.R. Ní Mhíocháin and J.M.D. Coey, "Adapted Diffusion Limited Aggregation Model for the Effects of Magnetic Fields on Fractal Electrodeposits", *J. Magn. and Mag. Mat.*, 226, pp.1281-1283, 2001.
72. J. Erlebacher, P.C. Searson and K. Sieradzki, "Computer Simulations of Dense-Branching Patterns", *Phys. Rev. Lett.*, 71, pp.3311-3314, 1993.

73. V. Fleury, M. Rosso, J.-N. Chazalviel and B. Sapoval, "*Experimental Aspects of Dense Morphology in Copper Electrodeposition*", Phys. Rev. A, 44, pp.6693-6705, 1991.
74. J.-N. Chazalviel, "*Electrochemical Aspects of the Generation of Ramified Metallic Electrodeposits*", Phys. Rev. A, 42, pp.7355-7367, 1990.
75. P. Meakin, "*Effects of Particle Drift on Diffusion-Limited Aggregation*", Phys. Rev. B, 28, 5221-5224, 1983.
76. H. Mizuseki, K. Tanaka, K. Kikuchi, K. Ohno and Y. Kawazoe, "*A New Model of DLA under High Magnetic Field*", Comp. Mat. Sci., 10, pp.46-50, 1998.
77. H. Mizuseki and Y. Kawazoe, "*Simulation of Electrochemical Deposition Process by a Multiparticle Diffusive Aggregation Model*", J. App. Phys., 87, pp.4611-4616, 2000.
78. E.L. Cussler "*Diffusion Mass Transfer in Fluid Systems*", Cambridge University Press, 1997.
79. C. Duchanoy, F. Lopicque, C.F. Oduoza, A.A. Wragg, "*Mass Transfer and Free Convection Associated with Electrodeposition at Long Narrow Upward Facing Tracks*", Electrochimica Acta, 46, pp.433-441, 2000.
80. E.J. Fenech and C.W. Tobias, "*Mass Transfer by Free Convection at Horizontal Electrodes*", Electrochimica Acta, 2, pp.311-325, 1960.
81. G.B. Thomas and R.L. Finney, "*Calculus and Analytic Geometry, 7th Edition*", Addison-Wesley, 1988.
82. K. Kim and T.Z. Fahidy, "*An Analysis of Free-Convective Magneto-electrolysis in Constant Magnetic Fields*", J. Electrochem. Soc., 142, pp.4196-4204, 1995.
83. W. Duan, H. Yano and Y. Tanimoto, "*Computer Simulation of Silver Deposition from its Aqueous Solution in High Gradient Magnetic Field*", Fractals, 6, 145-150, 1998.
84. T.Z. Fahidy, "*Magneto-electrolysis*", J. App. Electrochemistry, 13, 553-563, 1983.
85. R.A. Tacke and L.J.J. Janssen, "*Applications of Magneto-electrolysis*", J. App. Electrochemistry, 25, pp.1-5, 1995.
86. O. Aaboubi, J.P. Chopart, J. Douglade and A. Olivier, "*Magnetic Field Effects on Mass Transport*", J. Electrochem. Soc., 137, pp.1796-1804, 1990.

87. N. Leventis, M. Chen, X. Gao, M. Canallas and P. Zhang, "*Electrochemistry with Stationary Disk and Ring-Disk Millielectrodes in Magnetic Fields*", J. Phys. Chem. B, 102, 3512-3522, 1998.
88. N. Leventis and X. Gao, "*Steady-State Voltammetry with Stationary Disk Millielectrodes in Magnetic Fields: Nonlinear Dependence of the Mass-Transfer Limited Current on the Electron Balance of the Faradaic Process*", J. Phys. Chem. B, 103, 5832-5840, 1999.
89. J. Lee, S.R. Ragsdale, X. Gao and H.S. White, "*Magnetic Field Control of the Potential Distribution and Current at Microdisk Electrodes*", J. Electroanal. Chem., 422, 169-177, 1997.
90. S.R. Ragsdale, J. Lee, and H.S. White, "*Analysis of the Magnetic Force Generated at a Hemispherical Microelectrode*", Anal. Chem. 69, 2070-2076, 1997.
91. S.R. Ragsdale, K.M. Grant, and H.S. White, "*Electrochemically Generated Magnetic Forces, Enhanced Transport of a Paramagnetic Redox Species in Large, Nonuniform Magnetic Fields*", J. Am. Chem. Soc., 120, 13461-13468, 1998.
92. R. Aogaki, K. Fueki and T. Mukaibo, "*Diffusion Process in Viscous Flow of Electrolyte Solution in Magnetohydrodynamic Pump Electrodes*", Denki Kagaku, 2, pp.89-94, 1976.
93. R. Aogaki, K. Fueki and T. Mukaibo, "*Application of the Magnetohydrodynamic Effect to the Analysis of Electrochemical Reactions - 1. MHD Flow of an Electrolyte Solution in an Electrode Cell with a Short Rectangular Channel*", Denki Kagaku, 43, pp.504-508, 1975.
94. R. Aogaki, K. Fueki and T. Mukaibo, "*Application of the Magnetohydrodynamic Effect to the Analysis of Electrochemical Reactions - 2. Diffusion Process in MHD Forced Flow of Electrolyte Solutions*", Denki Kagaku, 43, pp.509-514, 1975.
95. G.B. Ngo Boum and A. Alemany, "*Numerical Simulations of Electrochemical Mass Transfer in Electromagnetically Forced Channel Flows*", Electrochimica Acta, 44, 1749-1760, 1999.
96. G.B. Ngo Boum, S. Martemianov, A. Alemany, "*Computational Study of Laminar Flow and Mass Transfer around a Surface-Mounted Obstacle*", Int. J. Heat and Mass Transfer, 42, pp.2849-2861, 1999.



97. G.B. Ngo Boum, "*Étude Numérique du Transport de Matière au sein d'un Electrolyte: Effet d'un Champ Magnétique*", Ph.D. Thesis, l'Institut national Polytechnique de Grenoble, 1998.
98. K. Kim and T.Z Fahidy, "*On the Numerical Solution of an Electrolytic Convective-Diffusion Problem in an Externally Imposed Force Field*", Chem. Eng. Journal, 68, 69-72, 1997.
99. V. Fleury, "*Branched Fractal Patterns in Non-Equilibrium Electrochemical Deposition from Oscillatory Nucleation and Growth*", Nature, 390, pp.145-148, 1997.
100. V. Fleury, J.-N. Chazalviel and M. Rosso, "*Theory and Experimental Evidence of Electroconvection around Electrochemical Deposits*", Phys. Rev. Lett., 68, pp.2492-2495, 1992.
101. V. Fleury, J.H. Kaufman and D.B. Hibbert, "*Mechanism of a Morphology Transition in Ramified Electrochemical Growth*", Nature, 367, pp.435-438.
102. R. Aogaki, A. Tadano and K. Shinohara, "*The Micro-MHD Effect on Electrodeposition*", Proceedings of the 4th Symposium on New Magneto-Science, pp.27-46, 2000.
103. K. Shinohara and R. Aogaki, "*Magnetic Field Effect on Copper Corrosion in Nitric Acid*", Electrochemistry, 67, 126-131, 1999.
104. T. Weier, U. Fey, G. Gerbeth, G. Mutschke, O. Lielausis and E. Platacis, "*Boundary Layer Control by Means of Wall Parallel Lorentz Forces*", Magnetohydrodynamics, 2001 (in press).
105. T.R. Ní Mhíocháin, D. Weaire, S.M. McMurry and J.M.D. Coey, "*Analysis of Torque in Nested Magnetic Cylinders*", J. App. Phys., 86, pp.6412-6424, 1999.
106. T.R. Ní Mhíocháin, J.M.D. Coey, D. Weaire and S.M. McMurry, "*Torque in Nested Halbach Cylinders*", IEEE Trans. Magn., 35, pp.3968-3970, 1999.
107. H.A. Leupold, E. Potenziani II, "*Applications of Yokeless Flux Confinement*", J. Appl. Phys. 64, 5994 (1988).
108. H. A. Leupold in "*Rare Earth Iron Permanent Magnets*", Chap. 8, J. M. D. Coey (editor), Oxford University Press (1996).
109. K. Halbach, "*Design of Permanent Multipole Magnet with Oriented Rare Earth Cobalt Magnet*", Nucl. Inst. Meth., 169, 1, (1980).

110. Permanent magnet flux sources are available from Magnetic Solutions Ltd., IDA Centre, Unit 13, Pearse St., Dublin 2, Ireland.
111. T. Kenjo, "*Electric Motors and their Controls : an Introduction*", Oxford University Press, 1991.
112. A. Aharoni, "*Introduction to the Theory of Ferromagnetism*", Oxford University Press (1996).
113. J. P. Yonnet in "*Rare Earth Iron Permanent Magnets*", Chap. 9, J. M. D. Coey (editor), Oxford University Press (1996).
114. G. Akoun, J.P Yonnet, IEEE Trans. Magn., 20, 1962, (1984).

# Publications

- T.R. Ní Mhíocháin, D. Weaire, S.M. McMurry and J.M.D. Coey, “*Analysis of Torque in Nested Magnetic Cylinders*”, J. Appl. Phys., 86, pp.6412-6424, 1999.
- T.R. Ní Mhíocháin, J.M.D. Coey, D. Weaire and S.M. McMurry, “*Torque in Nested Halbach Cylinders*”, IEEE Trans. Magn., 35, pp.3968-3970, 1999.
- T.R. Ní Mhíocháin and J.M.D. Coey, “*Numerical Simulation of Magnetic Field Effects on Fractal Electrodeposits with an Adapted Diffusion Aggregation Model*”, Magnetohydrodynamics, 37, pp.169-176, 2001, also published in Proceedings of the Fourth International Pamir Conference, ‘*Magnetohydrodynamics at the Dawn of the Third Millenium*’, vol. 1, pp. 375-380, 2000.
- T.R. Ní Mhíocháin and J.M.D. Coey, “*Adapted Diffusion Limited Aggregation Model for the Effects of Magnetic Fields on Fractal Electrodeposits*”, J. Magn. and Mag. Mat., 226, pp.1281-1283, 2001.
- G. Hinds, F. E. Spada, J.M.D. Coey, T.R. Ní Mhíocháin and M.E.G. Lyons, “*Magnetic Field Effects on Copper Electrolysis*”, J. Phys. Chem. B, 105, pp.9487-9502, 2001.
- J.M.D. Coey, G. Hinds, C. O’Reilly and T.R. Ní Mhíocháin, “*Magnetic Field Effects on Electrodeposition*”, Material Science Forum, vols 373-376, pp. 1-8, 2001.

- T.R. Ní Mhíocháin and J.M.D. Coey, “*Generation of Magnetic Fields with Permanent Magnets*”, in ‘High Magnetic Fields, Techniques and Experiments’, vol. 1, editor Fritz Herlach, in press.
- T.R. Ní Mhíocháin and J.M.D. Coey, “*Permanent Magnets*”, in the Encyclopedia of Life Support Systems, EOLSS Publishers Co. Ltd., in press.
- J.M.D. Coey and T.R. Ní Mhíocháin, “*Permanent Magnet Assemblies*”, in the ‘Encyclopedia of Materials: Science and Technology’, Elsevier, in press 2001.

# Appendix A

## Analysis of Torque in Nested Halbach Cylinders

Rotatable nested cylindrical magnets may be used to generate variable magnetic fields. A mutual torque exists between the cylinders which is an important consideration in practical designs. We present a thorough investigation of this torque, combining experiment, computation and theory. In the finite length case, in which the magnetisation varies according to the prescription of Halbach, the torque is an end effect. It is proportional to  $\sin\alpha$ , where  $\alpha$  is the angle defining the relative orientation of the cylinders. Practical designs use a discrete number  $N$  of permanent magnet segments to approximate the continuously varying magnetisation of the ideal design. These introduce higher components  $\sin(n\alpha)$  to the angular dependence of torque, where the allowed values of  $n$  are restricted to  $n = (kN \pm 1)$  according to the Segmented Magnet Torque Theorem.

### A.1 Introduction

Permanent magnet variable flux sources have some appealing advantages over conventional electromagnets. They are compact, and require no cooling or external power supply. Long permanent magnet cylinders, known as Halbach cylinders or dipole rings, create a magnetic field in their bore which is uniform to a very good approximation. Two such cylinders can be coaxially nested and rotated about their common axis to create a variable field as described by Leupold [107].

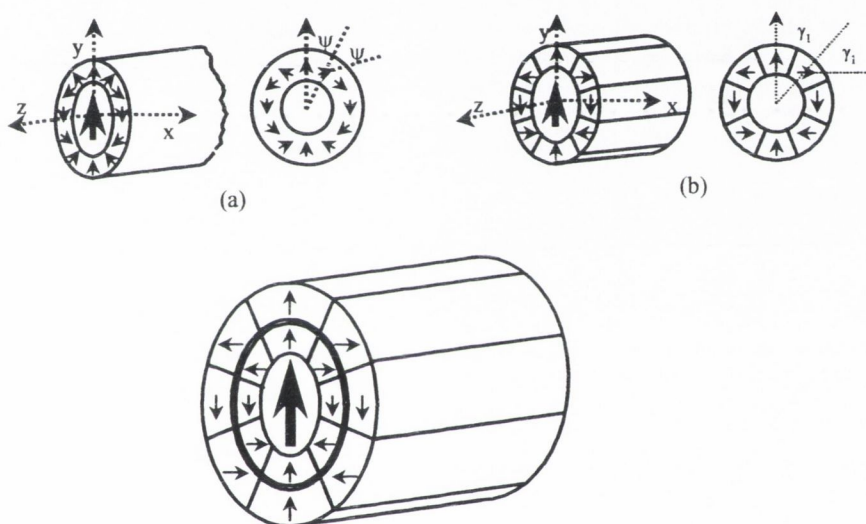
Among the issues encountered in the design of such devices, there is the problem of mutual torque between the two cylinders. The torque is exactly zero in the idealised model of infinitely long cylinders with continuously varying orientation of the magnetisation. Thus its origins and magnitude in real systems have not been apparent.

Here an experimental, numerical and theoretical analysis of the torque as a function of the relative angle between the cylinders is presented. Principles of symmetry are applied, and a theorem is proved concerning the functional form of the energy and torque. An analytical theory emerges which is confirmed and complemented by numerical simulations. There remain to be resolved some minor discrepancies with experimental observations, but the present level of understanding provides a valuable design tool.

The design of an ideal Halbach cylinder is indicated in Fig.72(a). The axis of the cylinder is the  $z$ -axis, and the magnetisation lies in the plane perpendicular to  $z$ . The magnitude of the magnetisation is constant, while its orientation varies continuously: at an angular position  $\psi$  measured clockwise from the  $y$ -axis the magnetisation has orientation  $2\psi$  as shown in the figure. A cylinder with continuously varying magnetisation direction will be termed an ‘ideal Halbach’ cylinder. An infinitely long ideal Halbach cylinder produces a uniform magnetic field in the  $y$ -direction within the bore, and zero field everywhere outside the cylinder. The magnitude of the induction  $B$  in the bore [108] is

$$B = B_r \ln \left( \frac{R_o}{R_i} \right) \quad (\text{A.1})$$

where  $B_r$  is the remanence of the material, and  $R_o$ ,  $R_i$  are the outer and inner radii of the cylinder respectively.



72.(a) The ideal infinite length dipole ring, with definition of angular variables; (b) The finite length, segmented Halbach approximation, with definition of angular variables; (c) Two nested cylinders; the field in the bore is the vector sum of the fields from the individual cylinders.

Fig.72(b) presents a practical approximation to this design, as suggested by Halbach [109]. A discrete number  $N$  of uniformly magnetised segments is used to approximate the uniformly varying magnetisation of the ideal design. The direction of the magnetisation in any segment is constant and given by twice the angular position  $\psi = \gamma_j$  of the centre of the segment, where  $\gamma_j = j2\pi/N$  for  $j = 1, 2, \dots, N$ . We refer to this design as the ‘segmented cylinder’. Inhomogeneities in the field within the bore and some stray field outside the cylinder result from the segmented structure and finite length of such a magnet.

A pair of coaxially nested cylinders, one inside the bore of the other, is shown in Fig.72(c). Such a pair can generate magnetic fields which are continuously variable in both magnitude and direction, as suggested in reference [107]. The resultant field in the central bore is the vector sum of fields from the individual cylinders. By rotating the cylinders with respect to each other, the magnitude and orientation of the central field can be uniformly varied. If the dimensions of the cylinders are chosen such that the same bore field is produced by each cylinder alone, then the magnitude of the resultant field of the pair can range from zero to twice that of a single cylinder.

Commercial cylinders are constructed using rare-earth magnet materials such as Nd-Fe-B. These materials have very square hysteresis loops with a high coercivity ( $\mu_0 H_c > 1.5$  T) and small transverse susceptibility ( $\chi_{\perp} \approx 0.1$ ), so that the magnetisation pattern of the cylinders is essentially unaffected by the large fields to which it is exposed [108]. Thus in theoretical calculations of the field due to such a cylinder it is a fair approximation to take the susceptibility in any direction to be zero.



In a typical device [110], two cylinders are independently rotated by motors which drive them to the positions necessary to produce a given field. A variable torque is experienced as one cylinder is rotated relative to the other. Torque places strain on the gears and motors turning the cylinders, and can contribute significantly to their wear and tear. Hence, it is important to have a greater understanding of its origins.

We have investigated this torque experimentally (Section A.2), using computer modelling (Section A.4) and analytically (Section A.5). In Section A.3 we present the background theory necessary for our analysis. We show that torque is absent for infinitely long ideal cylinders, and results from field non-uniformities in nested segmented cylinders of finite length.

The energy  $dE$  of a small element of magnetic material with volume  $dV$  and uniform polarisation  $J$ , placed in an external magnetic field  $H_{app}$ , is given by

$$dE = -J \cdot H_{app}dV \quad (\text{A.2})$$

where  $J$  is related to magnetisation  $M$  by  $J = \mu_0 M$ . For these rigid magnets the polarisation is equal to the remanence  $J = B_r$ .

The element experiences a torque  $d\Gamma_m$ , tending to align  $J$  with  $H_{app}$ , given by

$$d\Gamma_m = J \times H_{app}dV \quad (\text{A.3})$$

and a torque  $d\Gamma_f$  about a fixed origin

$$d\Gamma_f = r \times F \quad (\text{A.4})$$

where  $r$  gives the position of the element relative to the origin.

$$F = -\nabla(dE) = \nabla(J \cdot H_{app}) dV \quad (\text{A.5})$$

is the force on the element due to the gradient of the applied field, in the case where  $J$  is constant over the volume  $dV$ .

In the case of concentric cylinders, and as a result of the reciprocity theorem given in section A.3.1, the torque on the system may be calculated by considering the rotation of either cylinder about its axis in the field due to the other cylinder which is kept stationary. The total torque  $\Gamma$  consists of contributions  $d\Gamma_m$  and  $d\Gamma_f$  (Eqs.A.3 and A.4) integrated over the volume of the first cylinder. The  $i$ -th component of the torque is given by

$$\Gamma_i = \int_V \left\{ (J \times H_{app})_i + \sum_{jkl} \varepsilon_{ijk} r_j J_l (\nabla_k (H_{app}))_l \right\} dV. \quad (\text{A.6})$$

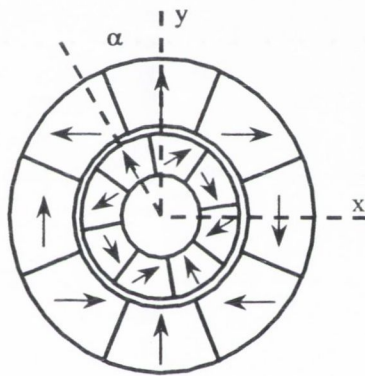
The torque and the energy are related by

$$\Gamma = -\frac{dE}{d\alpha} \quad (\text{A.7})$$

where  $\alpha$  is the angle of rotation of the inner cylinder relative to the outer, as shown in Fig.73, and  $E$  is the energy of one cylinder in the field of the other.

## A.2 Experimental Results

We measured the variation in torque as a function of  $\alpha$  for a nested two-cylinder system, where  $\alpha$  is the angle through which the inner cylinder is rotated from the position where its magnetisation is fully aligned with that of the outer, from Fig.73. Both cylinders were made of segments of Nd-Fe-B. The cylinder dimensions are given in the table.



73. Graphical definition of the relative angular rotation  $\alpha$  between the cylinders when the outer cylinder is kept in a fixed position.

	<i>Inner Cylinder</i>	<i>OuterCylinder</i>
Inner Radius (mm)	26	52.5
Outer Radius (mm)	47.5	110
Length (mm)	100	100
Segment Number $N$	8	8
Nominal Value for Remanence (T)	1.08	1.17

Table A1 : Cylinder characteristics.

Each cylinder was connected, via a system of gears, to a d.c. motor [111]. The position of each cylinder at any instant was recorded via an absolute encoder.

The torque  $\Gamma_{mot}$  generated by the d.c. motor is directly proportional to  $I$ , the current drawn,

$$\Gamma_{mot} = k_T I \quad (\text{A.8})$$

where  $k_T$  is the torque constant given by

$$k_T = \frac{(V - IR)}{\omega_m}. \quad (\text{A.9})$$

Here  $V$  is the operating voltage,  $R$  is the resistance at the motor terminals and  $\omega_m$  is the angular speed of the rotor in (radian/s). This equation is obtained by equating the power input to the motor,  $P_i = VI$ , to the total output power  $P_o$  generated by the motor.  $P_o$  is the sum of the power associated with the torque,  $\Gamma_{mot}\omega_m$ , and the power loss,  $RI^2$ .

If the motor is run at constant voltage, the torque generated by the motor at any instant can be calculated by monitoring the variations in current drawn and motor speed. This can then be related to the torque experienced by the cylinder via the gear ratios. The gearing system comprised a planetary gearbox, and a worm-wheel unit.

In the measurements reported below, the outer cylinder was held in a fixed position while the inner cylinder was rotated. The inner motor was run at a constant voltage of 12 V.

The current, inner encoder position and voltage were recorded at regular time intervals, and the angular speed  $\omega_c$  of rotation of the cylinder at each of these instants was determined.

The angular speed  $\omega_m$  of the motor was found from

$$\omega_m = \omega_c r_{gb} \frac{n_{teeth}}{n_{start}} \quad (\text{A.10})$$

where  $r_{gb}$  is the gearbox ratio,  $n_{teeth}$  is the number of teeth in the worm-wheel, and  $n_{start}$  is the number of starting teeth in the worm screw.

From these data, the torque  $\Gamma_{mot}$  generated by the motor was calculated at each instant using Eqs.A.8 and A.9. This yielded the torque  $\Gamma$  experienced by the cylinder:

$$\Gamma = \Gamma_{mot} r_{gb} \left( \frac{n_{teeth}}{n_{start}} \right) \eta_m \eta_{ww} \eta_{gb}$$

where  $\eta_m$ ,  $\eta_{ww}$  and  $\eta_{gb}$  are the efficiencies of the motor, worm-wheel and gearbox respectively.

The cylinder torque for a constant applied voltage of 12 V is plotted in Fig.74(a) as a function of the relative orientation  $\alpha$  for two complete rotations of the inner cylinder, and the current and angular velocity of the cylinder are plotted in Fig.74(b). In this case the cylinder was rotating in the clockwise direction, so that  $\alpha$  is negative. As will be explained more fully later, the variation in torque around one full rotation of the cylinder is essentially sinusoidal. For one half of each cycle, the motor is working to overcome the magnetic torque. In this region, an increase in load torque is reflected by an increase in the current drawn by the motor, and a decrease in the speed of the motor head and vice versa. For the second half of each cycle, both the motor and the magnetic torque rotate the cylinder in the same direction, so there is effectively zero load torque on the motor. The current drawn

by the motor is reduced and its speed increased. However, the maximum (no load) speed,  $n_0$ , and the minimum (no load) current,  $I_0$ , are determined by the applied voltage and the terminal resistance of the motor, and their values are defined for a given motor. In this case  $n_0 = 4090$  rpm, and  $I_0 = 12.3$  mA. Hence, in this region of the graph, both current and speed remain approximately constant.

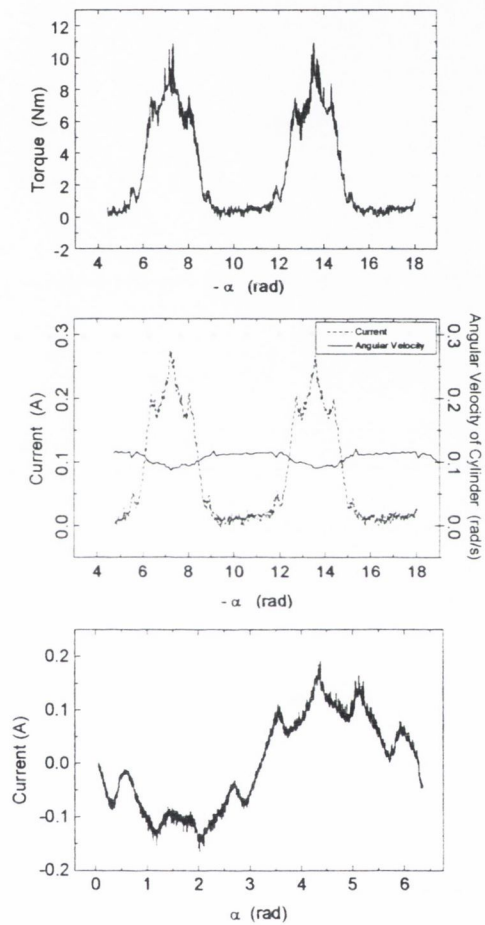
Fig.74(b) shows variation in current  $I$  for two complete clockwise rotations. Similar data were collected for rotation in the anticlockwise sense. These two sets of data were combined to indicate the structure of the torque variation over 360 degree cycles. The combined data for one complete rotation are shown in Fig.74(c).

These measurements were repeated for constant voltages of 6 V, 8 V and 10 V, and also while rotating the inner cylinder at four different values of constant speed and allowing the voltage to vary. Each of these cases yielded results consistent with those presented above.

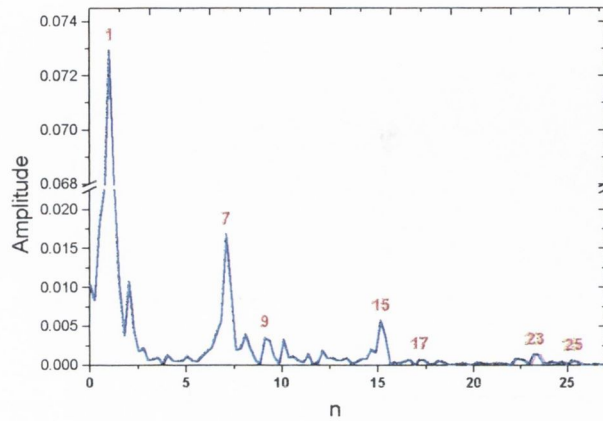
The variation of the current as a function of  $\alpha$  may be written as a Fourier series

$$I(\alpha) = \sum_{n=1}^{\infty} (a_n \cos(n\alpha) + b_n \sin(n\alpha)) \quad (\text{A.11})$$

A Fourier transform of the current data is shown in Fig.75, plotting the amplitude of the current,  $\sqrt{a_n^2 + b_n^2}$ , as a function of the order,  $n$ , of the term. The dominant term is evident at  $n = 1$ , indicating that the variation is mainly sinusoidal. Higher order terms are also evident, in particular at  $n = 7, 15$  and  $23$ , each with a smaller neighbouring peak around  $n = 9, 17$  and  $25$  respectively. That is, higher order terms are significant at  $n = (kN \pm 1)$ , where  $N$  is the number of segments on the cylinder and  $k$  is an integer.



74.(a) Torque on the inner cylinder over two full clockwise rotations; (b) Current drawn by inner cylinder motor and cylinder angular velocity for two clockwise rotations; (c) Current data from clockwise and anticlockwise rotations combined to give complete information over one complete rotation.



75. Amplitude of Fourier components of data in the previous figure, showing a dominant peak at the  $n = 1$  term of the Fourier series, with successive peaks at the  $n = (kN \pm 1)$  terms as labelled, where  $N = 8$  is the number of segments and  $k$  is an integer.

These terms in the torque variation are modelled numerically and accounted for analytically in the following sections.

### A.3 The Model

The numerical and analytical calculations which we present depend on the following: (i) the Reciprocity Theorem which allows us to find the torque by calculating the energy of the inner cylinder in the field of the outer;

(ii) the rigidity of the polarisation in the high remanence, high coercivity materials used to construct the cylinders. This allows us to use a magnetic charge model for our



field calculations, and in particular a surface charge model for calculating the field due to a segmented cylinder (Section A.4.1);

(iii) the symmetry properties of the cylinders which lead to the ‘Segmented Magnet Torque Theorem’ (Section A.5.2) concerning the angular dependence of the torque.

### A.3.1 Reciprocity

The Reciprocity Theorem [112] for magnetostatic energy, states that the energy,  $E$ , of one magnet due to the field of a second is equal to the energy of the second due to the field of the first. That is,

$$E = \int_{all\ space} H_1 \cdot J_2 dV = \int_{all\ space} H_2 \cdot J_1 dV \quad (\text{A.12})$$

where  $H_i$  is the magnetic field produced by magnet with polarisation  $J_i$ , where  $i = 1, 2$ . The inner and outer cylinders must experience equal and opposite torques which may be calculated from the energy using Eq.A.7. In our nested model we choose to calculate the torque by considering the effect on the inner cylinder of the field due to the outer one.

### A.3.2 Magnetic Charge Model

As the first step in the simulation, we calculate the field due to the outer cylinder alone (Section A.4.1). The model depends on the assumption, which is an adequate approximation for the real cylinders, that each segment has a perfectly rigid polarisation  $J$ . The magnetic induction within a block of magnetic material is

$$B = \mu_0 H + J \quad (\text{A.13})$$

In a magnetostatic system,

$$\nabla \times H = 0 \quad (\text{A.14})$$

so we may define a scalar potential  $\varphi_m$  by

$$H = -\nabla\varphi_m. \quad (\text{A.15})$$

Since  $\nabla \cdot B = 0$ , then from Eq.A.12

$$\nabla \cdot H = -\nabla^2\varphi_m = \frac{-\nabla \cdot J}{\mu_0} \quad (\text{A.16})$$

and  $\varphi_m$  satisfies a Poisson equation with magnetic charge density  $\rho_m = -\nabla \cdot J$ .

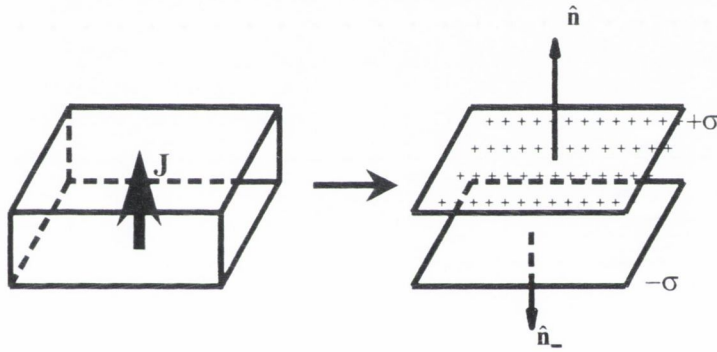
In the ideal case, the field is calculated from a non-zero volume charge density, as in appendix B. In the case of a segmented cylinder, however, each segment has uniform and perfectly rigid  $J$ . Thus the volume magnetic charge density  $\rho_m$  in each segment is zero. In this case the magnet may be represented by charged surfaces, as in the surface charge model of Yonnet [113]. The magnetic charge density  $\sigma$  on a surface with unit normal  $\hat{n}$  is given by

$$\sigma = J \cdot \hat{n} \quad (\text{A.17})$$

By way of illustration, Fig.76 shows a cuboidal magnet represented by two charged surfaces. Analytical expressions for the vector field at a point, due to a charged rectangular surface have been derived by Akoun and Yonnet [114].

### A.3.3 Consequences of particular symmetries in Halbach cylinders

Both the ideal and segmented designs have a *bilateral symmetry*:



76. A cuboid of magnetic material with polarisation  $J$  may be represented as two planes with equal and opposite surface charge density  $\sigma$ .

i.e.  $J$  is symmetric about  $\psi = 0$ :

$$J(\psi = \varepsilon) = J(\psi = -\varepsilon) \quad (\text{A.18})$$

In the ideal case and the case of cylinders with an even number of segments  $N$ , there is also a vertical asymmetry:

i.e.  $J$  is anti-symmetric about  $\psi = \pi/2$ ,

$$J(\psi = \pi/2 + \varepsilon) = -J(\psi = \pi/2 - \varepsilon) \quad (\text{A.19})$$

for any angle  $\varepsilon$ . Note that the angle  $\psi$  is measured from the  $y$ -axis as in Fig.72, and is related to the usual polar angle  $\phi$ , by  $\psi = \pi/2 - \phi$ .

Now consider the case of two infinitely long ideal cylinders (with polarisation direction varying continuously). Each has zero external stray field, and a perfectly uniform bore field. Therefore the field due to the inner cylinder in the volume occupied by the outer cylinder is zero. Hence according to Eq.A.6, the outer cylinder experiences no torque. By reciprocity, there can be no torque on the inner cylinder, which experiences a uniform field due to the outer cylinder. This implies that an ideal cylinder experiences zero torque in a uniform field. As a consequence of the symmetries in Eqs.A.18 and A.19, a finite length cylinder composed of an even number  $N$  of segments also experiences zero torque in a uniform field, as the torque on each segment is exactly balanced by an equal and opposite torque on another segment.

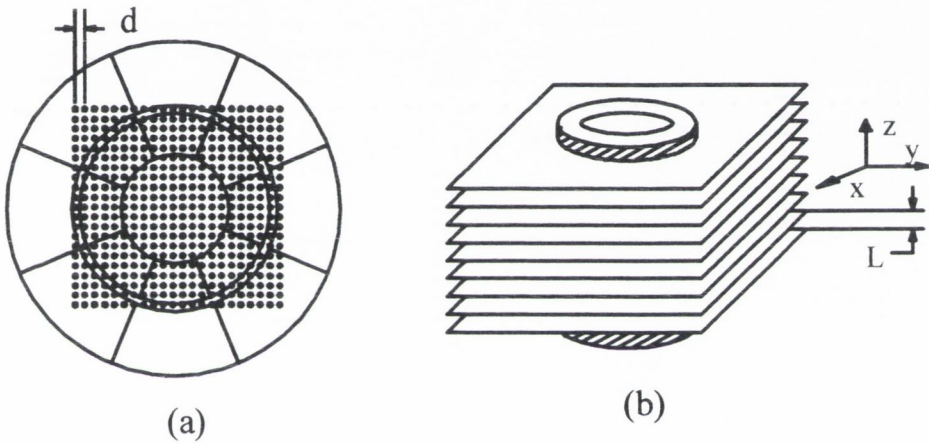
The torque observed experimentally must therefore arise from non-uniformities in the field, which are attributable to the segmented structure and finite length of both inner and outer cylinders.

## A.4 Numerical Simulation

There are two main steps in calculating the variation of the torque as the cylinders rotate. Firstly, the field produced in the bore of the outer cylinder is calculated numerically, using the surface charge model, as described in Section A.4.1. Secondly the torque experienced by the inner cylinder in this field is calculated, as in Section A.4.2. In Section A.4.3 we present the results of these calculations. Section A.4.4 presents a numerical analysis of the non-uniformities in the profile of the field in the cylinder bore, and relates these to the torque.

### A.4.1 Field Calculation

For the following calculation on segmented cylindrical magnets, each segment is treated as a combination of prisms in order to approximate curved surfaces. The total field at any point is simply the sum of the field contributions from each face, calculated using the surface charge model (Section A.3.2). On a cross-section of the cylinder, we specify a grid of points, each with position vector  $r = (x, y, z)$  as shown in Fig.77(a). At each of these points within the bore of the outer magnet we calculate the components of the field  $H_x$ ,  $H_y$  and  $H_z$ . The field varies along the length of the cylinder as well as across the width of the bore, and so is calculated across similar grids on a number of different, equally spaced planes as shown in Fig.77(b). Each point at which the field is calculated is surrounded by an element with volume  $\Delta V = Ld^2$ , where  $d$  is the separation between neighbouring points on the grid, and  $L$  is the separation between successive planes. This volume element must be sufficiently small to ensure the accuracy of the calculation.



77.(a) The grid of points, in one plane, at which the field of the outer cylinder is calculated. The inner cylinder is placed in the bore, and those grid points lying within the cross-section of the inner cylinder are used for the torque calculation; (b) Planes along the length of the cylinder.

### A.4.2 Torque Calculation

The total torque on the inner cylinder is calculated by summing over individual volume elements  $\Delta V$ , as in Eq.A.6. Similarly for the total energy  $E$ :

$$\Gamma = \sum_{\mathbf{i}} \Gamma^{(\mathbf{i})} = \sum_{\mathbf{i}} (J^{(\mathbf{i})} \times H^{(\mathbf{i})} \Delta V + r^{(\mathbf{i})} \times F^{(\mathbf{i})}) \quad (\text{A.20})$$

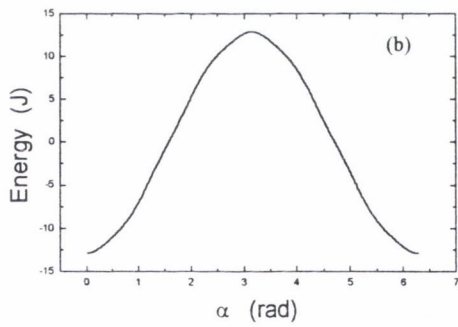
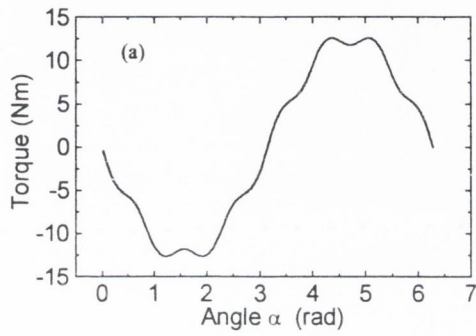
$$E = \sum_{\mathbf{i}} E^{(\mathbf{i})} = - \sum_{\mathbf{i}} J^{(\mathbf{i})} \cdot H^{(\mathbf{i})} \Delta V \quad (\text{A.21})$$

Here  $H^{(\mathbf{i})}$  is the field due to the outer cylinder at the position  $r^{(\mathbf{i})}$  of the  $i$ -th volume element of the inner cylinder, and  $J^{(\mathbf{i})}$  is the polarisation of that element. The force  $F^{(\mathbf{i})}$  at each point is proportional to the field gradient at that point, from Eq.A.5.

### A.4.3 Numerical Results

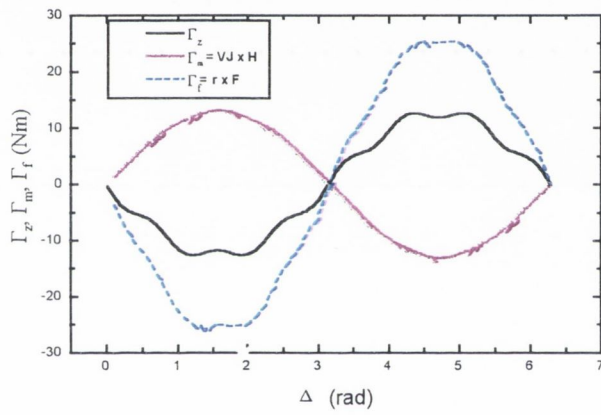
In this section, the results of the calculation of  $\Gamma$  and  $E$  are presented for cylinders of the same dimensions as those used to obtain the experimental data, given in the previous table. In accordance with expectations, the only non-zero component of torque is  $\Gamma_z$ , about the axis of the cylinder.

Fig.78(a) and (b) show  $\Gamma_z$  and  $E$  respectively as functions of  $\alpha$  (the angle through which the inner cylinder is rotated from the fully aligned position, as in Fig.73). The energy reaches a minimum at the fully aligned ( $\alpha = 0$ ) position. The energy data are closely fitted by a cosine function,  $E = -A \cos \alpha$ , where  $A$  is a positive constant. There are two contributions to  $\Gamma_z$  in Eq.A.20 (see Eqs.A.3 and A.4), each of which is shown in Fig.79. The  $\Gamma_{mz}$  and  $\Gamma_{fz}$  terms are found to be well approximated by  $A \sin \alpha$  and  $-2A \sin \alpha$  respectively. A good approximation to the total torque is therefore given by  $\Gamma_z = -A \sin \alpha$ .



78.(a) Torque on the inner cylinder as a function of angular position  $\alpha$  within the bore of the static outer cylinder; (b) Energy of the inner cylinder as a function of  $\alpha$ .

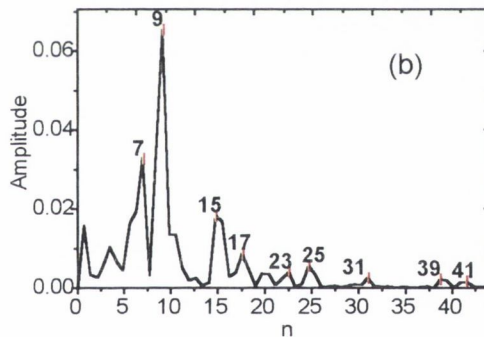
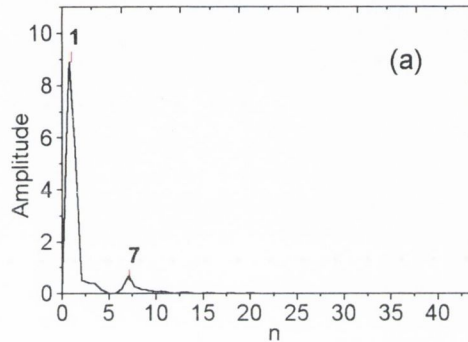




79. The resultant torque  $\Gamma_z$  is a combination of two contributions.

Numerical values of the contributions to the torque from different cross-sections along the axis of the cylinder show that the main contributions come from the end regions. The total value of the torque is not significantly changed by increasing the lengths of the cylinders, while the contribution from the central region becomes negligible. This indicates that the torque is primarily an end effect associated with the field inhomogeneities at the cylinder ends.

In addition to the fundamental sinusoidal variation,  $\Gamma$  is modulated by structure associated with segmentation. In similar contexts this structure is often referred to as “cogging torque”. Fig.80(a) shows the amplitude of the Fourier components of the torque data in Fig.78(a). The order of the dominant term in the torque variation,  $n = 1$ , corresponds to the leading sine term. The 7th order term is also pronounced. Higher harmonics are present, but with much smaller amplitudes. To see these more clearly, we fit a curve of the form  $B \sin \alpha + C \sin(7\alpha)$  to the data in Fig.78(a), where  $B$  and  $C$  are constants. The fitted curve is then subtracted from the original data. In so doing we largely remove the  $n = 1$  and  $n = 7$  terms. A Fourier transform of the remaining data is shown in Fig.80(b). Higher order terms can now be seen to occur in pairs at  $n = (N - 1), (N + 1), (2N - 1), (2N + 1), (3N - 1), (3N + 1)$ , etc., where  $N = 8$  is the number of segments (i.e. peaks at  $n = 7, 9, 15, 17, 23, 25$ , etc.). These terms coincide with the  $n = (kN \pm 1)$  terms which emerged experimentally in Fig.75. These results will be accounted for by the theory of Section A.5.



80.(a) Amplitude of Fourier components of the simulated  $\Gamma_z$  data, with dominant terms of order  $n = 1$  and  $7$  as labelled; (b) Fourier transform of the same data after a function of the form  $B \sin \alpha + C \sin(7\alpha)$  is fit to the data and subtracted off. Peaks of order  $n = (kN \pm 1)$  are now apparent, where  $N = 8$  is the number of segments and  $k$  is an integer.

#### A.4.4 Analysis of the Field Profile

Numerical calculation confirms that for a segmented cylinder with even  $N$  placed in a completely uniform field, the torque vanishes at every value of  $\alpha$ . Therefore in the case of two segmented cylinders, the existence of finite torque, and the dependence of  $E$  and  $\Gamma$  on  $\alpha$ , arise from inhomogeneities in the field.

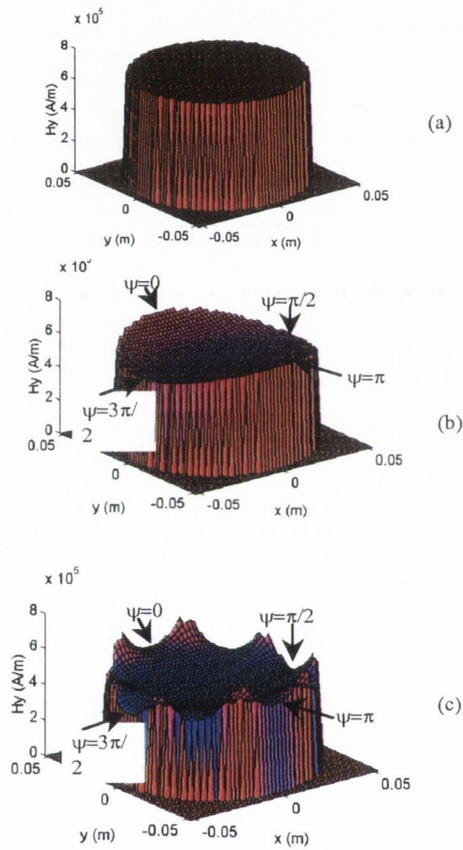
We have investigated these inhomogeneities by using the surface charge model to calculate the field in the bore of an outer cylinder with dimensions as given in the earlier table. We demonstrate separate contributions to field non-uniformities by varying segment number  $N$  and length  $L$ .

##### Approximation of Ideal Infinite Length Cylinder

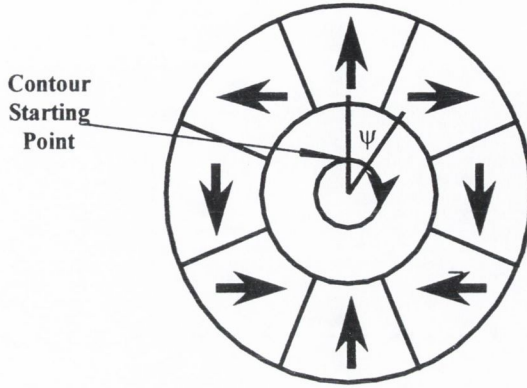
Fig.81(a) shows the profile of  $H_y$  in the bore midway along the length of the cylinder ( $z = 0$ ) when the cylinder is very long (to approximate infinite length) and has a large number of segments,  $N = 128$  (to approximate uniformly varying magnetisation). To the accuracy of our numerical procedure,  $H_y$  remains constant at all points in this central plane, as expected for an ideal cylinder of infinite length.

##### Field Variation due to Finite Length

Fig.81(b) shows the profile at  $z = 0$  in a cylinder with  $N = 128$  to approximate uniformly varying magnetisation, but with  $L = 100$  mm. The magnitude of the field at  $\psi = 0$  and  $\psi = \pi$  is greater than that at  $\psi = \pi/2$  and  $\psi = 3\pi/2$ . As the cylinder is made longer, the extent of this effect at the central  $z = 0$  position decreases, although it persists at both ends. This is therefore an end effect, associated with the finite length of the cylinder.



81. Profiles of the  $y$  component of field at  $z = 0$  in the bore of (a) an ideal, infinite length cylinder; (b) an ideal, finite length cylinder; (c) an 8-segment, finite length cylinder.



82. Field values in the next figure are taken clockwise from the starting point around a circular contour inside the bore.

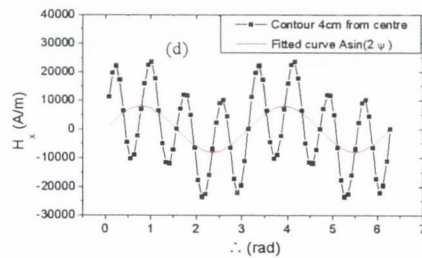
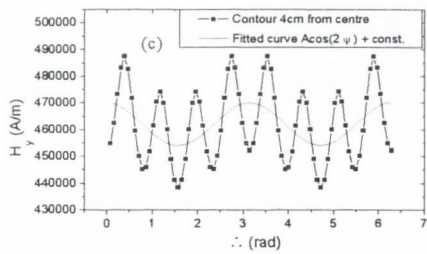
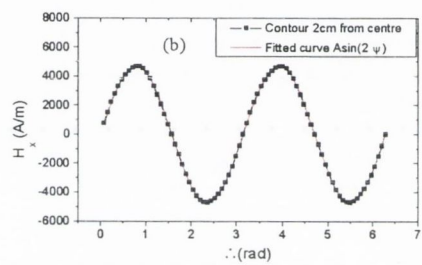
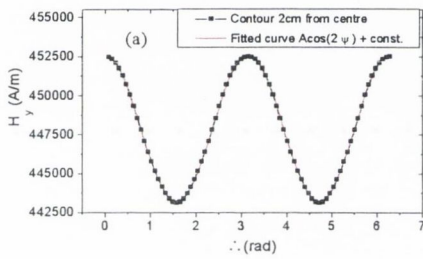
To determine a specific form for the end effect of Fig.81(b), consider the calculated magnitudes of  $H_y$  and  $H_x$  as a function of angular position  $\psi$  at a fixed radius within the bore such as that shown in Fig.82.  $H_y$  as a function of  $\psi$  is shown in Fig.83(a). This function is well fit by :

$$H_y = H_0 + \Delta H \cos (2\psi) \quad (\text{A.22})$$

Fig.83(b) plots  $H_x$  against  $\psi$ , which is fitted by :

$$H_x = \Delta H \sin (2\psi) \quad (\text{A.23})$$

Eqs.A.22 and A.23 are accounted for analytically in appendix B.



83.(a)  $H_y$  around contour of 20 mm radius; (b)  $H_x$  around contour of 20 mm radius; (c)  $H_y$  around contour of 40 mm radius; (d)  $H_x$  around contour of 40 mm radius; all at  $z = 0$  in a bore of 52.5 mm radius.

### Field Variation due to Segmentation

Fig.81(c) shows the profile for an 8-segment, finite length cylinder. Again the end effect is apparent, but in addition, peaking in the field occurs near the boundaries between adjacent segments throughout the bore.

Figs.83(c) and (d) show  $H_y$  and  $H_x$  as functions of  $\psi$ . The peaking effects of the eight segments appear superimposed on the end effect of Figs.83(a) and (b). As the number of segments is increased towards the case of an ideal, but finite length cylinder, the magnitude of the segmentation peaking decreases.

## A.5 Theoretical Model

In this section we demonstrate theoretically that the variation of the torque with relative orientation of the cylinders arises from field inhomogeneities due to their finite length and segmented structure. We apply symmetry arguments in the case of an ideal cylinder in Section A.5.1, and extend them to prove the 'Segmented Magnet Torque Theorem' in Section A.5.2. In Section A.5.3 we show analytically that the primary variation is due to finite length, while in Section A.5.4 we show that, in the limit of very long magnets, the torque does not increase with length. As an extension of this we identify the way in which the torque scales with the cylinder dimensions.

### A.5.1 Symmetry arguments in the ideal, finite length case

Firstly we consider a pair of nested, ideal, finite length Halbach cylinders, that is, cylinders in which the magnetic polarisation varies *continuously* as shown in Fig.72(a). The



polarisation  $J$  depends only on the angle  $\psi$  (measured clockwise from the  $y$  axis), while its magnitude  $J$  is independent of position:

$$J(\psi) = J (\sin 2\psi \hat{x} + \cos 2\psi \hat{y}) \quad (\text{A.24})$$

If the relative orientation of the cylinders  $\alpha$  is measured from the minimum energy configuration, where the polarisations in the two cylinders are fully aligned (Fig.73), then we shall show that the energy satisfies

$$E(\alpha) = E(0) \cos \alpha \quad (\text{A.25})$$

where we expect  $E(0) < 0$ . The corresponding torque is

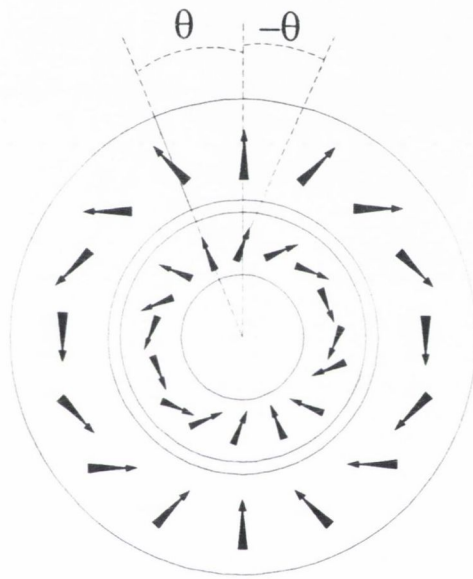
$$\Gamma(\alpha) = -\frac{dE}{d\alpha} = E(0) \sin \alpha \quad (\text{A.26})$$

The proof follows:

At a point in an ideal Halbach cylinder with angular position  $\psi$ , the polarisation  $J$ , Eq.A.24, makes angle  $\psi$  with the radius vector as shown in Fig.72(a). So rotating the inner cylinder through an angle  $\theta$  relative to the outer one is equivalent to keeping both cylinders fixed and rotating the polarisation at each point in the inner cylinder through angle  $-\theta$ , as shown in Fig.84.

The energy of an element of the inner cylinder of volume  $dV$  at the point  $r$  with coordinates  $(\rho, y, z)$  is

$$dE(r) = -J(r) \cdot H(r) dV = -JH(r) \cos \beta(r) dV \quad (\text{A.27})$$



84. Rotating the inner, ideal Halbach cylinder by  $\theta$  is equivalent to rotating the magnetisation at each point by  $-\theta$ .

where  $J(r)$  is the polarisation of the inner cylinder, and  $\beta(r)$  is the angle between this polarisation and the field  $H(r)$  due to the outer cylinder at that point. Let  $E(\theta_o)$  be the result of integrating Eq.A.27 over the volume of the inner cylinder, for some relative orientation of the cylinders  $\alpha = \theta_o$ .

Notice that integration of Eq.A.27 over the angular variable  $\psi$  gives zero if the field is entirely uniform. This follows because, in the case where  $H$  is independent of  $r$  and parallel to the  $y$  axis, the angle  $\beta(r) = 2\psi + \theta_o$ . Integration over  $\psi$  then gives zero energy and zero torque, in agreement with the symmetry arguments presented in Section A.3.3.

For an arbitrary initial relative orientation  $\theta_o$ , the energy after a further rotation through  $\theta$  is found by rotating the polarisation at each point through  $-\theta$ . The energy of the volume element at point  $r$  becomes

$$dE(r) = -J H(r) \cos(\beta(r) + \theta) dV = \text{Re}\{-J H(r) e^{i(\beta(r)+\theta)}\} dV \quad (\text{A.28})$$

where, for convenience, we have introduced complex notation. The magnitude of the polarisation, and the field  $H$  and angle  $\beta$  at the point  $r$  are unchanged. Integrating this expression over the volume  $V$  of the inner cylinder will give the form of the energy as

$$E(\theta + \theta_o) = \text{Re}\{f(\theta_o) e^{i\theta}\} \quad (\text{A.29})$$

where

$$f(\theta_o) = -J \int_V dV H(r) e^{i\beta(r)} = |f(\theta_o)| e^{i\beta_1(\theta_o)} \quad (\text{A.30})$$

Eq.A.29 then gives

$$E(\theta + \theta_o) = |f(\theta_o)| \cos(\theta + \beta_1(\theta_o)) \quad (\text{A.31})$$

If the initial orientation is chosen to be the minimum energy orientation, then  $\theta_o = 0$ , and the angle  $\theta$  becomes  $\alpha$ , the angular displacement from the minimum energy position from Fig.73. The bilateral symmetry of the polarisation, Eq.A.18, implies that

$$E(\alpha) = E(-\alpha) \quad (\text{A.32})$$

and this is only satisfied when  $\beta_1(0) = 0$ , giving the results Eqs.A.25 and A.26 advertised above for the energy and torque. This result is confirmed analytically in Section A.5.3.

### A.5.2 The Segmented Magnet Torque Theorem

In the case of segmented cylinders the discussion above may be generalised to prove the following theorem:

*The torque between a pair of segmented cylinders of finite length and relative orientation  $\alpha$  is obtained by differentiating the energy with respect to  $\alpha$ , where the energy may be written*

$$E(\alpha) = a_0 \cos \alpha + \sum_{k=1} (a_k \cos(kN - 1)\alpha + b_k \cos(kN + 1)\alpha) \quad (\text{A.33})$$

*and the summation is over all positive integers  $k$ .*

In the segmented case, the direction of the polarisation  $J^{(s)}$  is constant within a segment, so that rotation of the inner cylinder through angle  $\theta$  is equivalent to rotation of  $J^{(s)}$  through angle  $-\theta$  only when  $\theta$  is an integer multiple of  $2\pi/N$ . It is this restricted symmetry property which dictates the form of Eq.A.33, as follows.

Again it is convenient to use complex notation and write the energy of an element at point  $r$ , for some arbitrary orientation angle  $\theta_o$  in the range 0 to  $2\pi/N$ , as

$$dE^{(s)}(r) = -J^{(s)} H^{(s)}(r) \cos \beta^{(s)}(r) dV = -\operatorname{Re} \left( J^{(s)} H^{(s)}(r) e^{i\beta^{(s)}(r)} \right) dV \quad (\text{A.34})$$

where, as in Eq.A.27,  $\beta^{(s)}(r)$  is the angle between  $J^{(s)}$  and  $H^{(s)}$  at that point, and the superscript  $(s)$  identifies the segmented case. Now after a rotation through  $2\pi/N$  the energy of the element becomes

$$dE^{(s)}(r) = -\operatorname{Re} \{ J^{(s)} H^{(s)}(r) e^{i(\beta^{(s)}(r) + 2\pi/N)} \} dV. \quad (\text{A.35})$$

Integration over the volume of the inner cylinder gives the energy corresponding to the relative orientation  $\alpha = \theta_o + 2\pi/N$  as

$$E^{(s)}(\alpha) = \operatorname{Re} \{ f^{(s)}(\theta_o) e^{i2\pi/N} \} = \operatorname{Re} \{ f^{(s)}(\theta_o) e^{i(\alpha - \theta_o)} \} \quad (\text{A.36})$$

where, corresponding to Eq.A.30,

$$f^{(s)}(\theta_o) = -J^{(s)} \int_V dV H^{(s)}(r) e^{i\beta^{(s)}(r)}$$

We define

$$F(\alpha) = f^{(s)}(\theta_o) e^{-i\theta_o}$$

and Eq.A.36 may be written in terms of the angle  $\alpha$ :

$$E(\alpha) = \operatorname{Re} \{ F(\alpha) e^{i\alpha} \}$$

Since  $F(\alpha)$  depends only on  $\theta_o$ , we may write

$$F(\alpha) = F(\theta_o + 2\pi/N) = F(\theta_o) \quad (\text{A.37})$$

Thus  $F(\alpha)$  is periodic in  $2\pi/N$ , and may be expanded in a Fourier series:

$$F(\alpha) = \sum_{k=-\infty}^{+\infty} c_k \exp(ikN\alpha)$$

Substitution of this expansion into Eq.A.36 gives, for arbitrary relative orientation  $\alpha$ , an expression of the form

$$E^{(s)}(\alpha) = \text{Re} \left\{ c_0 \exp(i\alpha) + \sum_{k=1} c_k \exp(i(kN+1)\alpha) + c_{-k} \exp(i(-kN+1)\alpha) \right\} \quad (\text{A.38})$$

The bilateral symmetry requirement Eq.A.32 eliminates all sine terms in Eq.A.38. Thus this expression for the energy reduces to Eq.A.33, and since the orientation  $\alpha = 0$  corresponds to a minimum energy we should expect  $a_0 < 0$ . Differentiation of Eqn.(28) gives the following expression for the torque:

$$\Gamma(\alpha) = a_0 \sin \alpha + \sum_{k=1} ((kN-1) a_k \cos(kN-1)\alpha + (kN+1) b_k \cos(kN+1)\alpha) \quad (\text{A.39})$$

The allowed terms which emerge in this equation agree with those seen both experimentally and numerically, shown in Figs.75 and 80 respectively.

### A.5.3 Analytical Results for the Finite Length Effect

In the previous section, we showed by symmetry arguments that the leading term in the torque variation is sinusoidal, as shown in Eq.A.39. In this section we show analytically

that the leading sinusoidal term is determined by field non-uniformities due to the finite length of the cylinders.

Consider nested cylinders of finite length, but uniformly varying magnetisation. The outer cylinder is kept fixed and the inner rotated through  $\alpha$  from the fully aligned position as in Fig.73. From Eq.A.6, the torque  $d\Gamma_z$  on any volume element of the inner cylinder,  $dV$ , centred on point  $r(x, y, z) \equiv r(\rho, \psi, z)$ , is given by

$$\begin{aligned} d\Gamma_z(\rho, \psi, z) &= (J_x H_y - J_y H_x) dV + (x F_y - y F_x) \\ &= \left( (J_x H_y - J_y H_x) + x \left( J_x \frac{dH_x}{dy} + J_y \frac{dH_y}{dx} \right) \right) dV \end{aligned} \quad (\text{A.40})$$

where the force on the element has components  $F_i = \sum_l J_l (\nabla_i H_l) dV$ , and  $J$  lies in the  $xy$ -plane.

When the two cylinders are in the fully aligned position, the polarisation  $J$  at an angular position  $\psi$  in each cylinder is at  $2\psi$  to the  $y$ -axis. After rotating the inner cylinder through  $\alpha$ , the polarisation  $J$  at a point in the inner cylinder with orientation  $\psi$  is given by

$$J = J (\sin(2\psi + \alpha) \hat{x} + \cos(2\psi + \alpha) \hat{y}) \quad (\text{A.41})$$

In appendix B, we have derived analytical forms of the  $x$  and  $y$  components of the field in the bore, Eq.B.17:

$$H_x = \Delta H(\rho, z) \sin(2\psi)$$

$$H_y = H_0(\rho, z) + \Delta H(\rho, z) \cos(2\psi) \quad (\text{A.42})$$

where the expressions for  $H_0(\rho, z)$  and  $\Delta H(\rho, z)$  are given in Eq.B.18. In the case of infinite length,  $\Delta H \rightarrow 0$  and  $H_0 \rightarrow (J/\mu_0) \ln(R_o/R_i)$  as in Eq.A.1. The field gradient has

components

$$\begin{aligned}
 \frac{\partial H_x}{\partial x} &= \frac{\partial(\Delta H)}{\partial \rho} \sin \psi \sin(2\psi) + \frac{2\Delta H}{\rho} \cos \psi \cos(2\psi) & (A.43) \\
 \frac{\partial H_x}{\partial y} &= \frac{\partial(\Delta H)}{\partial \rho} \cos \psi \sin(2\psi) - \frac{2\Delta H}{\rho} \sin \psi \cos(2\psi) \\
 \frac{\partial H_y}{\partial x} &= \frac{\partial(H_0 + \Delta H \cos(2\psi))}{\partial \rho} \sin \psi - \frac{2\Delta H}{\rho} \cos \psi \sin(2\psi) \\
 \frac{\partial H_y}{\partial y} &= \frac{\partial(H_0 + \Delta H \cos(2\psi))}{\partial \rho} \cos \psi + \frac{2\Delta H}{\rho} \sin \psi \sin(2\psi)
 \end{aligned}$$

since, from Fig.85,

$$x = \rho \sin \psi \quad (A.44a)$$

$$y = \rho \cos \psi \quad (A.44b)$$

Substituting into Eq.A.40, and cancelling terms, we find

$$d\Gamma_z = (J H_0 \sin(2\psi + \alpha) + J \Delta H \sin \alpha - 2J \Delta H \sin \alpha) dV \quad (A.45)$$

Eq.A.45. contains two separate contributions:

$$(J_x H_y - J_y H_x) = (J H_0 \sin(2\psi + \alpha) + J \Delta H \sin \alpha) \quad (A.46)$$

and

$$(x F_y - y F_x) = -2J \Delta H \sin \alpha \quad (A.47)$$

The total torque  $\Gamma_{tot}$  is found by integrating over the volume of the inner cylinder:

$$\Gamma_{tot}(\alpha) = \iiint (J H_0 \sin(2\psi + \alpha) - J \Delta H \sin \alpha) \rho d\rho d\psi dz \quad (A.48)$$

After performing the angular integration

$$\Gamma_{tot}(\alpha) = -2\pi J \sin \alpha \iint \Delta H(\rho, z) \rho d\rho dz \quad (A.49)$$



i.e.

$$\Gamma_{tot}(\alpha) \propto -\sin \alpha \quad (\text{A.50})$$

Note that the result in Eq.A.49 is the combination of the two terms in Eqs.A.46 and A.47, which contribute in a ratio  $-2 : 1$ . This is in agreement with the ratio between these contributions found numerically in Fig.79.

This analysis demonstrates that, in the case of an ideal cylinder of finite length, the torque varies as  $-\sin(\alpha)$  in accordance with the symmetry arguments of Section A.5.1, and in agreement with experimental (Section A.2) and numerical (Section A.4.3) results.

#### A.5.4 Torque in the case of long ideal Halbach cylinders

In the case of ideal Halbach cylinders of finite length, the torque tends to a constant as the length is increased. It is therefore an end effect. This is demonstrated theoretically below.

Consider first a single semi-infinite Halbach cylinder occupying  $-\infty < z < 0$ . The field at a distance  $z$  from the end of the cylinder is given by  $H(z)$  (suppressing the other spatial variables  $\rho, \phi$ ). For large  $z$ , this field is the sum of contributions from distant dipoles, so it must diminish with  $z$  at least as fast as

$$\int_z^\infty (z')^{-3} dz' = O(z^{-2}) \quad (\text{A.51})$$

A Halbach cylinder of finite length  $L$  may be treated as a finite section of an infinite cylinder, which consists of the finite section with a semi-infinite section added at each end. The field  $H(z)$  in the bore of the finite section is the difference between the uniform field  $H_0$  due to the infinite cylinder and the contributions  $\Delta H_1(z)$  and  $\Delta H_2(z)$  from the two

semi-infinite segments:

$$H(z) = H_0 - \Delta H_1(z) - \Delta H_2(z)$$

The torque on a Halbach cylinder in a uniform field is zero (Sections A.3.3 and A.5.1). So, in considering the torque on a second Halbach cylinder of length  $L$ , nested within the first one (also of length  $L$ ), there is no contribution from  $H_0$ , and we can use  $-(\Delta H_1(z) + \Delta H_2(z))$  instead of  $H$ . Expressing this torque in terms of an integral (the element  $d\Gamma_z$  of Eq.A.6 integrated over the volume of the inner cylinder) we see that the contribution of each of the two terms  $\Delta H_1(z)$  and  $\Delta H_2(z)$  is independent of  $L$  as  $L \rightarrow \infty$ , because of the rapid convergence of the fields indicated by Eq.A.51. This equation suggests that the asymptotic form of the torque for long cylinders is of the form

$$\Gamma \sim \text{constant} + O(L^{-1}) \quad (\text{A.52})$$

The order indicated is an upper bound. The symmetries considered here imply a stronger (octupole) decrease of the field than  $z^{-2}$ , and the actual asymptotic form of  $\Gamma$  should be of order  $L^{-3}$ .

### Scaling laws

From the definition of energy in Eq.A.2, we see that as the dimensions are scaled up, the energy must scale as (length)<sup>3</sup>. We have just shown that, in the ideal case, the torque is independent of the length of the cylinder, in the limit of large length. The scaling law may therefore be written

$$\Gamma \propto R_i^3 \quad (\text{A.53})$$

independent of  $L$ , for long, ideal Halbach cylinders. For segmented cylinders there is a second term of order  $R_i^2 L$ . This prediction is born out by numerical calculation .

## A.6 Conclusion

Halbach cylinders experience zero torque in uniform applied field. Thus the origin of the real torque observed in nested systems of finite length, segmented Halbach cylinders merits investigation. In Section A.5.3, we see that although each volume element experiences a large torque due to the applied field  $H_0$ , these contributions cancel over the whole cylinder, due to symmetry. Therefore the resultant torque is determined by the much smaller fluctuations in this field due to finite length and segmentation. The total torque for cylinders with this particular symmetry is much less than we should expect from the magnitude of the torque on any one segment.

The principal variation of the torque as the inner cylinder is rotated through an angle  $\alpha$ , while holding the outer cylinder fixed, is sinusoidal. We have derived an analytical theory of the inhomogeneities in the fields produced in the cylinder bores. This, together with symmetry arguments, leads to the fact that the dominant sinusoidal variation in torque is an end effect due to the finite lengths of the cylinders.

The remaining variation in the torque is accounted for in the ‘Segmented Magnet Torque Theorem’ where we use symmetry to isolate the higher order,  $n = (kN \pm 1)$ , terms in the Fourier transform of the torque data (where  $N$  is the number of segments in the cylinder, and  $k$  is an integer). This symmetry analysis says nothing about the size of the coefficients in Eq.A.39. In particular, nothing is determined about specific dependencies of

the coefficients on  $N$  or on the dimensions of the cylinders. This may provide an interesting topic for future study. However, the numerical calculations show that all coefficients for  $k \geq 1$  are small compared with the magnitude of  $a_0$ , and decrease strongly with  $k$ , although this may not necessarily be the case for alternative designs.

In the case of ideal cylinders, the torque is independent of the length  $L$ , in the limit of large  $L$ , and this leads to the scaling law  $\Gamma \propto R^3$ , where  $R$  is a radial dimension of the nested cylinders. This implies that, for long ideal cylinders, the torque is produced entirely in regions within a distance  $\sim R$  from either end.

Good agreement was found between experiment, numerical calculation and analytic theory, with respect to angular variation of torque as the cylinders are rotated. The calculated value for the magnitude of the torque was found to be an upper bound on experimental values. Experimental results show maximum values ranging from 6 – 13 Nm for different magnet assemblies of the same dimensions with an average of approximately 8 Nm, while the numerical maximum is 12.6 Nm. A number of factors may account for this difference, as follows.

Our field calculation is based on the assumption of zero transverse susceptibility  $\chi_{\perp}$ , while in reality  $\chi_{\perp} \approx 0.1$ . As this will tend to align the magnetisation direction along the direction of the applied field, it may act to reduce the net torque experienced. Calculated fields are often as much as 10% greater than those measured in the bores of real cylinders. In part this reflects non-rectangularity of the hysteresis loop. As torque is proportional to  $J^2$ , this may account for up to 20% reduction in the torque observed compared to that calculated. In addition, in the two cylinder system detailed in Section A.2, steel ball-

bearings are attached to the cylinder ends to allow them to rotate. This soft magnetic material draws some flux from the bore, particularly at the ends where the torque is most significant. This reduction in applied field may further serve to reduce the experimentally observed torque. Thus the calculated value for torque acts as an upper bound for real systems.

# Appendix B

## Calculation of the field due to a finite length ideal Halbach cylinder

The field due to a Halbach cylinder may be calculated from a magnetic potential  $\varphi_m$  which satisfies the Poisson Eq.A.16. In the case of an ideal cylinder, the polarisation varies continuously according to Eq.A.24. If this equation is rewritten in terms of conventional cylindrical coordinates  $\rho$ ,  $\phi (= \pi/2 - \psi)$  and  $z$ , the polarisation is of the form

$$J(\phi) = J (\sin(2\phi) \hat{x} - \cos(2\phi) \hat{y}) \quad (\text{B.1})$$

In this case, the volume magnetic charge density is

$$\rho_m(r) = -\nabla \cdot J = -\frac{2J \sin \phi}{\rho} \quad (\text{B.2})$$

This is non-zero over the volume  $V$  of the cylinder:  $R_i < \rho < R_o$ ,  $0 < \phi < 2\pi$ , and, in the case of finite length,  $-L/2 < z < L/2$ .

The solution to the Poisson equation for the potential at a point  $r$  is

$$\varphi_m(r) = \frac{1}{4\pi\mu_0} \int_V dV' \frac{\rho_m(r')}{|r - r'|} \quad (\text{B.3})$$

where primed coordinates indicate source points, and the integration is over the volume of the cylinder. The denominator in the integrand may be expanded in terms of spherical harmonics: B.3

$$\frac{1}{|r - r'|} = 4\pi \sum_{l=0}^{\infty} \sum_{m=-l}^{+l} \frac{1}{(2l+1)\mu_0} \frac{r_{<}^l}{r_{>}^{l+1}} Y_{lm}^*(\theta', \phi') Y_{lm}(\theta, \phi) \quad (\text{B.4})$$

where  $r_<$  and  $r_>$  are respectively the lesser and greater of  $r$  and  $r'$ . This equation is expressed in spherical polar coordinates, related to the cylindrical coordinates by

$$\rho = r \sin \theta \quad (\text{B.5})$$

$$z = r \cos \theta = \rho \cot \theta$$

Substitution of Eq.B.4 into Eq. gives the potential

$$\varphi_m(r) = \sum_{l=0}^{\infty} \sum_{m=-l}^{+l} \left( a_{lm} r^l + \frac{b_{lm}}{r^{l+1}} \right) Y_{lm}(\theta, \phi) \quad (\text{B.6})$$

where

$$a_{lm} = \frac{1}{(2l+1)\mu_0} \int_V dV' \frac{\rho_m(r')}{r'^{l+1}} Y_{lm}^*(\theta', \phi') \quad (\text{B.7})$$

$$b_{lm} = \frac{1}{(2l+1)\mu_0} \int_V dV' \rho_m(r') r'^l Y_{lm}^*(\theta', \phi')$$

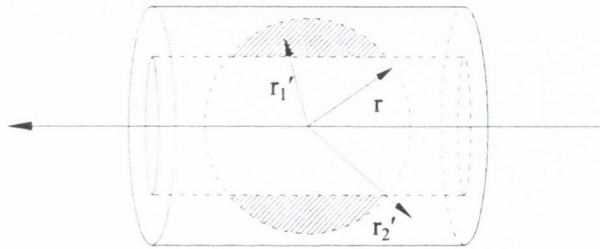
For source points such that  $r' > r$  the first term in Eqn.(A6) contributes to the potential, while the second term is the contribution from regions where  $r' < r$ .

In the case of an infinitely long ideal cylinder, the potential, giving rise to the field of Eq.A.1, is

$$\varphi_{m\infty} = -\frac{J}{\mu_0} r \sin \theta \sin \phi \ln \left( \frac{R_o}{R_i} \right) \quad (\text{B.8})$$

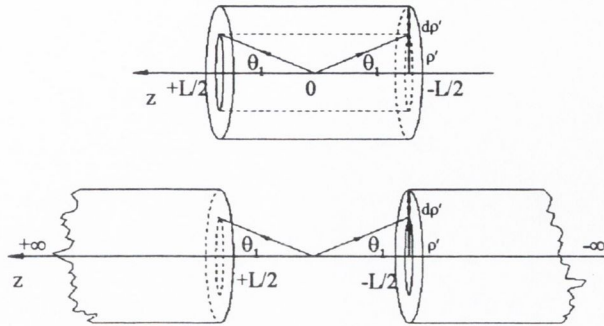
We wish to calculate the potential within the bore of an ideal Halbach cylinder of *finite* length  $L$ .

At an arbitrary point  $r$  in the bore there will, in general, be contributions to the potential from points in the magnetic material with  $r' > r$ , such as  $r'_2$  in the unshaded region of Fig.85, and also from points with  $r' < r$ , such as  $r'_1$  in the shaded region. To simplify



85. The field at a point  $r$  in the cylinder bore is due to source points  $r'$  in the cylinder, some of which satisfy  $r > r'$ , such as  $r'_1$  in the shaded regions, and some of which satisfy  $r < r'$ , such as  $r'_2$  in the unshaded regions.





86.(a) The field due to an ideal Halbach cylinder of finite length  $L$  may be calculated by integrating over the volume of the cylinder; (b) alternatively it may be found by calculating, by integration, the field due to two semi-infinite cylinders, separated by a distance equal to the length of the finite length cylinder, and subtracting this field from the field created by an infinite length cylinder.

the calculation and avoid the necessity of evaluating contributions from points with  $r' < r$ , we proceed as follows:

We calculate the potential due to two semi-infinite ideal cylinders, one extending from  $z = L/2$  to  $\infty$ , and the other from  $z = -L/2$  to  $-\infty$ , Fig.86. From this we find the potential due to these cylinders at points in the bore between  $z = -L/2$  and  $z = +L/2$ , and then subtract the result from the potential for a cylinder of infinite length, Eq.B.8. The field due to a cylinder extending from  $z = -L/2$  to  $z = L/2$  at a point within its bore is then found from the gradient of this potential. All points within the material of the two semi-infinite cylinders satisfy  $r' > r$ , where  $r$  refers to any point within the bore of the finite length cylinder,  $-L/2 < z < +L/2$ ,  $\rho < R_i$ .

Consider a cylindrical shell of thickness  $d\rho'$  at a fixed radius  $\rho'$  within the semi-infinite cylinder defined by  $R_i < \rho' < R_o$ ,  $L/2 < z' < \infty$ . The contribution of this shell

to the potential at a point  $r$  in the region  $\rho < R_i$ ,  $-L/2 < z < +L/2$  is, from Eqs.B.2, B.6 and B.7

$$d\varphi_{m+}(r, \theta, \phi) = \sum_{l=0}^{\infty} \sum_{m=-l}^{+l} da_{lm} r^l Y_{lm}(\theta, \phi) \quad (\text{B.9})$$

where

$$da_{lm} = \frac{-2J}{(2l+1)\mu_0} \int_{L/2}^{\infty} dz' \int_0^{2\pi} d\phi' \rho' d\rho' \frac{\sin \phi'}{\rho'} \frac{1}{r'^{l+1}} Y_{lm}^*(\theta', \phi'). \quad (\text{B.10})$$

Using Eq.B.5 to write  $z'$  and  $r'$  in terms of  $\theta'$  and  $\rho'$ , this becomes

$$da_{lm} = \frac{-2J}{(2l+1)\mu_0} \int_0^{\theta_1} d\theta' \int_0^{2\pi} d\phi' \sin \phi' \frac{d\rho'}{\rho'^l} \sin^{l-1} \theta' Y_{lm}^*(\theta', \phi')$$

where, from Fig.86, the upper limit of the integration over  $\theta$  satisfies

$$\cot \theta_1 = \frac{L}{2\rho'} \quad (\text{B.11})$$

Integrating over  $\phi'$  and substituting into Eq.B.9 we obtain

$$d\varphi_{m+}(r, \theta, \phi) = \frac{-J}{\mu_0} \sum_{l=1}^{\infty} \frac{(l-1)!}{(l+1)!} P_l^1(\cos \theta) \sin \phi r^l \left( \frac{d\rho'}{\rho'^l} \int_0^{\theta_1} d\theta' \sin^{l-1} \theta' P_l^1(\cos \theta') \right) \quad (\text{B.12})$$

where  $P_l^m(\cos \theta')$  is an associated Legendre function.

Similarly an expression is obtained for the potential  $d\varphi_{m-}(r, \theta, \phi)$  due to the cylindrical shell extending from  $z = -L/2$  to  $-\infty$ . The symmetry properties of the integrand indicate that each term of the summation in  $d\varphi_{m+}$  is equal to the corresponding term in  $d\varphi_{m-}$  apart from a factor  $(-1)^{l+1}$ . Thus terms with even  $l$  cancel. The total potential due to the two semi-infinite cylinders is obtained by integrating over  $\rho'$ :

$$\varphi_{m+} + \varphi_{m-} = \frac{-2J}{\mu_0} \sum_{l \text{ odd}}^{\infty} \frac{(l-1)!}{(l+1)!} P_l^1(\cos \theta) \sin \phi r^l \left( \int_{R_i}^{R_o} \frac{d\rho'}{\rho'^l} \int_0^{\theta_1} d\theta' \sin^{l-1} \theta' P_l^1(\cos \theta') \right). \quad (\text{B.13})$$

Notice that the upper limit of the integration over  $\theta'$  is a function of  $\rho'$ , Eq.B.11.

The integrand of the angular integration may be rewritten using the property of Legendre functions

$$\sin^l \theta' = \frac{2^l l!}{(2l)!} P_l^l(\cos \theta') \quad (\text{B.14})$$

Finally, the potential due to a cylinder of length  $L$  is

$$\begin{aligned} \varphi_{mL} &= \varphi_{m\infty} - (\varphi_{m+} + \varphi_{m-}) \\ &= \frac{-J}{\mu_0} r \sin \theta \sin \phi \ln \left( \frac{R_o}{R_i} \right) + \frac{2J}{\mu_0} \sum_{l \text{ odd}}^{\infty} \frac{(l-1)!}{(l+1)!} I_l P_l^1(\cos \theta) \sin \phi r^l \end{aligned} \quad (\text{B.15})$$

where

$$I_l = \int_{R_i}^{R_o} \frac{d\rho'}{\rho'^l} \int_0^{\theta_1} d\theta' \frac{2^l l!}{(2l)!} \frac{P_l^l(\cos \theta') P_l^1(\cos \theta')}{\sin \theta'} \quad (\text{B.16})$$

The magnetic field due to the finite length cylinder,  $H = -\nabla \varphi_{mL}$ , has components

$$H_x(r, \theta, \phi) = \Delta H(r, \theta) \sin(2\phi) \quad (\text{B.17})$$

$$H_y(r, \theta, \phi) = H_0 - \Delta H(r, \theta) \cos(2\phi)$$

$$H_z(r, \theta, \phi) = \Delta H_z(r, \theta) \sin \phi$$

where

$$\begin{aligned} \Delta H(r, \theta) &= \frac{-J}{\mu_0} \sum_{l \text{ odd}}^{\infty} \frac{(l-1)!}{(l+1)!} r^{l-1} I_l \left( ((l+1) \sin^2 \theta - 2) \frac{dP_l}{d(\cos \theta)} + l(l+1) \cos \theta P_l \right) \\ H_0(r, \theta) &= -\frac{J}{\mu_0} \ln \left( \frac{R_o}{R_i} \right) + \Delta H(r, \theta) - \frac{2J}{\mu_0} \sum_{l \text{ odd}}^{\infty} \frac{(l-1)!}{(l+1)!} r^{l-1} I_l \frac{dP_l}{d(\cos \theta)} \\ \Delta H_z(r, \theta) &= -\frac{2J}{\mu_0} \sum_{l \text{ odd}}^{\infty} \frac{(l-1)!}{(l+1)!} r^{l-1} I_l \left( (l+1) \sin \theta \cos \theta \frac{dP_l}{d(\cos \theta)} - l(l+1) (\sin \theta) P_l \right) \end{aligned} \quad (\text{B.18})$$